Development of the Flight Computer for the RadMap Telescope

Marius Anger

23.11.2020

Department of Physics
Technical University of Munich

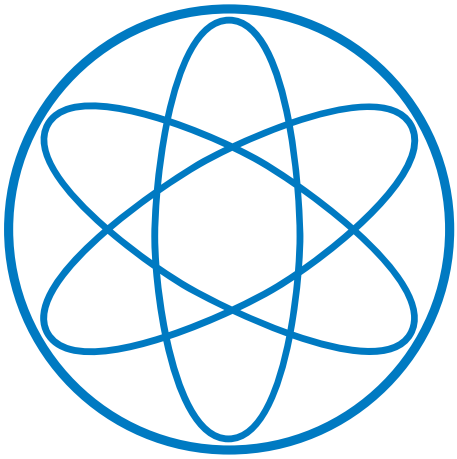

Master Thesis

Supervised by

Prof. Dr. Stephan Paul
Institute for Hadronic Structure and Fundamental Symmetries (E18)

Abstract

Galactic cosmic rays and solar particle events during deep-space missions to the Moon, Mars and other destinations are critical health risks to humans. A precise characterisation of the radiation environment within a spacecraft is needed to protect the astronauts from the diverse effects of radiation exposure. This work presents the development of the flight computer and the system architecture of the RadMap Telescope. The experiment aims to validate a radiation monitoring device aboard the International Space Station for missions beyond low Earth orbit. The instrument combines a scintillating fiber-based particle telescope and two flight-proven dosimeters as well as two crystal dosimeters in a compact form factor.

Acknowledgements

I would like to express my gratitude to *Martin Losekamm* for offering me this thesis and for guidance and support throughout this journey. Even though you had so much to do for many other tasks and projects, you had time for my doubts and questions. It is simply amazing, how you had time for me and keep all of it rolling at the same time.

I thank *Sebastian Würl*, *Jan Henrik Müller* and *Malte Schmitz* for helping me out with errors in my code and other computer science questions.

Since I was quite new to PCB designing, I also have to thank *Dominik Steffen* and *Igor Konorov* for answering a lot of questions and helping out with their laboratory equipment.

All of you were a great help!

Contents

Chapter 1

Introduction

Radiation doses to astronauts in deep space are much higher than annual dose limits for humans on Earth [1]. Therefore it is important to obtain precise information about dose rates and exposure risks. This information currently has poorly understood uncertainties making risks assessments for long term interplanetary missions difficult [2]. The current detector suite used aboard the International Space Station (ISS) to improve these uncertainties is comprised of several different instruments in terms of size, weight and technology. The RadMap Telescope aims to combine advantages of currently used spectrometer and dosimeter technologies into one compact and simple deployable device to reduce the complexity of radiation environment monitoring.

This thesis describes the development of the RadMap Telescope flight computer. The instrument will soon be deployed for half a year inside the International Space Station (ISS) to validate its capabilities for deep-space missions.

Figure 1.1: The RadMap Telescope in flight configuration.

The RadMap Telescope measures $13 \times 13 \times 15\,\mathrm{cm}^3$ and weighs about 3.5 kg. The main detector system uses scintillating fibers made of polystyrene to detect traversing particles within an active volume of $512\,\mathrm{cm}^3$. Photons produced via ionisation of fiber atoms along the track are detected via silicon photomultipliers (SiPMs). The produced signals are digitised by the read out electronics (ROE) and passed to the flight computer or central control unit (CCU), where artificial neural networks will

process the acquired information. The RadMap Telescope aims to provide near-real-time dose rates and radiation environment measurements for deep-space missions, which can be transmitted to Earth or used directly aboard the spacecraft.

In section 1.1 the radiation environment and current measurement technologies in space as well as the effects of radiation will be explained. A more detailed overview of the RadMap Telescope is given in chapter 2. Chapter 3 and following explain the development steps and tests of the RadMap Telescope flight computer.

1.1 Radiation in the Solar System

The radiation environment in space consists of two primary sources within the solar system: Solar protons and other particles of solar origin ejected rapidly in large events called Solar Particle Events (SPEs) [3] (section 1.1.2) as well as an extra-solar, isotropic background radiation of galactic origin known as Galactic Cosmic Rays (GCRs) [4] (section 1.1.3).

Affected by the other bodies within the solar system these sources can create secondary particles [5]. Particles can be trapped around an object by the magnetic field of the body, for instance in belts around Earth or the Jupiter moon Io [6, 7] (section 1.1.4). Secondary particles produced by interactions of high energetic particles with the surface or atmosphere of a planetary body can also contribute to the radiation environment of a spacecraft (section 1.1.4).

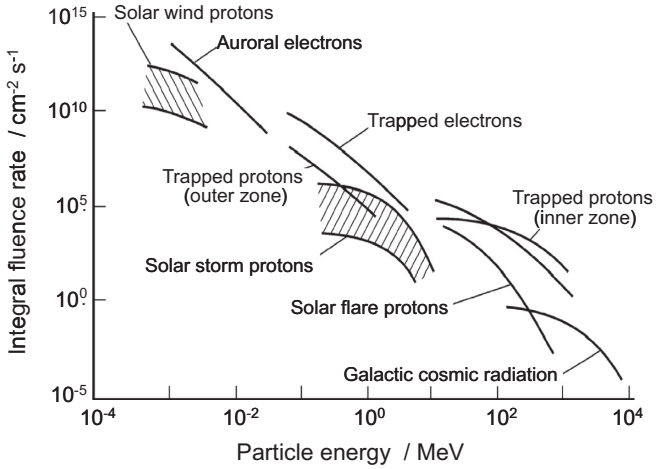

Figure 1.2: Most important sources of space radiation with their energy and particle flux [8].

An overview over the energy and particle flux density of these radiation sources is given in Figure 1.2. The relative size, energy and charge contribution of each radiation source to the overall radiation flux in a spacecraft is dependent on a large number of parameters including the altitude and inclination of the orbit, the orientation relative to the orbiting body and the Sun and the particular phase of the solar cycle.

1.1.1 The Sun

The Sun dominates nearly all processes within roughly 10 au[1] and more in radius, known as the heliosphere [9]. The heliosphere is the domain in which the Sun's magnetic field (the interplanetary magnetic field, IMF) is most dominant. The gravitational effects of the Sun dictate the topology in its surrounding space.

[1] 1 au = 149 597 870 700 m is the distance between Earth and the Sun.

In addition to emitting blackbody (electromagnetic) radiation, the Sun emits up to a mega ton of particles per second. This flux consists mostly of protons and electrons of 1.5 keV to 10 keV [10]. This so-called solar wind is responsible for most space weather. It is ejected from the Sun's corona, its outermost region. Here hydrogen and helium atoms can escape gravitational attraction and form a steadily streaming outflow. Because of its high temperature and constant illumination by the Sun, the solar wind is fully ionized plasma.

The radiation environment within the heliosphere is largely dictated by the Sun and its behaviour. Certain components of the radiation environment originate directly and nearly all other contributions to it are modulated or modified by solar activity.

The Sun's activity varies in a 22-year cycle observable through the number of sunspots present on the surface [11]. This solar cycle originates in the differential rotation[2] of the Sun of about 26 days at the equator [12]. It disturbs the magnetic field lines in its interior and every half solar cycle (11 years) a major rearrangement of the magnetic field lines weakens the IMF and its polarity flips. The cycle is often considered to be 11 years long on average ignoring magnetic field polarity. Sunspots are caused by the magnetic field lines converging underneath the surface. Thus, changes in the magnetic field can be related to the number of sunspots seen on the surface [13]. The cycle is at its minimum when the minimum number of sunspots can be observed and at maximum when the maximum number of spots is observed.

1.1.2 Solar Particle Events and Solar Energetic Particles

Solar energetic particles (SEPs) are part of the solar wind activity. They have two different sources [3]: Solar flares and coronal mass ejections (CMEs). Both are so-called Solar Particle Events (SPEs).

A solar flare is a sudden flash of increased brightness on the Sun, usually observed near its surface and in close proximity to a sunspot group as seen in Figure 1.3a. Solar flares originate in the interior of the Sun. A CME is a significant release of plasma and accompanying magnetic field from the solar corona (Figure 1.3b). They often follow solar flares. SEPs associated with CMEs are the most intense type.

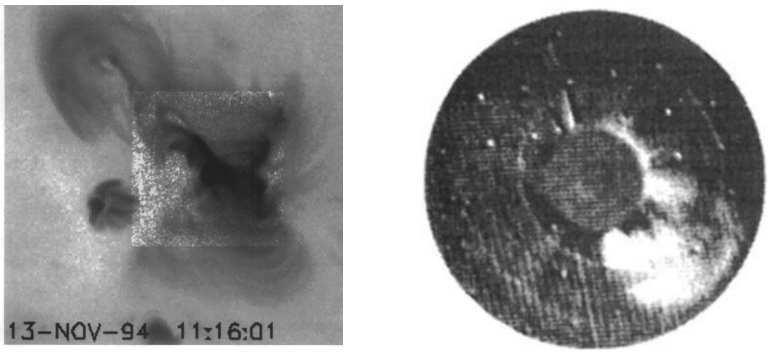

(a) (b)

Figure 1.3: (a) Composite image of low and high resolution image of a solar flare (black) on the Sun's surface, occurred on November 13, 1994 [14]. (b) CME observed by Solwind coronagraph. The Sun is blocked by a light shield in the middle of the image. Ejected mass (white) is seen in the lower right. It occurred on May 10, 1979 [15].

Both SPEs occur when the magnetic field realigns explosively at the surface of the Sun and drives vast amounts of energy into space [16]. Particle energies range from 1 MeV up to many GeV [17]. They consist of electrons, protons and heavier charged particles up to iron [18, 19]. The main difference between them is that CME particles disturb the magnetic field lines of the sun because of their higher energies while flare particles travel mostly along them [20, 9].

[2] Parts of a non solid rotating object rotate at different angular velocities at different latitude and depth of the body.

About 50 SPEs can be expected over the course of a single solar cycle [21]. Due to the vast difference in the spectrum of SPEs not all events impinging on a spacecraft do have lethal influences to the astronauts. A major SPE is defined as an event having a proton flux over 10 MeV per 10^{10} cm^2. One or two events of this magnitude can be expected per solar cycle [5]. Such an event is considered a major health risk to astronauts due to the high energy flux.

1.1.3 Galactic Cosmic Rays

GCRs are charged particles that originate from sources beyond our solar system. These ions are accelerated by interstellar objects nearly to the speed of light [4]. Among other phenomena supernova explosions can accelerate such particles by diffuse shock interactions with the ejected material [22, 23]. These particles interact many times with other particles along their way to the Solar System [24]. Therefore one can not trace them back to the origin and observes an isotropic background.

The GCR spectrum consists of 98 % protons and heavier ions (baryon component) and 2 % electrons and positrons (lepton component) [25]. The baryon component is composed of 87 % protons, 12 % helium ions (alpha particles) and the remaining 1 % heavy ions of higher charge as seen in Figure 1.4a.

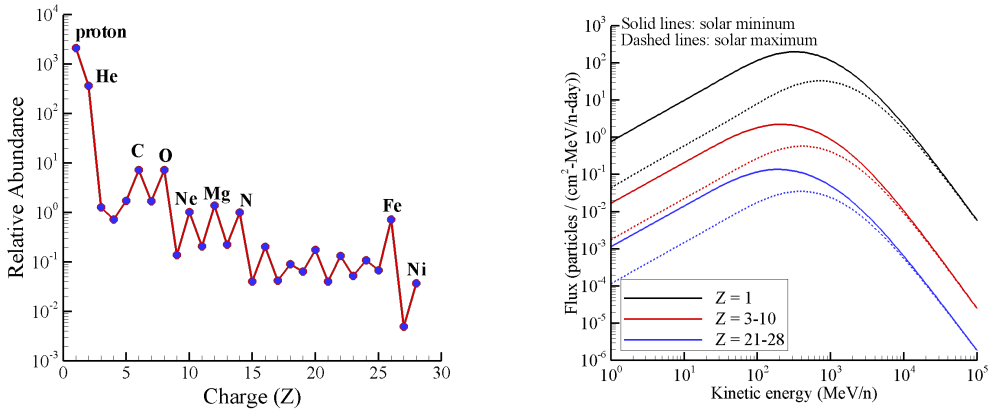

(a) (b)

Figure 1.4: (a) Relative GCR element abundances (H-Ni) recorded in 1977, normalized to neon. (b) GCR flux at solar minimum and maximum for different element ranges [26].

GCR spectra for three different element ranges are shown in solar minimum and maximum in Figure 1.4b. The flux of incoming particles to their respective energies peaks within the solar system around 1 GeV per nucleon [5]. The solar magnetic field modulates the lower energy particles and can shift the peak to higher energies. Since the GCR particles are charged, they are affected by the varying IMF. The flux scales inverse with the solar cycle.

Depending on their energy, protons of this origin can either penetrate tissue heavily or pass right through the astronaut and the spacecraft [27]. Fast charged particles moving through matter interact with the electrons of atoms in the material. The interaction excites or ionizes the atoms, leading to an energy loss of the traversing particle. In dosimetry linear energy transfer (LET) is used to quantity this, which is the amount of energy that an ionizing particle transfers to the material traversed per unit distance [28]. In space especially particles with high atomic number and energy (HZE) are important. Because of their high LET [29] and fragmentation capability, they have a large potential to cause radiobiological damage [30]. As seen above the GCR component is the main source for HZE particles in the solar system.

1.1.4 Secondary Particles

Secondary particles are sources of radiation that are mainly caused by primary particles interacting with the electromagnetic fields of celestial bodies or intervening matter. Around Earth mostly solar

particles can be trapped in belts around it. Nearly all spacecraft departing from Earth will have to traverse them. The two main destinations for human space flight, Moon and Mars, do not have strong magnetic fields like Earth and thereby this effect will not play the major role near these objects [31, 32]. Furthermore, interactions between GCRs and the surface or atmosphere of a celestial body can create secondary particles.

Trapped Particles in Earth's Radiation Belts

Near celestial bodies, that have their own magnetic field, exists a region where the IMF is not dominant, but particles are mostly affected by the magnetic field of the body. For example, Earth's magnetosphere influences the radiation environment within 6 to 7 Earth radii[3] (R_E) [33]. It can not only shield certain parts of impinging particles but also trap them around it. Earth is surrounded by intense regions of energetic protons and electrons referred to as the Van Allen Belts or Earth's radiation belts [6].

The geomagnetic field can be approximated by a dipole, creating coil shaped magnetic field lines as seen in Figure 1.5a. Earth acts as a magnetic dipole trap where charged particles with low mass such as electrons and protons nearly cancel their velocity parallel to the magnetic field lines [34]. This results in a spiral motion around the field line. At the magnetic poles the magnetic field line density increases and the small parallel motion of the particles is stopped and reversed. This causes the particle to be trapped and bounce back and forth between the magnetic south and north pole. In addition the ions drift slowly between the magnetic field lines, resulting in a clockwise rotation around the earth for protons and an anticlockwise motion for electrons.

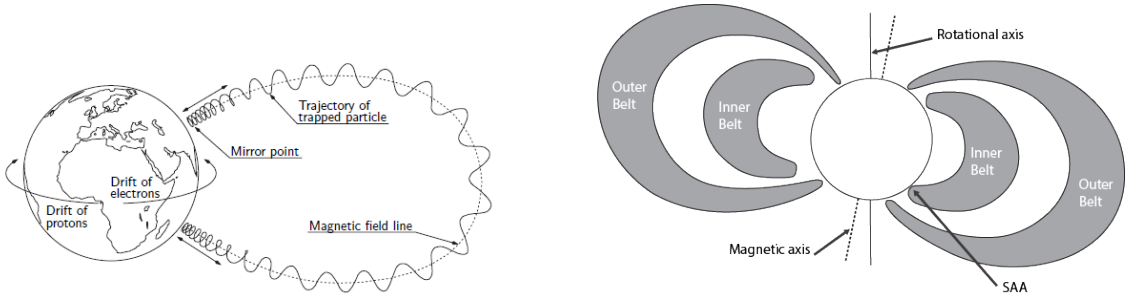

(a) (b)

Figure 1.5: (a) Motion of a trapped ion along a magnetic field line of Earth. (b) Two major belts of electrons and protons around the earth shown with respect to magnetic and rotation axis [35].

This trapping creates two belts around Earth as seen in Figure 1.5b. Both belts contain electrons that come from the SPEs. The inner belt extends to about 2.4 R_E and consists mostly of electrons with energies less than 5 MeV. The outer belt contains electrons with energies up to 7 MeV and extends from about 2.8 R_E to 12 R_E [36]. Especially this outer belt varies in size inversely with solar activity. Trapped protons occur only in the inner region with an energy of tens to several hundred MeV and form a broad peak between 150 MeV to 250 MeV [37]. These protons are the result of GCRs hitting Earth's the atmosphere and creating so-called albedo protons.

The displacement of the magnetic field with respect to the rotation axis of Earth creates a misalignment of the magnetic poles with respect to the rotational poles. This effect and the motion inside the molten iron core of the earth create disturbances. As a result, in a region above the coast of Brazil the magnetic field is weaker [6]. The inner proton belt can reach up to an altitude of 200 km in this so-called South Atlantic Anomaly (SAA).

[3] R_E = ca. 6360 km

Other Particle Sources

When primary radiation particles interact with intervening matter, either nuclear interactions or fragmentation takes place. These interactions can occur when GCRs hit the hull of a spacecraft or atmospheres [5]. Due to the highly relativistic nature of these interactions, their products are highly boosted in the forward direction. This results in so-called particle showers or cascades. They consist of different types of particles with varying energies and lifetimes. Thus the radiation can change drastically compared to the primary radiation [38]. Typical secondary particles are protons, neutrons, γ-rays and pions. α-particles, deuterons, tritons and other heavier nuclei can also be produced by the HZE elements of GCRs [20].

A further secondary source of radiation are albedo particles. These occur near celestial bodies that can reflect or stop high energy cosmic particles. Especially on bodies like Moon and Mars, where nearly no atmosphere or magnetic field is present, this effect is a strong source of particles. They are generated by interactions of high energetic particles with the planetary surface with trajectories pointing back to space [5].

1.2 Physics of Radiation Interactions

A charged particle with a mass large compared to an electron traversing matter loses part of its kinetic energy via electromagnetic interactions within the surrounding material. It can cause excitation and ionisation to the atoms of the matter along its track. This effect can be described by the Bethe Bloch formula shown in Equation 1.1 [39].

$$-\frac{dE}{dx} = \frac{4\pi e^4 z^2}{m_0 v^2} NZ \left[\ln \frac{2m_0 v^2}{I} - \ln\left(1 - \frac{v^2}{c^2}\right) - \frac{v^2}{c^2} \right] \tag{1.1}$$

and

$$-\frac{dE}{dx} = S \tag{1.2}$$

Where S is the so-called stopping power. It is the differential energy loss per unit length of traversed material.

In these expressions, v and z are the velocity and charge of the primary particle. The number density and atomic number of the absorber atoms are N and Z. The constants m_0 and e are the electron rest mass and the electronic charge. c is the speed of light. The parameter I represents the average excitation and ionization potential of the material. It is an experimentally determined parameter for each element. For non-relativistic charged particles ($v << c$) the second and third term inside the brackets can be neglected.

Material properties are only entering the equation via I, N and Z. Comparing different types of charged particles with the same velocity impinging on the material only z changes. Particles with greater charge will have larger specific energy loss. Figure 1.6 shows such a stopping power versus the momentum of a muon in copper to illustrate this equation.

Equation 1.1 is only valid with in the marked region from about 0.08 GeV/c to 70 GeV/c. Particles with lower energies are not fully ionised and the equation does not apply. For larger energies, radiative losses dominate the energy loss of the particle. The point of minimum ionization marks the minimum energy that a particle needs to ionize a matter atom. Such a particle is called minimum ionizing particle (MIP).

Below the MIP point the particle will initially deposit slowly increasing fractions of its energy in the surrounding matter. With decreasing kinetic energy, the stopping power rapidly increases. Thus, the particle deposits a significant fraction of its energy at the end of its trajectory.

Figure 1.7 shows such a energy loss along the track of a charged particle plotted against the traversed distance within the material, which is known as a Bragg curve. Near the end of the track the curve

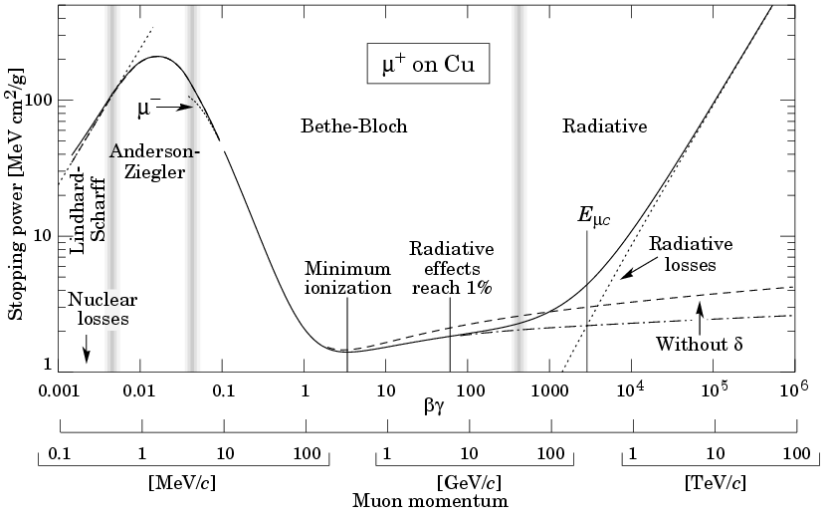

Figure 1.6: Mass stopping power versus muon momentum in $\beta\gamma$ (with $\beta = vc$ and γ being the Lorentz factor) [40].

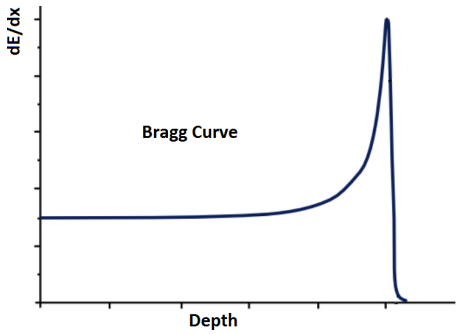

Figure 1.7: Schematic Bragg curve in relative stopping power versus depth [41].

peaks and falls off rapidly as the particle is stopped completely within the material. This peak is characteristic for the material used as well as for the impinging particle.

One can use this to differentiate between different particles, as high energy particles take longer to stop within the material or only lose some energy and do not stop in the material resulting in a flatter curve. With this method called Bragg curve spectroscopy the energy and charge of incoming radiation can be measured [42].

1.3 Effects of Radiation

Radiation affects electronic hardware and causes complex effects in semiconductor logic that degrade electronics over time. High energy radiation such as GCRs can lead to single and random bit flips or transistor errors in electronics, which can lead to malfunctioning components [43, 44].

But radiation is also harmful to human tissue. A measurement of the amount of radiation received is the absorbed dose. The absorbed dose takes account of all charged particles that were produced in or enter a unit volume [28]. Its value is derived from the mean value of the stochastic quantity of energy imparted and does not reflect the random fluctuations of the interaction events. From the absorbed dose one can derive the mean absorbed dose in an organ or tissue, which is weighted by a radiation-specific factor to determine the equivalent dose in the specific tissue. The equivalent dose can be weighted with a tissue-specific factor to get the effective dose [39]. This process is highly dependent on the used models and weights.

The unit for the absorbed dose is gray (Gy). One gray is the deposit of one joule of radiation energy per kg of matter or tissue. Equivalent and effective dose rates are often measured in sievert (Sv). One sievert represents the equivalent biological effect of one joule of deposited radiation energy in one kilogram of human tissue.

Different kinds of radiation have different effects in biology. LET can help in understanding how much energy was deposited by a particle along the track. It is depending on the energy and the particle type and can be approximated as the stopping power [45]. Though biological effectiveness of radiation can be determined by LET directly [46, 47], for a more precise calculation and the depth dose distribution particle dependent energy spectra are needed [48].

What effect space radiation has on humans is a complex question which is subject to current research as the known data sets result from atomic bomb tests and droppings over Japan. Since these events were composed of low LET γ-rays and α-particles, they can not be used to understand effects of high LET HZE particles [49, 50]. One can categorize effects as long or short term. Short term problems are usually related to high radiation exposures over a short period of time. Depositing large amounts of energy while traversing it, radiation can directly destroy cells or cause DNA strands to break up [51]. A large number of cell deaths can cause radiation sickness. Also cataract development is considered within this scope [52]. Long term effects are problems that arise over an accumulated radiation dose which can also be of low rate. DNA altering processes increase risk of carcinogenesis [1]. Cancer, digestive and respiratory diseases and immune system dysfunctions can develop over time [52].

1.4 Radiation Measurement

Radiation detectors determine particular measurement quantities such as

- particle type and energy, and direction of flux
- dose deposition in the detector material and
- other dosimetric quantities such as lineal energy, which is a stochastic quantity and is a microscopic analog of the LET.

To monitor astronauts the determination of absorbed dose and dose equivalent is required. These can be measured by personal dosimeters worn on the body. Together with environmental monitoring, which gives radiation field data as an input for calculations, estimations of dose rates in the human body can be made [52].

Several types of instruments are available. Each detector technology has its advantages and disadvantages. Some of the currently used technologies will be discussed (for more information see [52]).

A single device is not capable to determine the required dose quantities for all components of the radiation field. The absorbed dose and dose equivalent cannot be calculated from just a single component as there are large variations in the relative contributions from the different particle types.

1.4.1 Active Devices

Active devices are detectors that need electrical power to operate. Most often they record and display data in real time or near real time. They can measure flux rates as well as time-integrated values.

Tissue-equivalent Proportional Counters

One of the most common ways of measuring ionising radiation is by collecting the number of ions that have been created in a gas exposed to radiation. Such a proportional counter filled with a tissue like material or gas (methane or propane based) is called a tissue-equivalent proportional counter (TEPC)

[53]. The charge produced by an ionising particle traversing the gas chamber is collected and the signal can be related to the energy loss of the crossing particle in that simulated tissue volume. This type of instrument measures both the LET and the absorbed dose in tissue.

Semiconductor Devices

Silicon diodes can be used for the detection of charged particles. They record the energy deposited of the traversing charged particle in the sensitive volume of the detector. The ratio of the deposited energy to the thickness of the detector yields the approximate LET. This information can be integrated to give the accumulated dose and dose rate for charged particles in the detector material. In combination with conversion coefficients the tissue dose can be determined. Several detectors combined to an array can be used as a telescope to enable spatial resolution. Due to size limitations these devices often do not cover all angles but are restricted to a solid angle.

Direct Ion Storage Devices

Direct ion storage devices combine an ionisation chamber with a semiconductor device. Charges produced by a traversing particle inside a gas chamber are stored to a non volatile semiconductor memory cell. These detectors are used to estimate accumulative dose rates over several hours to years. Absorbed dose rates from heavy ions can be estimated well with these devices, but low energy charged particle rates depend on the chamber wall thickness and material.

1.4.2 Passive Devices

No single passive device is capable of dose measurement across the full energy and direction distribution of particles available in space. All passive devices must at least record the accumulative energy deposited by all types of radiation particles in their active material, referred to as the total ionizing dose (TID).

Luminescence Detectors

Most passive personal dosimeters in use are thermoluminescent dosimeter (TLDs). Small crystals that show luminescence after exposure to ionising radiation are embedded in such a device. When controlled heating is applied, the crystal releases the trapped energy in the form of visible light. Its intensity is proportional to the intensity of the ionizing radiation the crystal was exposed to. By multiplying with a suitable coefficient one can relate the intensity to the absorbed dose. Other technologies that behave similarly to crystals are also used. These devices show strong inverse LET dependences above $10\,\mathrm{keV\,\mu m^{-1}}$ [52].

Nuclear Track Detectors

For detection of high LET components of the radiation field nuclear emulsions can be used. A charged particle passing through the material leaves a trace which can then be viewed with a microscope. Nuclear emulsions can determine the charged particle type and its direction in the detection medium. They are mostly insensitive to radiation with LET in water lower $10\,\mathrm{keV\,\mu m^{-1}}$ [52].

Combined Detector Systems

A combination of a low LET and a high LET detector can allow the determination of dose equivalent over a broader LET range. For example cut-off points for insensitivity couple very well when TLDs and nuclear track detectors are combined.

1.5 Radiation Environment Aboard the International Space Station

The radiation dose aboard the ISS is mainly dominated by the protons arising from the SAA as it is frequently passed by the spacecraft. On the outside, the electrons of the Van Allen belts are more dominant [54]. The GCR contribution is highly dependent on the current inclination of the spacecraft as the flux increases with higher latitudes. The interaction of GCR components with the matter of the ISS increases the complexity of the radiation environment inside the spacecraft by processes described earlier. Variations in the primary external radiation field and in the mass distribution of the spacecraft will change the relative contribution of each component to organ and tissue doses. The equivalent dose aboard the ISS reach from $80\,\mathrm{mSv\,d^{-1}}$ to $180\,\mathrm{mSv\,d^{-1}}$ [55]. The difference in shielding material and thickness at each location results this broad range as well as the time of measurement as the radiation sources do vary over time.

The environment aboard has been studied since the deployment 1998 and is therefore reasonably well understood. As described above, the ISS experiences some parts of the radiation which would be present during a deep-space mission that is not as easily accessible for a long period of time at the surface of Earth. It can thereby serve as a controlled and easily accessible test environment for missions like the RadMap Telescope.

1.6 Radiation Environment in Deep Space

Dose rates in deep space are much higher than on Earth or in a low Earth orbit due to the lack of shielding by the atmosphere and the magnetic field of Earth [55]. The main contributions are the isotropic GCR background and particles radiated by the Sun. The equivalent dose rate in LEO and on Mars is about 180 mSv per year, compared to about 3 mSv per year on Earth. In deep space it ranges from $180\,\mathrm{mSv\,yr^{-1}}$ to $600\,\mathrm{mSv\,yr^{-1}}$ [1]. This is significantly higher, since no magnetic field nor an atmosphere is stopping GCR or SPE particles. Even further into space the effects of the Sun become weaker and the GCR background is the main contribution to the overall radiation dose. Additionally the environment is influenced near large objects such as moons and planets by the disturbances in the IMF. Also, the solid angle to the Sun can be blocked by the body itself creating a shielding effect. Intravehicular radiation in form of secondary particles by interaction of GCRs with matter is always present and contributes at all locations.

As the mission time exceeds easily one year for deep space missions as even a mission to the nearest planet, Mars, takes several months of transit time, time-dependent effects of the already mentioned sources have to be taken into account [5]. As discussed the solar modulation and activity can lead to vastly changing radiation environments. Estimations show that deep space missions impose higher risks of exposure induced death (REID) by cancer of up to 40 % over the 3 % which is NASA's radiation standard limit on astronauts [1, 56]. This high REID estimation has high uncertainties rising from a lack of HZE particle understanding and model differences. For other less studied diseases with respect to radiation, the REID are heavily model-dependent and suffer from insufficient data sets [2]. For an advanced understanding of human space flight risks these data sets are required.

Different dosimeters and spectrometers are deployed and have been tested on the ISS to characterise the radiation environment [57, 54, 58, 55] to get a better understanding of the biological effects that arise especially from GCRs and SPEs.

The sensor suit currently deployed to measure radiation inside the ISS lacks sensitivity to heavy ions and cannot measure the energy- and angle-dependent radiation spectrum in real time [59]. But, as discussed, HZE particle effects are not completely understood. The ability to monitor the radiation environment and thereby the space weather is key for astronaut safety and dose reduction. This monitoring has to happen near real time or in real time to have the ability to react quickly and deploy countermeasures to sudden changes in the radiation field, as SEP can impose on the spacecraft. Measurement analysis has to be done on-site since deep-space communication technologies cannot

deliver the data rates required to transmit the data sets involved and as data can only be transported with a maximum speed of the speed of light, deep-space missions always lack real-time communications [60].

Chapter 2

The RadMap Telescope

The RadMap Telescope is a technology demonstrator to validate new radiation measurement concepts for future deep-space missions. It will soon be deployed for half a year aboard the ISS where it can be tested within a controlled environment. The goal is not to perform more accurate measurements than other more specialized devices currently deployed, but to combine the used measurement technologies (spectrometers and dosimeters) in a compact device. This can save precious weight and room inside a spacecraft and reduces the system complexity of several different detectors to only one device.

It aims to measure the energy- and angle-dependent radiation spectrum of protons and HZE particles and to provide dose rate measurements in near real time. The telescope has a complete solid angle acceptance and can be deployed anywhere inside a spacecraft only restricted by power and communication limitations of the mission. This enables a quick relocation within the spacecraft to measure the shielding effectiveness and radiation environment in different locations quickly and with less uncertainties especially on time-dependent effects as arising from the need of other instruments to turn multiple times to cover the complete solid angle. Because of its small form factor its particle identification capabilities cannot cover the full energy range of the radiation environment. The RadMap Telescope focuses on particles with energies most harmful to human tissue and organisms, i.e. those with energies of tens to hundreds of MeV per nucleon.

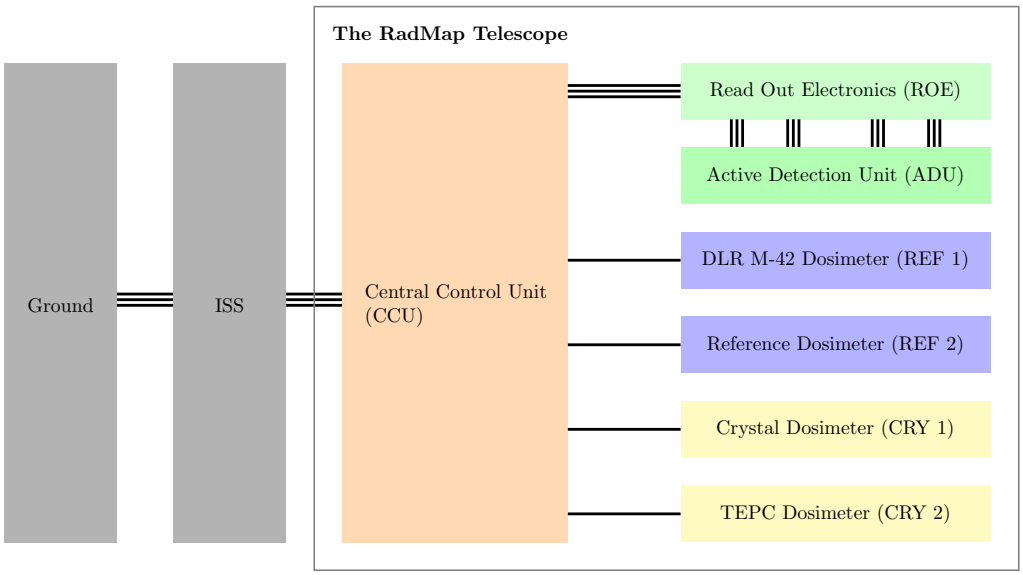

Figure 2.1: Schematic overview of all systems inside the RadMap Telescope.

As seen in the schematic overview in Figure 2.1 the RadMap Telescope has five different detector systems. A main active detection unit (ADU) and two reference dosimeters (REF 1 & 2) as well as two crystal dosimeters (CRY 1 & 2). These are managed by the flight computer or central control unit (CCU), which is the main focus of this work. It collects and processes the data and sends it via the ISS to Earth.

2.1 Detector Systems

The five different detectors use different technologies to measure particle ID, energy and dose rates. In the following the ADU, REF 1 & 2 and CRY 1 & 2 operating principles and functions will be explained.

2.1.1 Active Detection Unit

The main sensor is the Active Detection Unit (ADU). It uses 1024 scintillating fibers made of polystyrene to detect passing particles within an active volume of 512 cm^3. They are arranged in four stacks with eight layers and 32 fibers on each layer as seen in Figure 2.2. Every other layer is rotated by 90 degrees. Layers with the same orientation have a small offset to each other to cover the space created by the slight gap between each fiber. This enables a reconstruction of the 3-dimensional track of the ionising path of a traversing particle by combining the information of the two 2-dimensional projections imposed by the different layer orientations.

Figure 2.2: ADU of the RadMap Telescope: Exploded view of the fiber stack shows the alignment and sectioning.

The polystyrene fibers are an aromatic organic compound of hydrated carbon. Benzene rings in the material provide delocalised electrons, which can be excited by an incoming particle. Transitions between intramolecular vibrational excitation states cause a de-excitation, which produces light. The process of excitation and de-excitation of molecules within the absorber material is called scintillation.

In the case of pure polysterene the light is emitted in the ultra-violet regime. To ensure that the emitted photons reflect via total reflection to the end of each fiber a wavelength shifting additive has been added to the material. It shifts the wavelength emitted by the benzene rings into a different wavelength via absorption and emission. This also ensures that the light passing through the fiber is not reabsorbed, as the emitted wavelength of the shifting material is chosen not to excite Polysterene.

A silicon photomultiplier (SiPM) glued to the end collects the light which is converted by the photoelectric effect into electrons. The silicon consist of a junction between an electron-rich and an electron-depleted region of the semiconductor multilayer material. Applying a reverse bias voltage sets up an electric field across the junction. It will cause charge carriers to be accelerated towards the anode (holes), or cathode (electrons). An electron-hole pair is created by the photoelectric effect and traverses to the border of the two regions through the imposed electric potential. It has sufficient kinetic energy to create secondary charge pairs through the process of impact ionization in a so-called avalanche [61]. The junction will break down and become conductive. This amplifies the signal of the electron-hole pair to a macroscopic current flow [62]. To create a sufficient current from only a single electron-hole pair high voltages have to be applied to create a high electric field for the avalanche effect. This is called Geiger mode [63]. Changes in temperature of the material result in different material behavior and can lead to higher dark count rates [61]. To obtain consistent results temperature changes have to be compensated for by altering the bias voltage.

The advantages of using a silicon photomultiplier instead of other technologies are their mechanical stability and electromagnetic resilience, which is even more important in space than in ground application as the start of a rocket imposes strong vibrations and acoustic noise [64]. Also, they are sensitive to single photons and can detect a broad energy range at the same time [65], which improves the accuracy of the device. The SiPMs (PM3325 [66]) are manufactured by KETEK and provide a peak-sensitivity close to the peak-emission wavelength of the scintillating material used to achieve the best possible detection efficiency. To ensure that no stray light is coming to the detector that would disturb the measurement, the fiber stack is placed in a opaque compartment.

The produced voltages of the SiPM are digitised by the IDE3380 application-specific integrated circuit (ASIC) 12-bit analog to digital converter (ADC) by Ideas [67].

The ADU has been tested and characterized in previous works of the research group led by Prof. Paul (E18) and it was shown that it can reconstruct proton energies between 30 and 70 MeV with a resolution of better than 1 MeV [68, 69].

In total 64 ASICs (16 channels each) are used to digitise the 1024 SiPM channels. The digitised information is then filtered for noise and trigger conditions are applied to clean up the signal. This is done inside a Xilinx Artix-7 field-programmable gate array (FPGA). Compared to integrated circuits (ICs), where the structure and functionality of the built-in logic gates can not be altered after manufacturing, a FPGA is designed to be configured by the customer after manufacturing. This enables the adaption of filter and trigger conditions during operation and makes an optimisation of the detection efficiency possible. The ASICs together with the FPGA will be called read out electronics (ROE), where the FPGA is the ROE base, which is connected to the CCU.

Simulations by T. Pöschl (E18) have shown that a maximum hit rate of 1 kHz can be expected for the deployment aboard the ISS, while on average the event rate is 0.1 kHz. The maximum data and mean data rate which have to be sent to the CCU assuming that all fibers receive a hit are given by the following equations:

$$1\,\mathrm{kHz} \times 1024 \times 12\,\mathrm{bit} = 12.3\,\mathrm{Mbit\,s^{-1}} \tag{2.1}$$

$$0.1\,\mathrm{kHz} \times 1024 \times 12\,\mathrm{bit} = 1.23\,\mathrm{Mbit\,s^{-1}} \tag{2.2}$$

This data rate is a crude estimation and real world data rates probably are much lower, as this is calculated with all channels receiving a signal and the triggering by the FPGA is not taken into account.

The data provided by the ROE will be analysed by artificial neural networks aboard the CCU. With these networks the instrument is able to analyse the ADU data aboard the spacecraft and deliver near-real-time particle spectra and dose rates.

The artificial neural networks have to be trained by machine learning prior to use. The networks use an end-to-end open source platform for machine learning called TensorFlow for data training

and evaluation. The training and evaluation process is discussed in detail in the master thesis of M. Höschler [70].

If a trigger condition is specified by three fibers or more showing hits and one can project these hits in two planes, the measurement data will be collected by the CCU. It is processed via artificial neural networks or saved as raw data to the persistent storage on the CCU. First, the impact angle on the detector will be determined by a specialised network. Furthermore, a second network will analyse the data for particle energy and charge. The raw data of the ADU will be stored for particle events that the networks cannot categorise as well as in the beginning of the mission to determine the performance of the artificial neural networks. The particle data can be used to calculate the dose. Early networks show a need for at least 1 GB of random access memory (RAM) to store data temporarily.

One of the main focuses of the demonstrator mission aboard the ISS is the understanding and characterisation of these networks and their performance when supplied with on-orbit data. The networks are subject to change during the mission and a CCU architecture has to be chosen to accomplish this. The aim is to have well-known and flight-proven networks for future space missions that run on optimised hardware.

2.1.2 Reference Dosimeters

As the ADU is tested but not flight-proven with real data, the RadMap Telescope includes two flight-proven sensors to record the TID and compare calculated dose rates with.

The M-42 dosimeter (REF 1) developed by the German Aerospace Center (DLR) uses a planar silicon PIN photodiode with an active area of $1.23\,\mathrm{cm}^2$ [71]. The amplified signal is digitised and sent to a microcontroller, where the spectral data is stored and easily accessible via a user interface. The RadMap Telescope uses a version with a universal asynchronous receiver-transmitter (UART) interface. Different variants of this detector have been tested successfully on airplanes and sounding rockets. It can record energy depositions from 60 keV to 18 MeV. Based on this the absorbed dose in Silicon and the commonly used absorbed dose in tissue or water is calculated. The M-42 will be part of the measurement suite of the MARE experiment on NASA's upcoming Artemis-1 mission [71].

A second dosimeter (REF 2) is used for referencing. The exact details are not fixed yet, but it will be a commercially available solution, that produces analog voltages to indicate the dose rate. The analog data will be digitised by an ADC and can be collected by an attached microcontroller.

2.1.3 Crystal Dosimeters

Additionally to these sensors, two inorganic scintillator crystal detectors are used. They use similar technology as the ADU. Inorganic scintillator crystals are high density and high atomic number materials and can be made quite small to achieve reasonable stopping powers. Compared to the scintillation process of organic materials crystals create light by the absorption of the incident particle and conversion of the energy into thermalized electrons and holes [72]. A fraction of the pair's energy is transferred to luminescence centers where the actual light emission process works in the same way as in organic materials. Because this process is thermal rather than electrical, it can be used to detect uncharged particles as well, such as neutrons and gamma rays [72].

Four of the PM3325 SiPM and one IDE3380 ASIC are used to collect the photons and digitise the signal in each device. The total ionizing dose is then calculated by a microprocessor.

One device will be unshielded (CRY 1) and the other device will be surrounded by tissue-equivalent plastic (CRY 2). These devices have not been tested and the sensitivity and resolution will be compared with the two flight-proven dosimeters. The crystal dosimeters complement the ADU's measurement capabilities in the range of uncharged particles and lower energies.

2.2 Physical Dimensions

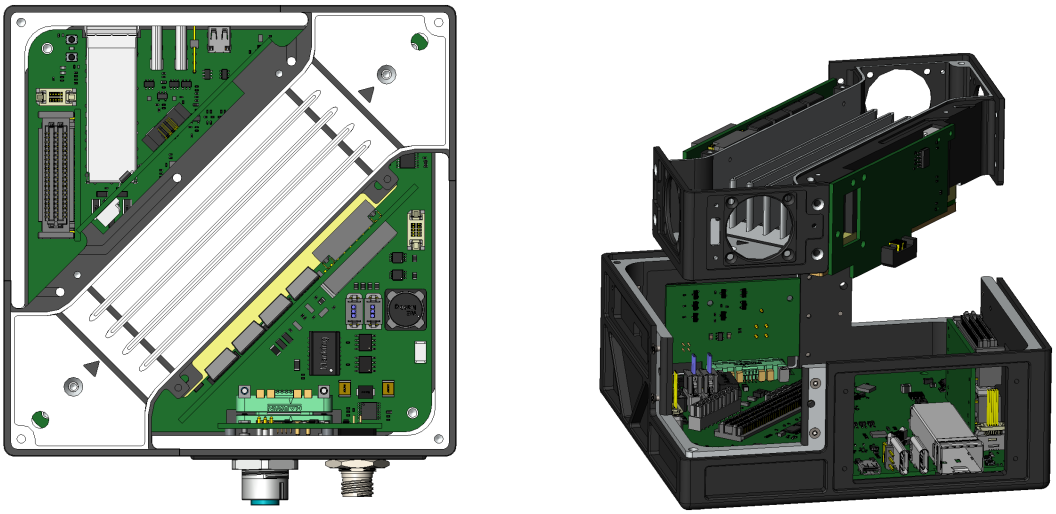

(a) (b)

Figure 2.3: Lower compartment of the aluminium case of the RadMap Telescope: (a) Top view and (b) an exploded view of the compartment.

The aluminium case of the RadMap Telescope is separated into two compartments. A cooling channel is placed diagonally between opposite corners of the lower compartment (Figure 2.3). It has two fans on each end to provide a steady air flow for cooling as in space no natural convection takes place due to weak gravitational fields. The CCU, the power distribution unit (PDU) and a Wi-Fi transceiver module are placed in contact with it underneath and on opposite sides respectively to provide cooling to the heat emitting components. Ports for power and an Ethernet connection are located on one side of the lower compartment. Wi-Fi antennas are placed underneath a plastic cover on the side of the outer hull to prevent signal blocking by the case. A service hatch gives access to debug and test connections of the CCU and the ROE on one side of the compartment. It is only used during development and is otherwise covered by a plate.

The upper compartment is dominated by the ADU and the ROE. The cooling channel of the lower compartment also cools the FPGA from the bottom. The ADU is placed in the middle with the ROE directly attached at its sides. The other sides of each board is attached to a cooling channel for each side of the ADU (excluding top and bottom). Each cooling channel has two fans to create air flow. At the top REF 1 and 2 are placed beside CRY 1 and 2 behind a protective cover.

In total the RadMap Telescope is $13 \times 13 \times 15\,\mathrm{cm}^3$ in size and weighs about 3.5 kg.

2.3 Data Acquisition

The flight computer (CCU) is collecting all data produces by the attached detector shown in Figure 2.1. In this work, components such as REF 1 or the ROE will be called nodes. The master over all systems is the CCU while all detector systems act as slave nodes to it. This means the CCU has to initiate the communication between node and master.

Unprocessed data provided by the ROE or processed data from the artificial neural networks is considered as science data. Dose rates collected from CRY 1 and 2 as well as REF 1 and 2 are addressed as dose data. Information of the overall system such as operating temperatures, voltages or available storage space is seen as telemetric data.

Telemetry and dose rates from REF 1 & 2 and CRY 1 & 2 are collected in constant intervals by the CCU. Data from the ROE is collected after a prior notification by the FPGA.

Details about the chosen interfaces and protocols are provided in the respective sections of their hard- and software implementation later.

2.4 Interfaces

The RadMap Telescope needs only three interfaces to operate: Power for the whole system has to be provided via the plug on the side of the case. Two networking solutions are given to transfer the data to a nearby network. The physical attachment point on the underside of the device uses the seat track standard mounting also found on aircrafts [73].

2.4.1 Power

The RadMap Telescope uses the 28 V direct current operational power provided from outlets inside the ISS [74] for its main power. It has to be attached via the power port at the side.

Main power is then split into six different power domains to be able to switch certain components on or off as needed (Figure 2.4).

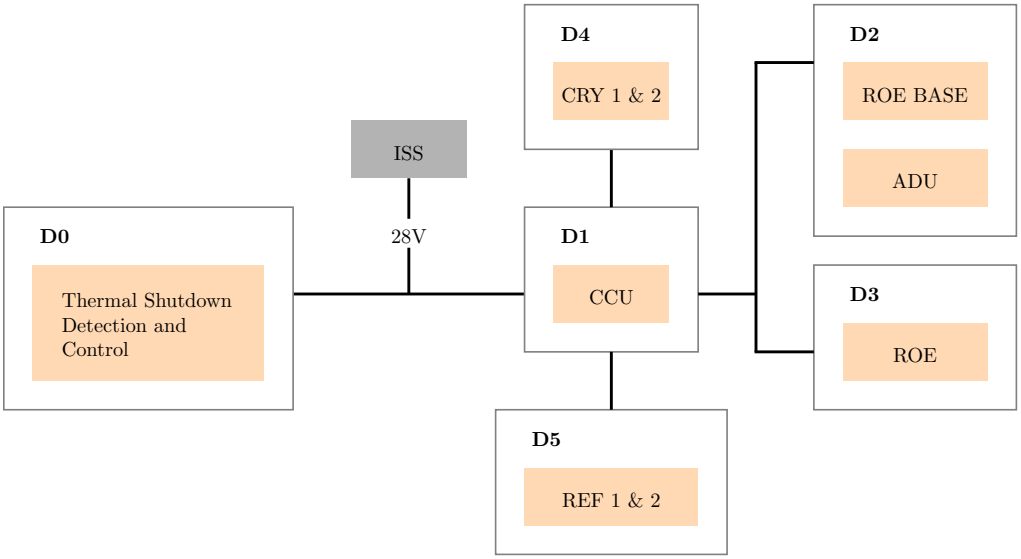

Figure 2.4: Power distribution: Main power provided by the ISS (28 V) are split in different domains, which power certain components of the instrument.

D0 is always on when power is provided from outside. This is the most important power domain as it provides power to the thermal shutdown system. A thermal shutdown is initiated, if the temperature on the outside of the case is getting over 45 °C. The RadMap Telescope will then shutdown all systems (expect the thermal monitoring system) until it has cooled down. This prevents harming of astronauts, while they touch the device and is a requirement for payloads accessible by humans aboard the ISS [74].

D1 provides all power required for the operation of the CCU, in particular to all peripheral IO such as Ethernet and also all sensors on the CCU board. Some power is converted here to lower voltages which are provided to other domains.

D2 and **D3** are powering the FPGA as well as the ROE. The SiPMs do also need power from these domains.

D4 and **D5** provide power to the CRY 1 & 2 as well as to both reference dosimeters.

Power domains are turned on according to four different operating modes seen in Table 2.1.

Table 2.1: Active power domains in operating modes of the RadMap Telescope.

domain active	D0	D1	D2	D3	D4	D5
ccuOnly	x	x				
telemetry	x	x				
dose	x	x			x	x
science	x	x	x	x	x	x

These modes are used in commissioning of the device and also in case a thermal shutdown requires the system to be booted up slowly to search for the failing component.

- **ccuOnly**: The CCU is on, but all domains including all detectors are disabled. This mode will be activated when a thermal shutdown has occured.
- **telemetry**: This mode provides only telemetry of the RadMap Telescope. All detectors are off.
- **dose**: Additionally to the telemetry mode also dose data of REF 1 & 2 and CRY 1 & 2 are collected and sent to ground.
- **science**: The science mode enables in addition to the dose mode also the ADU.

2.4.2 Communication

Two different network interfaces can be used to communicate with the RadMap Telescope. A wired connection port near the power connector can provide Fast Ethernet with speeds up to 100 Mbit s^{-1}. A dual-band IEEE 802.11ac wireless transceiver by Doodle Labs (ACM-DB-2) [75] can provide data rates up to 860 Mbit s^{-1}. The transceiver has a mini Peripheral Component Interconnect express (mPCIe) [76] interface to communicate with the CCU. The joint station local area network aboard the ISS is used for both interfaces.

The communication and tracking System of the ISS uses several different subsystems [74]. Data can be transferred most predominately over the Tracking and Data Relay Satellite System (TDRSS) between the ISS and ground as seen in Figure 2.5 [77]. Several satellites (TDRS) in higher orbits than the ISS provide different down and up stream services to the ISS and ground stations on Earth. The NASA Integrated Services Network (NISN) is used to communicate the data from or to the mission control center (MCC). Over the years different frequency bands for radio communication with the ISS have been added. Currently Ku (12 GHz to 18 GHz) and S band (2 GHz to 4 GHz) frequencies are in use and provide different payload data rate links for services on the station [78]. Downlink coverage varies from 70 to 85 percent [78] based on the ISS attitude and location.

The RadMap Telescope is allowed to transfer its packages via both a wired and wireless Medium Rate Data Link (MRDL) aboard the ISS with up to 100 Mbit s^{-1}. It uses the Ethernet 802.3 standard and User Datagram Protocol (UDP) [78, 80]. During periods of signal loss between station and TDRSS, the ISS Integrated Communications Unit (ICU) nominally records MRDL payload data that would have been transmitted to ground otherwise. The station automatically transmits the data when a connection is established again.

The RadMap Telescope uses NASA's Telescience Resource Kit (TReK) [81]. It is a suite of software applications used to monitor and control payloads aboard the space station. It enables a remote access to the instrument from ground based laboratories and can be used to receive payload data from the ISS.

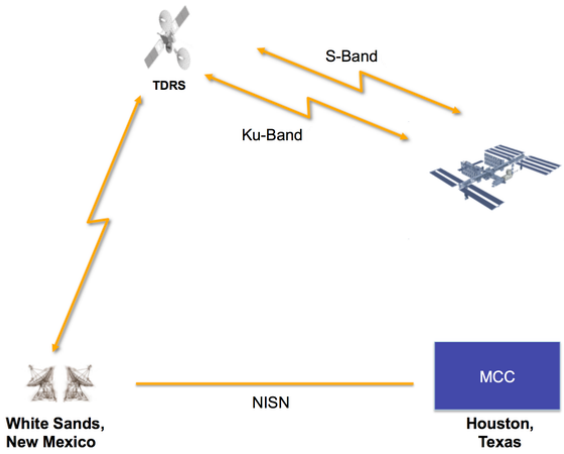

Figure 2.5: Simplified scheme of the communication architecture between ISS and mission control center [79].

The ISS provides a network-attached storage (NAS) for payloads, where raw ADU data will be transferred to. NASA systems automatically mirror the stored data of the NAS to a similar device on ground. The raw data can then be accessed to be processed without artificial neural networks and to train new networks.

NASA also provides a direct connection to the instrument for maintenance and commanding which can be used like a Secure Shell connection. Additional commanding capabilities in the form of commanding packages sent from ground may also be used.

Two different data package types are provided by the RadMap Telescope: Telemetry and dose as well as science information packages. Science packages include only information about neural network process ADU data and a dose rate calculated from ADU data. This information is sent in real time as soon as new data is available. Telemetry and dose packages provide basic instrument statistics and the calculated dose rates of the reference and crystal dosimeters. They are sent every 5 s.

As the key components are defined, the exact design of the flight computer for the demonstrator mission and a more detailed system architecture are still missing. Exact interfaces between each component have to be defined and verified. The development of the CCU and the detailed system architecture is the subject of the next chapters. The design of the flight computer especially is focused on the demonstrator mission as it provides a test environment for the instrument's calibration and artificial neural networks. Future missions into deep space benefit from specifically on-orbit tested artificial neural networks and may use a different CCU architecture while keeping the overall system architecture presented here.

The design process includes the determination of the requirements for the demonstrator mission (chapter 3) and their implementation in hardware and software (chapter 4 and 5). The implementations are tested to check, if they fulfill all requirements as needed (chapter 6). A summary of the resulting system architecture is presented in chapter 8.

Chapter 3

Requirements

The design process of any component is confined by requirements, which are imposed by stakeholder needs and concerns. In the case of the RadMap Telescope CCU the following stakeholders have been identified:

- The Institute for Hadronic Structure and Fundamental Symmetries (E18) at the Technical University of Munich (TUM) wants to conduct the previously presented mission.
- The National Aeronautics and Space Administration (NASA) as one of the key operators of the ISS has to keep the astronauts and station healthy and operational.
- The launch provider, which most likely will be Space Exploration Technologies Corp. (SpaceX) with its Falcon9 and Dragon capsule, wants to ensure a safe journey to the ISS, which is preferably unharmful to the instrument.

In Table 3.1 all requirements are listed with their respective ID and stakeholder. The rationals to the requirements are presented in the following.

The requirements 01SpaceX to 03SpaceX serve as an example for the environment that could be present during the transfer of the instrument to the ISS. These requirements may differ from one launch vehicle to the other. They are taken from the DragonLab specification and Falcon9 payload user's guide [82, 83]. During transit the instrument is placed in shock absorbing foam within a cargo transfer bag. This reduces the load of vibrations and also ensures a temperature and pressure controlled environment.

NASA's main concerns are regarding the safety of the astronauts living aboard the station as well as the integrity of it (01NASA and 04NASA). As the RadMap Telescope will be placed on walls within the pressurized sections of the ISS, it will be easily accessible to nearby astronauts without prior removing covers or opening drawers. This imposes risks to the astronauts that can accidentally come in touch with the device, such as burning or open wounds. As the instrument is not allowed to create network loops (05NASA), E18 decided that an easy solution is to have no more than one network interface active at a given time.

As the CCU is an internal component most requirements are imposed by the instrument concept as already presented above. For these E18 will serve as a stakeholder with the main interest of conducting the proposed demonstrator mission and enable the system to be used in future manned and unmanned deep space missions. The requirements arise also from mentioned aspects of the system in the previous chapter (01E18 to 06E18). As the system is used for constant radiation monitoring it would be impractical to require constant interaction with a human and would not be suited for unmanned deep space missions. A human independent operation cycle is thereby needed (02E18). Rough estimations have shown that, as the RadMap Telescope demonstrator is not allowed to need more than 30 W (04E18), the CCU processor should not take more than half of it (05E18). Other requirements are imposed by the operation and functionality of the device (08E18 to 14E18).

To be able to locate a faulty component, which causes or may cause a thermal shutdown, information of voltages, power draw and temperatures used in the instrument should be provided (15E18 to 20E18). In case of a thermal shutdown and to buffer in- and outgoing data the CCU should have some non-volatile storage (21E18). Concerning the thermal understanding of the system the exact pressure of the environment, in which the instrument is being placed, is of use and should be measured (22E18). As a thermal shutdown indicates wrong behaviour of the instrument the knowledge of such an event is required to fix the issue (23E18). The RadMap Telescope may be relocated by the astronauts aboard the space station by their own. After such a change in the placement and possibly also orientation of the instrument has occurred, the information about it is important to analyse the measured data as different sections of the ISS have different shielding materials and thicknesses. It may occur that such a change in position is not communicated to the analysing team. In addition, for manned spacecrafts, where the humans can come in contact with the device during their other operations on the spacecraft, changes in the attitude of the device can occur after the instrument has be accidentally relocated by a human. Therefore the change in placement and orientation has to be monitored (24E18).

Table 3.1: All requirements imposed by the stakeholders (E18, NASA, SpaceX) to the CCU are listed sorted by stakeholder. For a rational please see text.

ID	Stakeholder	Requirement
01SpaceX	SpaceX	Components should withstand 10 °C to 46 °C temperature [82].
02SpaceX	SpaceX	Components should withstand 958 hPa to 1027 hPa pressure [82].
03SpaceX	SpaceX	Components should withstand the shock and vibration of the launch [83].
01NASA	NASA	Components have to withstand 17 °C to 28 °C temperature [78].
02NASA	NASA	Components have to withstand 1013 hPa pressure [78].
03NASA	NASA	Components have to withstand the shock and vibration of a astronaut hitting the case accidentally.
04NASA	NASA	Temperature of the case has to be below 45 °C.
05NASA	NASA	The instrument is not allowed to create network loops.
06NASA	NASA	The instrument can use the MRDL.
01E18	E18	The CCU has to fit inside the lower compartment of the aluminium case.
02E18	E18	The CCU should be able to produce and send dose rate data without the need of constant human interaction.
03E18	E18	All components should use as little power as possible.
04E18	E18	The instrument should not use more than 30 W.
05E18	E18	The CCU processor should not use more than 15 W.
06E18	E18	All components should be radiation tolerant or replaceable by radiation tolerant hardware.
07E18	E18	All components should be able to withstand −40 °C to 125 °C temperature.
08E18	E18	Artificial neural networks run on the CCU have to be able to process events with a frequency of up to 1 kHz.
09E18	E18	The CCU needs at least 1 GB RAM for the neural networks.
10E18	E18	The CCU needs a mPCIe capable interface.
11E18	E18	The CCU needs an interface capable to fetch at least 12.3 $\mathrm{Mbit\,s^{-1}}$ of data provided by the ROE.
12E18	E18	The CCU has to be able to collect data provided by the DLR M-42.
13E18	E18	The CCU has to be able to collect data provided by the REF 2 dosimeter.
14E18	E18	The CCU has to be able to collect data provided by the CRY 1 and 2 dosimeters.
15E18	E18	The CCU should be able to measure voltages of all power rails.
16E18	E18	The CCU should be able to measure electric current of all power rails.
17E18	E18	The CCU should be able to measure temperature on the outlets of all cooling channels.
18E18	E18	The CCU should be able to measure temperature of the FPGA.
19E18	E18	The CCU should be able to measure temperature of the ROE.
20E18	E18	The CCU should be able to measure temperature of all power converters.
21E18	E18	The CCU should have at least 512 MB of non-volatile storage.
22E18	E18	The CCU should be able to measure the pressure of its environment.
23E18	E18	The CCU should be able to measure a thermal shutdown.
24E18	E18	The CCU should be able to measure changes in its orientation and placement inside the spacecraft.

Chapter 4

Hardware

When searching for the right component, first the functionality is chosen and then the other specifications are compared with the requirements given in chapter 3. Especially components with a radiation tolerant variant are interesting for the instrument and its future missions into space to increase the reliability. For the demonstrator mission most often the non radiation tolerant version is used as it is not required in the controlled environment of the ISS and all the components have to be verified on orbit first. For better manufacturing and quality control, components with physical dimensions (also called footprint), that can be tested with the equipment of the available laboratories of E18, are preferred over others.

After the selection of one component, it is tested on a so-called breadboard, which is a test platform where ICs can be tested without the need of soldering of every connection. If this cannot be done due to the shape or complexity of the component, the manufacturer's or separately built printed circuit boards (PCB) are used to verify the components electric functions.

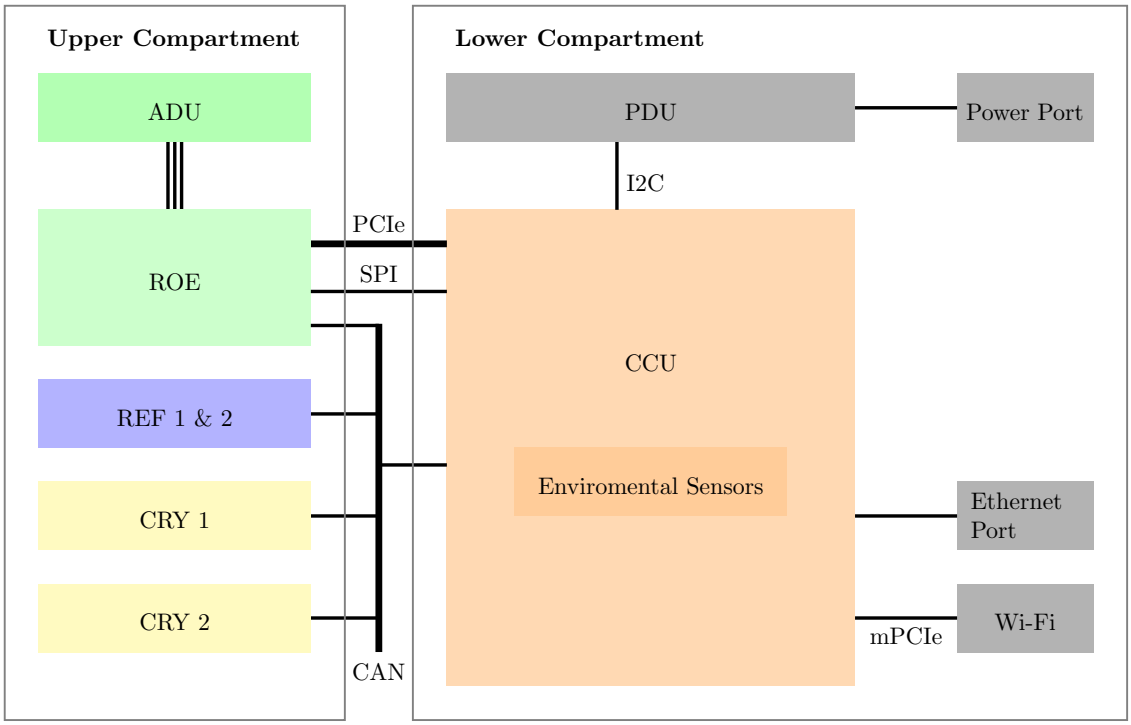

Figure 4.1: Schematic overview of the hardware system architecture of the instrument.

Figure 4.1 gives an overview of the RadMap Telescope system architecture, which will be discussed in the following sections. The CCU collects science data from the ROE via a Peripheral Component Interconnect Express (PCIe) [84]. The ASICs of the ROE, which read out the ADU, can be configured by the CCU via the Serial Peripheral Interface (SPI) [85]. REF 1 and 2 are combined into one node and share the same microcontroller. Dose and telemetry data of the ROE and the reference dosimeters (REF 1 & 2, CRY 1 & 2) is transmitted based on the Controller Area Network (CAN) [86]. Via an Inter-Integrated Circuit (I2C) bus [87] voltage and current information of all power domains from sensors inside the PDU can be obtained. Environmental sensors for pressure and orientation are also part of the CCU. Via the Ethernet port or the external mPCIe Wi-Fi card (Wi-Fi) communications to the ISS are established.

4.1 Processing Unit

The flight computer requires a device that can perform basic arithmetic, logic, controlling, and input and output (IO) operations. Such a device is called a central processing unit (CPU). This component will be evaluated first, as it will define the interfaces available for all internal data connections and has major influence on the system architecture.

The artificial neural networks impose requirements on processing power of the CPU. Parallel operating architectures are of special interest as it has been shown that artificial neural networks perform best on them due to their nature [88, 89]. They are also a component which will be developed further with the first on-orbit data and will be subject of change during the experiment.

As building such an architecture or processor is a complex task and the exact online processing power needed for the networks is not known, a solution with commercial available single board computers or system-on-chip (SoC) was chosen to have a significant performance overhead. As graphic processor units (GPUs) are built highly parallel [90], especially options with a built-in GPU were selected. Table 4.1 gives an overview of the modules, that will be evaluated in the coming sections for the main component of the CCU.

Table 4.1: Tested single board computers.

Product Name	RAM [GB]	GPU	FPGA
Xilinx Enclustra Zynq Mercury ZX1	1	No	Yes
Xilinx Enclustra Zynq Mercury+ XU1	4	Yes	Yes
Nvidia Jetson Nano	4	Yes	No
Nvidia Jetson TX2	8	Yes	No
Nvidia Jetson TX2i	8	Yes	No

Mercury ZX1 The Mercury ZX1 uses Xilinx's Zynq-7000™-series and can among others run Linux Ubuntu as an operating system on 512 MB of storage and 1 GB of RAM. It provides several different interfaces from SPI to Gigabit Ethernet. Of special interest is the tight integration of the Xilinx Kintex-7 FPGA with an ARM dual-core Cortex™-A9 CPU, which enables a flexible system with parallel processing power and real-time capabilities due to the FPGA.

Mercury+ XU1 The Mercury+ XU1 uses the bigger Xilinx's Zynq UltraScale+™ MPSoC-series, which includes an ARM Cortex™-A53 cores and ARM dual-core Cortex™-R5 as well as a Mali-400MP2 GPU together with a Xilinx UltraScale+™ FPGA. It can have up to 4 GB of RAM and 16 GB of storage and offers more interfaces than the ZX1.

Both devices combine a lot of computing power within $74 \times 54\,\mathrm{cm}^2$ and would even make integration of the FPGA used in the ROE into a single device possible. The Mali GPU is not considered as it is too small for the networks used in this application.

Jetson Nano The Jetson Nano module uses a ARM Cortex™-A57 in combination with a 128-core Maxwell™ GPU by Nvidia. A Linux operating system can be run on 4 GB RAM and different external storage options. The module is $70 \times 45\,\mathrm{cm}^2$ big.

Jetson TX2(i) The Jetson TX2 comes in different versions. The base version combines a Dual-Core Nvidia Denver 2 and an ARM Cortex™-A57 CPUs together with a 256-core Nvidia Pascal™ GPU. It has 8 GB of RAM and offers 32 GB of storage. It has a built-in Wi-Fi module and runs Linux Ubuntu. The TX2i version strips some of the features like the Wi-Fi module while built for industrial applications in drones and embedded systems. It is factory tested for vibrations and shocks. Both modules are about $90 \times 50\,\mathrm{cm}^2$ big.

These modules have a GPU which is interesting for the execution and deployment of the artificial neural networks.

To compare these systems against each other two tests were performed on each system:

- An overall load test, which aims to measure the total power consumption of the module (section 4.1.1)
- A Tensorflow calculation test to measure the event processing time on CPUs and GPUs of the modules (section 4.1.2)

4.1.1 Load Test

The maximum power consumption of each system can be estimated by trying to utilize the built-in CPU and GPU fully. This is valid as the CPU and GPU power consumption is large compared to IO interfaces and dominates the overall system power consumption. To utilize the processors a dummy Tensorflow calculation is used. It is designed to run for five minutes and uses as much computing power as the system can deliver. Where possible CPU and GPU were utilized fully simultaneously. All power measurements have been conducted with the use of the internal power monitor ICs of the respective development kit for each single board computer.

The Jetson modules have different power modes defined by Nvidia, which can be adjusted by the user via the operating system. In these modes CPU cores can be switched on and off and the frequencies of the CPU cores and the GPU can be limited to upper and lower operating limits. These limit how fast the CPU or GPU calculate. An overview over the predefined modes for Nano and TX2(i) modules give Table 4.2 and 4.3.

Table 4.2: Predefined Jetson TX2 and TX2i power modes.

Mode	Name	Used Denver Cores	Denver frequency [GHz]	Used ARM cores	Maximum ARM frequency [GHz]	Maximum GPU frequency [GHz]
0	Max-N	2	2.0	4	2.0	1.30
1	Max-Q	0		4	1.2	0.85
2	Max-P Core-All	2	1.4	4	1.4	1.12
3	Max-P ARM	0		4	2.0	1.12
4	Max-P Denver	1	2.0	1	0.4	1.12

Table 4.3: Predefined Jetson Nano power modes.

Mode	Name	Used ARM cores	Maximum ARM frequency [GHz]	Maximum GPU frequency [GHz]
0	Max-N	4	1.48	0.92
1	5W	2	0.92	0.64

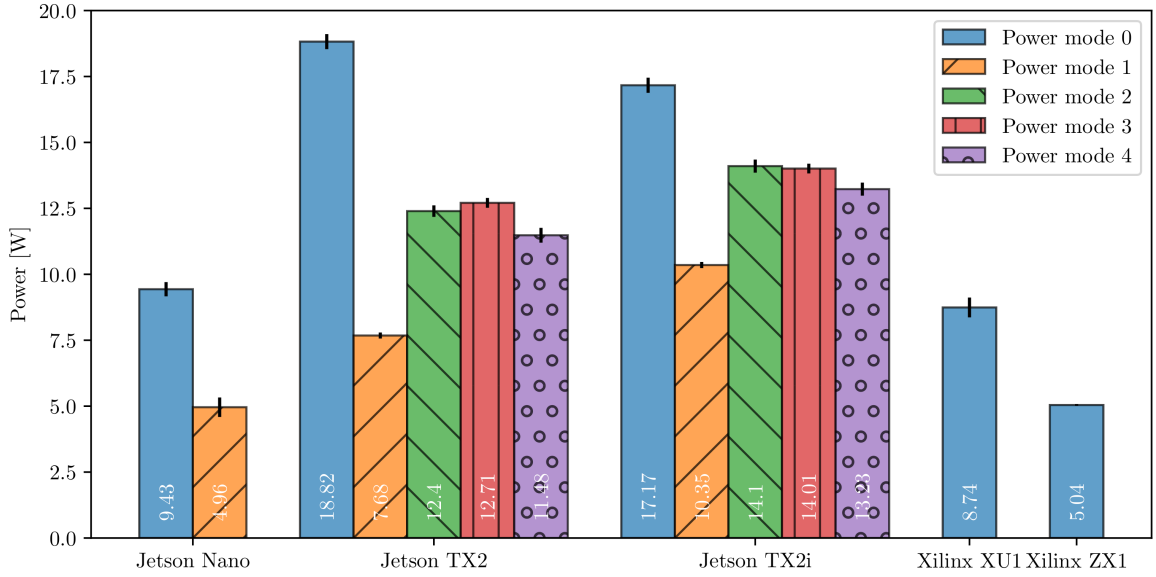

Figure 4.2: Combined GPU and CPU power consumption of tested single board computers: Colour shows power modes where available. Standard deviation from mean values are indicated with black error bars.

In Figure 4.2 the results of the combined CPU and GPU stress test are shown. The load was applied to the CPU and GPU (if available) at the same time. The predefined power modes of the Jetson modules were tested separately. A power drop for decreasing clock frequencies can be seen in comparing the different power modes with each other. This is expected as the processor is not allowed to operate at its full speed. A table with all values and results of separately conducted tests of CPU and GPU can be seen in section A.2.

The Jetson Nano and the Xilinx XU1 need both less then 10 W. The ZX1 module on the other hand only needs 5 W and is comparable with the Jetson Nano in power mode 1. The Jetson TX2 and TX2i modules can consume up to 19 W in power mode 0. In all other power modes the power consumption is under 15 W.

4.1.2 Tensorflow Test

Since the event processing uses artificial neural networks, the performance in terms of the event processing rate is a important factor for the compute unit. To compare the modules against this constraint a test with an event analysis network was conducted. This network is an early unoptimised version of the event processing networks that will be used for the on-orbit operations of the RadMap Telescope [91]. It uses a parallel data input and can work with several events at once, as the final network would. 1, 10, 100 and 1000 events per batch were tested. The network gives a rough estimation of event processing time per event, that can be expected of the individual SoC.

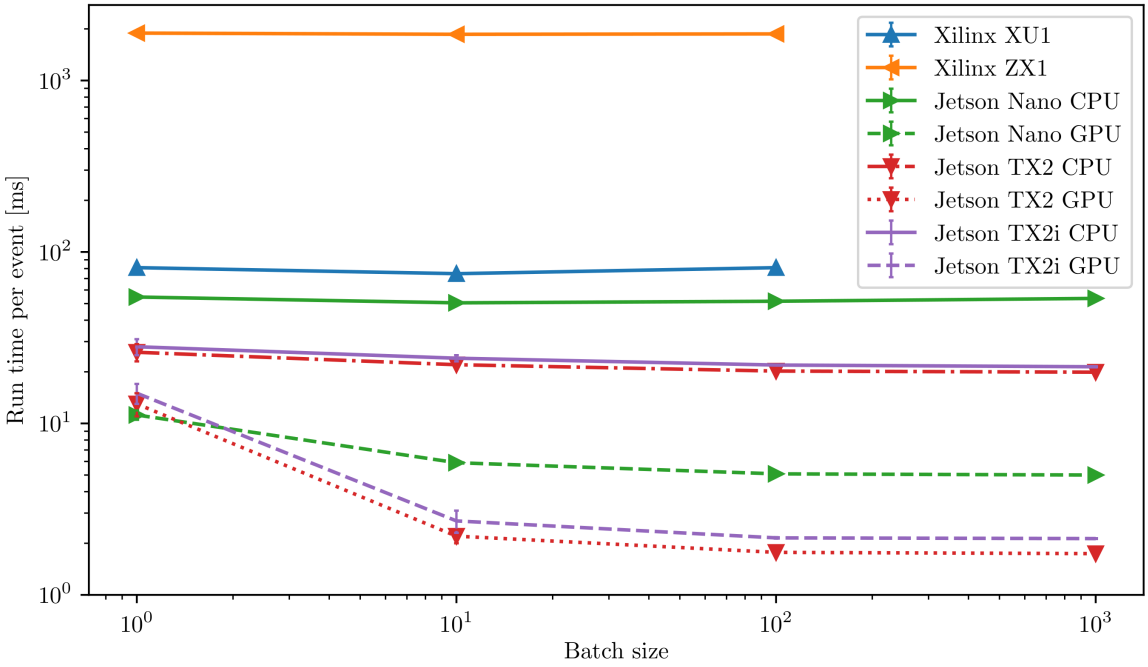

Figure 4.3: Event run time on tested single board computers: Analysis artificial neural network [91] was tested with different batch sizes on CPU and GPU (dashed) of different SoCs. For the Jetson TX2(i) and for the Jetson Nano power modes 3 and 0 are shown respectively.

In Figure 4.3 the event run time versus the used batch size of the network is shown for the individual modules. Modes with Denver cores enabled show similar or worse performance (Table A.3) and are not shown. Power mode 3 was chosen for the Nvidia Jetson TX2(i), as it uses less then 15 W and uses only the GPU and ARM cores. Power mode 0 was selected for the Jetson Nano as it unlocks the full potential of the chip while remaining under 15 W.

Event run times for the network run on the CPU do not depend on batch sizes, as they do not show large changes with increasing batch size. With increasing batch size the run time per event decreases, if the network is run on GPUs. Run time per event can be improve by a factor 2 in case of single event processing and by a factor of 10 in case of large batch sizes when compared with CPU run times. The Nvidia Jetson modules outperform the Xilinx modules. In the case of the ZX1 module the Jetson modules have run times lower by at a factor of 10. The XU1 module run times are comparable to the Jetson Nano run times, if the network is run on the CPU.

The parallel processing of the Nvidia GPUs can be beneficial, aiming for low event processing times near 1 ms to be able to process the events with the maximum predicted event rate of 1 kHz. Thus, the Xilinx modules are excluded in the further selection process for the CCU CPU.

4.1.3 Interface Comparison

To further narrow down the selection, the available interfaces on each module are compared. In Table 4.4 the SoCs of the Nvidia Jetson product family are shown with there respective interfaces.

The TX2 and TX2i modules are very similar and only differ by the build-in Wi-Fi and Bluetooth interface. The Nano does not have CAN (FD) and Wi-Fi. It supports fewer interfaces per type than the TX2 product series.

In comparison the Nvidia Jetson TX2(i) stands out as a very performing and at the same time very configurable processor. On top of the predefined power modes also user modes are possible and will

Table 4.4: Interfaces comparison of the Nvidia Jetson product family single board computers

Interface	TX2	TX2i	Nano
CAN (FD)	2	2	0
I2C	8	8	4
SPI	3	3	2
UART	5	5	3
LAN	1	1	1
PCIe Lanes	4	4	4
USB 2.0	3	3	3
USB 3.0	3	3	1
Wi-Fi/Bluetooth	yes	no	no

allow for even more configurations. It has a fast enough GPU to handle the event processing rates of up to 1 ms and provides a lot of different interfaces to use with the RadMap Telescope systems.

The Jetson TX2i is preferred over the TX2 as it is factory tested for vibrations up to 5 G and shocks up to 140 G for 2 ms. The Wi-Fi interface is not important as an external card is already present in the system. The mPCIe card can also be used with other CCU solutions in future missions and uses better connectors for vibration and shock tolerance than found on the Nvidia modules.

4.2 Architecture

With the main component for the CCU chosen, the system architecture can be defined as shown in Figure 4.4.

The Jetson TX2i collects the data from its connected nodes via the Controller Area Network (CAN) bus [86]. ADCs are used to read out the temperature sensors throughout several systems. They share the I2C [87] interface with the power monitors of the PDU, since most of the sensors will be located near the power converters. The different power domains can the switched on and off by the Jetson via general purpose input output (GPIO) pins to the PDU. In order to control all ASICs of the ROE, SPI and GPIOs are connected to it. Attitude and pressure sensors are also connected via I2C. For a high data rate link between FPGA and Jetson module PCIe [69] is used.

4.3 Nodes and Node Communication

This section explains the following nodes as seen in Figure 4.4 in more detail:

- ROE
- REF 1 & 2, which is one node as REF 1 and 2 share the same microcontroller.
- CRY 1 and 2 are to separate nodes, but will be presented only once as the only difference is their shielding.

4.3.1 CAN FD Bus

To connect the various nodes distributed over the RadMap Telescope, a power saving and wiring efficient solution is required. The main problems arise due to long signal paths and restricted routing space to each node.

Several low level interfaces that are provided by the Jetson compute module could be used:

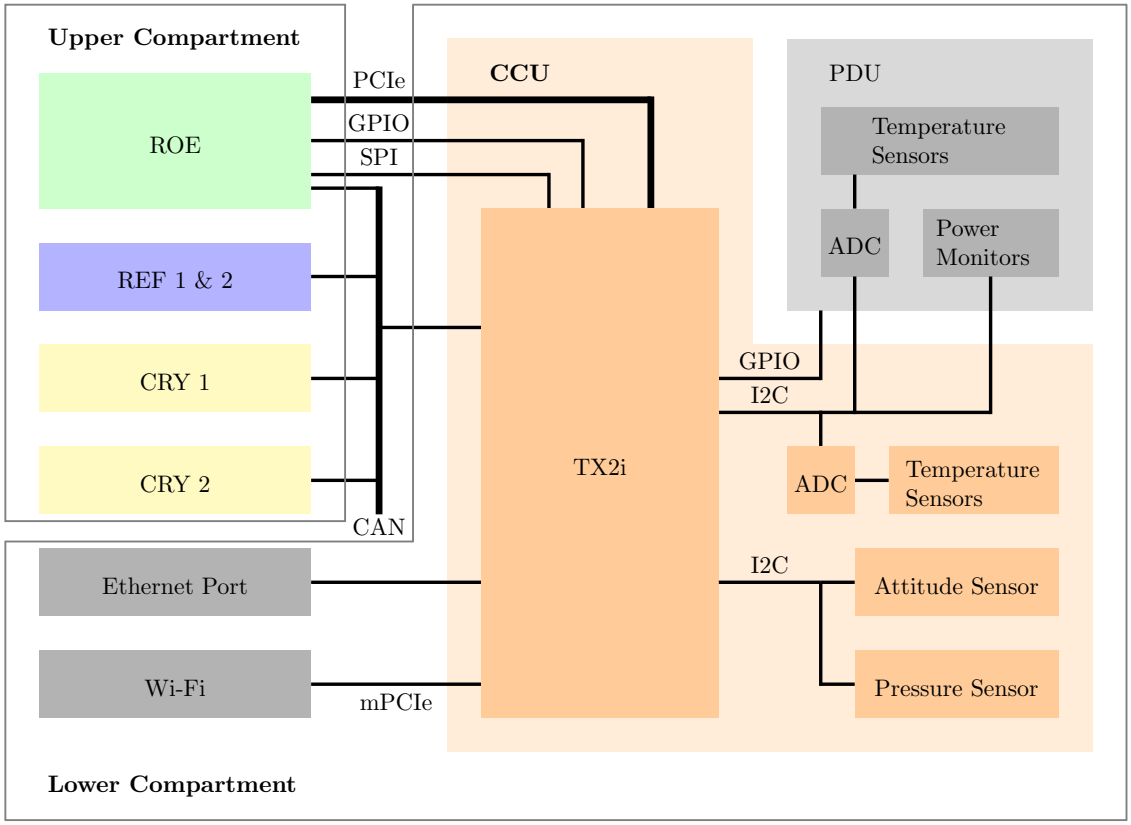

Figure 4.4: CCU system architecture: The Nvidia Jetson TX2i is the compute unit of the CCU. It is connected to several different components via the interfaces specified.

- The Serial Peripheral Interface (SPI) [85] is a synchronous serial communication interface. It uses one clock line and two directional communication lines between two ICs. If multiple ICs share the same data and clock lines, a chip select line for each chip has to be used to indicate to the slave chip that the master chip wants to start a communication. Only one master can be present in the system at a given time.
- Inter-Integrated Circuit (I2C) bus is a synchronous serial communication bus [87]. It uses a bidirectional data line and a clock line. Multiple chips can share the same bus and are addressed by a seven bit long address.
- The Controller Area Network (CAN) [86] and its successor CAN Flexible Data-Rate (CAN FD) [92] are commonly used in the automotive industry. CAN and CAN FD use a differential pair driven at common mode voltages of 0 and 5 V (CAN high and CAN low). Messages on the bus will be rebroadcasted by each member of the bus until the message has been received by its designated recipient. A CAN bus can have multiple chips attached and a variety of bus management architectures can be implemented with this protocol. CAN FD introduced higher data rates up to 5 Mbit s^{-1} [93] and a more flexible protocol with 64 bytes of data in one message.

For the RadMap Telescope SPI is not suitable for the connection of all nodes. It would need a chip select line and two data lanes with long traces from the CCU to each node. More so this star shaped signal structure introduces strong reflections within the data and clock lines, which can degrade the signal heavily over long distances.

I2C would overcome this issue with a common data and clock line. While in theory signals could be used up to 2.25 m of cable length, the power consumption would be increased and signal integrity in case of the RadMap Telescope might be of concern, as signals would have to pass multiple connectors

until they arrive at their destination. As the signal will not be re-emitted by members of the bus, the signal degrades over long distances, resulting in low data rates.

CAN fits into the needs of the RadMap Telescope. Due to the use of a differential pair it can operate over several tens of meters via multiple connectors. A small disadvantage could arise in the need for 5 V at every member on the bus to maintain the differential data line. Since most of the nodes do not operate on this voltage or have peripherals that need it, a power line would have to be added to the differential pair. CAN FD is in principle not needed for the RadMap Telescope, but the more flexible protocol makes the implementation of user headers less complex and is preferred over CAN.

To use CAN, a CAN specific controller and a transceiver is needed. Usually the controller is built into the microcontroller. If this is not the case, an external controller has to be used which is connected via one of the usable interfaces of the IC. A widely used and proven external controller is the MCP2515 [94], which uses SPI to communicate with its host [95]. If a CAN FD interface is needed, the successor MCP2518FD [96] can be used.

A transceiver chip has to be provided externally. In Table 4.5 some of the available solutions are presented.

Table 4.5: CAN FD transceiver comparison

Name	Voltages [V]	Operating Temperature	Radiation Hardened	maximum Power Consumption [mW]
ATA6560 [97]	3.3, 5	−55 °C to 150 °C	no	231
UT64CAN333x [98]	3.3	−65 °C to 150 °C	yes	198
LTC2875 [99]	3.3	−55 °C to 125 °C	no	198

The ATA6560 by Microchip offers a wide range of operating temperatures and a standby mode to save power during idle. A radiation hardened transceiver (UT64CAN333x) by Cobham with an even wider range of operating conditions is also interesting for later deep space missions. The LTC2875 and UT64CAN333x are unique as they do not need 5 V. Instead of using 5 V they use only 2.5 V for CAN high. All presented ICs share a similar footprint. As the LTC2875 saves the need of a 5 V power rail and can be upgraded for later missions to be radiation hardened, it is used throughout the instrument.

4.3.2 Node Microcontroller

For a fast development process and a reduction of manufacturing complexity each node uses the same microcontroller. Three candidates by Microchip have been chosen for this purpose which are compared in Table 4.6.

All presented microcontrollers are based on an 8-bit architecture and offer timers and simple arithmetic functionality. A built-in ADC can also be used to read analog voltages. Each controller has to be programmed to its specific needs and does not run an operating system. It does not have persistent storage accessible by the user and runs only the programmed code.

ATMega64M1s key aspects are its high temperature tolerance while offering a CAN interface which is unusual in this product range. ATMega128 and ATMegaS128 share all features but the later has been made radiation tolerant by the manufacturer. They are pin compatible, which means one can swap one for the other without redesigning the PCB. Also, the software written for one device can be used without changes by the other.

The ATMega128 has been chosen for its upgradability to a radiation tolerant version as well as its interfaces. Together with the mentioned MCP2518FD and LTC2875 chips it is able to communicate with the Jetson TX2i via CAN FD. This combination will be used for all four nodes (ROE, REF 1 & 2, CRY 1 and 2) on the CAN bus.

Table 4.6: Microcontroller comparison for use in nodes

Name	Operating Temperature	Radiation Tolerant	Memory Size [kB]	Interfaces
ATMega64M1 [100]	−40 °C to 150 °C	no	64	1x UART 1x SPI 1x CAN
ATMega128 [101]	−40 °C to 85 °C	no	128	2x UART 1x SPI 1x I2C
ATMegaS128 [102]	−55 °C to 125 °C	yes	128	2x UART 1x SPI 1x I2C

4.3.3 ROE and ROE base

To be able to control ASICs and SiPMs of the ROE, the architecture presented in Figure 4.5 is used. This enables the RadMap Telescope to optimise the detector efficiency while on orbit.

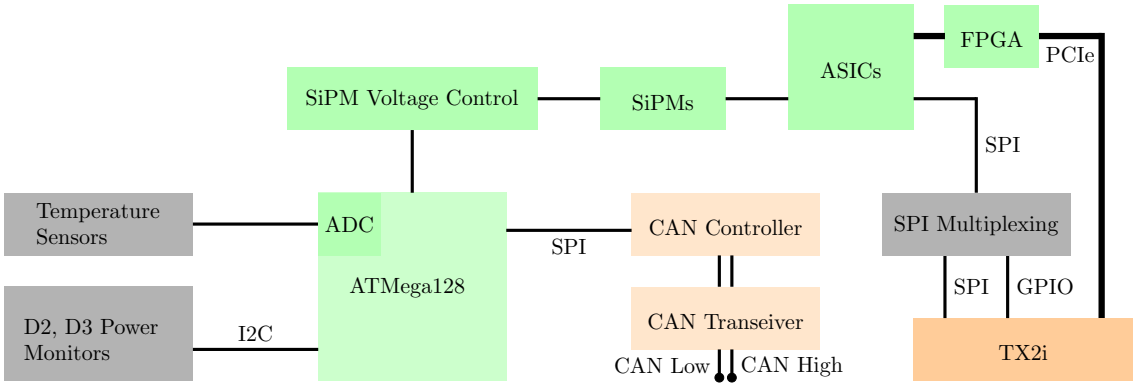

Figure 4.5: Schematic overview of the ROE base Node Architecture.

As explained in the previous sections, an ATMega128 microcontroller together with an external CAN controller and transceiver is used. With its built-in ADC it can measure voltage outputs by temperature sensors in the upper compartment. This includes temperatures of the individual cooling channels as well as the different ROE boards of the ADU. Additionally power monitors for domains D2 and D3 can be controlled via I2C by the microcontroller.

SiPM output voltages are digitised by the IDE3380 ASIC. The Artix-7 FPGA fetches the digitised output of the ASIC. The FPGA sends an interrupt signal to indicate that new data is available. After that the TX2i can collect the data via PCIe.

The SiPM operating voltage settings for temperature compensation are adjustable by the ATMega128. Together with the temperature measurement this enables temperature compensation of the measurement process. In order to control the settings of the ASICs, a SPI interface of the TX2i is used in combination with a SPI multiplexing circuit[1], as the SPI is needed by the 64 individual chips.

SPI Multiplexing Every ASIC can be controlled via SPI. As multiple members share the same bus, since the ATMega128 nor the TX2i have enough interfaces to address each chip individually, the SPI clock, data and chip select lines have to be multiplexed. The data and clock lines will be

[1] Such a circuit has one input and can distribute this input to multiple outputs. This is called multiplexing.

multiplexed 16 times for each ROE board of the ADU. The chip select line has to be multiplexed 64 times to address each chip.

Low power and SPI frequency compatible switches are needed. Several different multiplexer of this type are compared in Table 4.7.

Table 4.7: Comparison of different multiplexer for SPI

Name	Output Channels	Maximum Operating Temperature [°C]	Typical Power Consumption at 3.3 V [nW]
ADG704 [103]	4	85	3
MAX4734 [104]	4	85	13
ADG804 [105]	4	125	10
ADG1606 [106]	16	125	3
ADG706 [107]	16	80	3

All presented devices use between 3 nW to 10 nW. They differ in their maximum operating temperature and output channel number. The ADG804 and ADG1606 in series were chosen as they have the highest operating temperature and in combination can deliver 64 channels with low amount of switching ICs required.

PICe The most critical data interface is between the FPGA and the Jetson compute module. The interface has to be capable of transmitting at least 12.3 Mbit s^{-1} of data.

One of the interfaces of the TX2i, which fits this purpose is the Peripheral Component Interconnect Express (PCIe) [84]. Its specifications state the following key features:

- Support for multiple platform interconnect usages with chip-to-chip and board-to-board connections via connectors or cabling.
- A link may aggregate multiple lanes. A lane is defined as one receiving and one transmitting differential signal pair. Up to 16 lanes can be used in parallel.

In the case of the RadMap Telescope a four lane PCIe generation 2 link will be used. A overview of the PCIe generation capabilities is presented in more detail in section A.1. A four lane generation 2 link operating at a 5 GT s^{-1} transfer rate represents an aggregate bandwidth of 2 GB s^{-1} in each direction. With a need of 1.54 MB s^{-1} bandwidth by the ROE, this interface is more than capable of delivering the required data rate.

4.3.4 REF 1 & 2

As the two reference dosimeters will be placed next to each other only one microcontroller is used. Thus, this acts as one node on the CAN bus. The architecture of this node is presented in Figure 4.6.

The same microcontroller and CAN interface combination is used as described above. The UART interface of the ATMega128 is used to communicate with the DLR M-42 dosimeter. The REF 2 dosimeter data is also fetched and stored by the microcontroller. As the exact details of this dosimeter are not yet known, it may use the internal ADC of the microcontroller or an external one to digitise the output voltages of the dosimeter.

4.3.5 CRY 1 & 2

Each CRY dosimeter has its own microcontroller. They share the same architecture seen in Figure 4.7 as the only difference is the shielding material around the scintillating crystal.

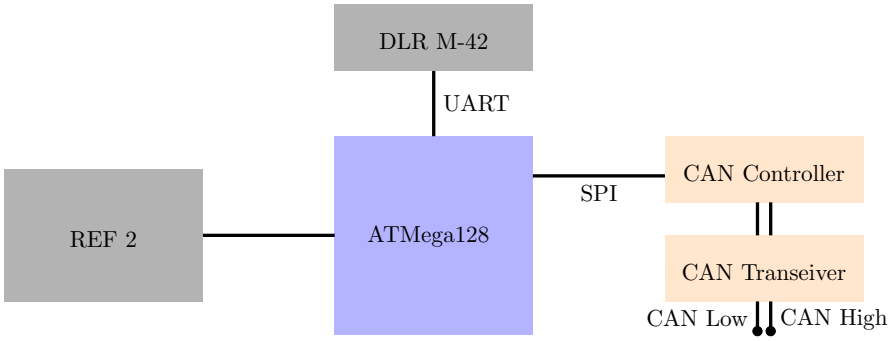

Figure 4.6: Schematic overview of the REF 1 & 2 node architecture.

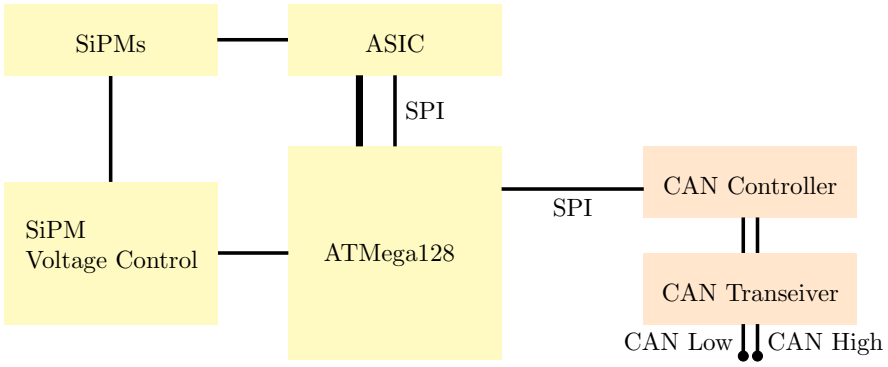

Figure 4.7: Schematic overview of the CRY (1 & 2) node architecture.

As the same SiPMs and ASICs are used for the measurement, the readout process is the same as in the ADU. Instead of using a FPGA as trigger the ATMega128 will collect the digital data. It also controls the SiPM operating voltages as well as the ASIC logic. The SPI interface used for the CAN interface has to be shared with the ASIC. The microcontroller will also calculate the accumulated dose.

4.4 Sensors

Sensors for temperature, power monitoring and environmental conditions like pressure and attitude changes are used within the RadMap Telescope.

4.4.1 Power Monitoring

For power rail monitoring a sensor with at least the capability for measuring the voltage and current is required. A small resistor, connected in series with the load to be measured, is used for this purpose. The voltage across this so-called shunt resistor is proportional to the current used by the load. A current sensor measures the amplified voltage across a well known resistor. The sense resistor R_{sens} can be placed in two different locations (high and low side) as seen in Figure 4.8.

In the case of the RadMap Telescope a high side application is preferred as low side sensing would require all power lines routed back to the PDU as the ground connection is established after the shunt resistor. The highest voltage that has to be measured is the 28 V input provided by the ISS. The current monitor should also be able to measure at least 1.08 A as this is the maximum current the

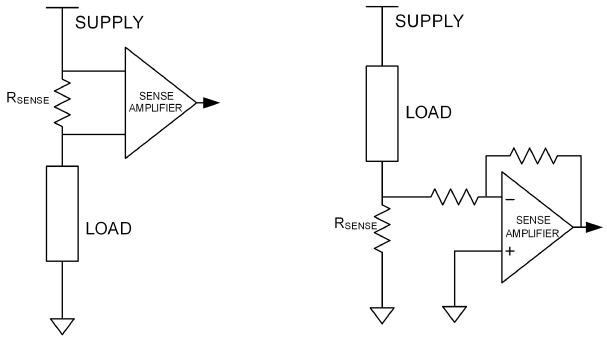

Figure 4.8: Schematic comparison of high (left) and low side (right) current sensing techniques [108].

instrument is allowed to take. A comparison of different power monitoring devices can be found in Table 4.8.

Table 4.8: Comparison of different power monitors.

Name	R_{sens} built in	Maximum Operating Temperature [°C]	Typical Power Consumption at 3.3 V [mW]
INA233 [109]	no	125	1.32
INA226-Q1 [110]	no	125	1.39
INA260 [111]	yes	125	1.39

All presented devices can measure voltages from 0 V to 36 V and are capable of high and low side application. Additionally to voltage and current they also calculate the resulting power consumption. The INA226-Q1 is built for automotive applications. Most notably the INA260 has the advantage of a built-in shunt resistor and therefore decreases the design complexity of the PCB. It will be used throughout all power domains to measure their power rails.

4.4.2 Attitude Changes

To measure changes in the orientation and placement of the instrument, accelerometers or attitude sensors can be used. A comparison of some applicable devices is given in Table 4.9.

Table 4.9: Comparison of accelerometers and attitude sensors

Name	Axis	Maximum Operating Temperature [°C]	Typical Power Consumption at 3.3 V [mW]	Accelerometer	Gyroscope
BMX055 [112]	3	85	17.5	yes	yes
BNO055 [113]	3	85	9.9	yes	yes
ADXL357 [114]	3	125	0.66	yes	no

The major difference between the presented devices is the built in gyroscope of the BMX055 and BNO055 compared to the ADXL357. While they take a lot more power than the ADXL357, the other sensors can also detect changes in the orientation without complicated calculations. Furthermore, the BNO055 uses its sensors to calculate the linear acceleration as well as the precise information of its orientation in space with so called sensor fusion, where multiple sensor values are combined to one quantity. As a prior project already did use the BNO055 successfully, it has been chosen for the RadMap Telescope, despite its higher power consumption compared to the ADXL357.

4.4.3 Pressure

The BMP280 [115] and BME680 [116] pressure sensors were used in prior projects successfully and are interesting for the instrument. The BME680 can also measure humidity and air quality. Since their power consumption is similar, the BME680 was chosen to get also the humidity information, which can be used in thermal calculations for a more precise result.

4.4.4 Temperature

The RadMap Telescope has many components and locations where temperature has to be measured. As a digital solution for every sensor would lead to a lot of interfaces and programming needed, a thermistor in combination with an ADC was chosen. A thermistor is a resistor, whose resistance is highly dependent to its temperature. As the resistance changes, the voltage drop over the thermistor changes. This voltage can be measured via an ADC.

The following combination of thermistor and ADC has been chosen. The MC9700(A) [117] by Microchip covers a large temperature range of $-40\,°C$ to $150\,°C$ and maintains a precision throughout this range of $1\,°C$ to $2\,°C$. It comes in multiple physical variants that can be applied in very versatile ways throughout the instrument.

The AD7091R-5 [118] is used as an ADC. It provides four channels with 12-bit resolution while only needing about $350\,\mu W$. It can also use multiplexers with the built-in GPIO functionalities, which makes it possible to gather temperature data of several different thermistors without the need of GPIO pins of the Jetson module or ATMega128.

Chapter 5

Software

The presented hardware has to be controlled via software running on the Jetson compute module and the individual nodes. Also, the software is confined by the requirements presented in chapter 3.

The Jetson TX2i is the master to all nodes on the CAN bus (ROE, REF 1 & 2, CRY 1 and 2) and is running a version of the Linux Ubuntu operating system provided by Nvidia. Science and telemetry data can be requested by a fixed set of commands for each node. With these commands the CCU is also able to configure the sensors and other devices of the node. The microcontrollers of the CAN nodes act as an extension to the CCU rather than distributing data on their own. Data processing, storing and redistribution to the ISS network is done by the compute module. Figure 5.1 gives an overview of the software architecture of the RadMap Telescope.

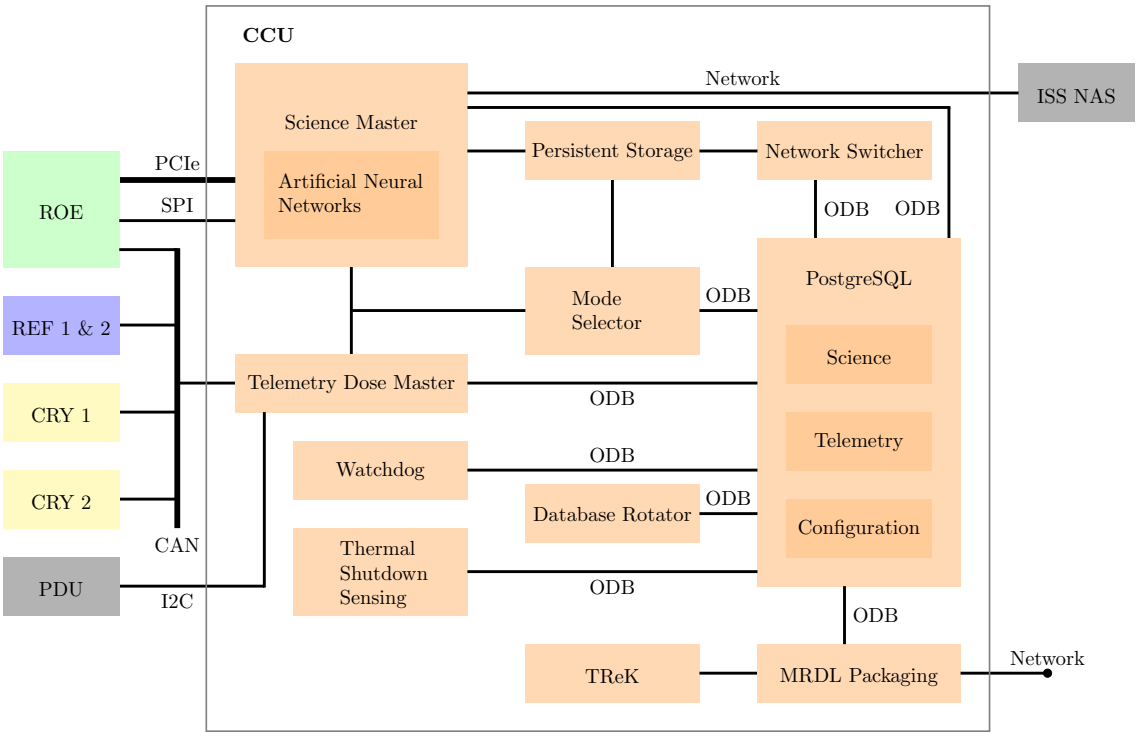

Figure 5.1: Schematic overview of the CCU software architecture.

Databases managed by the PostgreSQL [119] database management software are used for the CCU to store science, telemetry and configuration values. The programs utilize the ODB object relational

mapping (ORM) library [120] to interact with PostgreSQL. It is used by all presented software to interface three different databases: Science, Telemetry and Configuration.

At system boot the programs will be started by the CCU in the following order:

1. Watchdog
2. Thermal Shutdown Sensing
3. Network Switcher
4. Mode Selector

The Watchdog program checks, if the system has been reset after the processor was unresponsive and saves this information to the Telemetry database. The Thermal Shutdown Sensing program uses GPIOs of the Jetson TX2i to measure, if a thermal shutdown has occurred since the last system start. It stores the information in the Telemetry database. The network switcher program reads a file, that has the information stored about which network interface has to be used by the instrument, and configures network settings of the operating system. It is also used to check, if the chosen network interface can establish a connection to the ISS and may switch to the other interface, if the connection is not working.

The Mode Selector program starts the Science Master and Telemetry Dose Master program. It selects the operation mode according to stored information in a file in the persistent memory of the Jetson compute module. It can alter the mode, if a watchdog event or thermal shutdown has occurred by checking for it in the Telemetry database.

The Telemetry Dose Master fetches dose and telemetry data by the nodes on the CAN bus and from the attached I2C devices on all I2C buses (Power monitors, ADCs, pressure and attitude sensors). The data is stored in the Science and Telemetry databases accordingly. It can also configure the CAN nodes and I2C devices by values stored in the Configuration database. The Science Master program configures the ROE and collects the science data by it. The data is then saved to the ISS NAS or the persistent storage on the Jetson TX2i. It initiates the analysis with artificial neural networks, which will store their results in the Science database.

The Database Rotator deletes database entries which are older as a configurable time interval and that were sent to ground via the network. To pack UDP packages to be sent via the network the MRDL packaging program fetches required data from the databases and uses the NASAs (TReK) library [81] to build the network packages of science, telemetry and dose data.

All programs of the CCU can store status messages about their execution state in the Telemetry database. This is primarily useful for testing and issue tracking during development and also if a problem occurs while in operation aboard the ISS.

5.1 Nodes

All nodes of the CAN bus use the same microcontroller. They share large parts of their code and run the same basic program loop presented in this section. The software for all microcontrollers (ROE, REF 1 & 2, CRY 1 and 2) is written in C, as the AVR Toolchain [121] provided by Microchip uses it as its main programming language. Additionally to the functions of the AVR toolchain, two open source libraries for routines [122] and interfaces [123] are used.

An instrument specific header has been added to the CAN FD protocol. This header unifies how data is sent to the CCU and has extended features for requesting telemetry data of the microcontroller as well as configuring the devices present on the node. All commands that can be executed via CAN FD messages are predefined.

5.1.1 CAN FD Protocol

The commands sent to request data from a CAN node or configure attached devices use CAN FD frames. The CAN FD frame extends the available data field of one message to 64 bytes compared to only eight bytes for a CAN frame as shown in Figure 5.2 [86, 92].

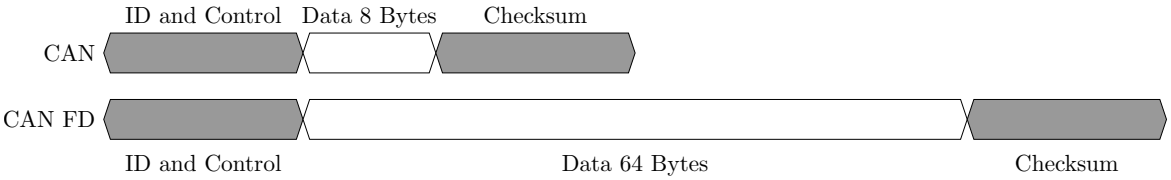

Figure 5.2: CAN and CAN FD frame types in comparison.

The standard CAN frame consists of a header section where the ID of the addressed node and protocol specific settings are stored. This is followed by eight general purpose data bytes and a message-specific checksum, which leads to 16 bytes in total. The checksum is used by the CAN controller to check if the full message has been received correctly and no bit flips have occurred during the transmission. The transmission is automatically retried by the controller, if the message is corrupted. The standard CAN was updated to CAN FD in 2012 to enable a larger general purpose data byte section of up to 64 byte. ID, control and checksum fields have the same purpose, but were slightly altered to support the longer frames (72 bytes total).

The RadMap Telescope uses the CAN FD frame since messages with over eight byte data content are needed. Within the 64 available data bytes the first four bytes are used to implement an instrument-specific protocol shown in Figure 5.3.

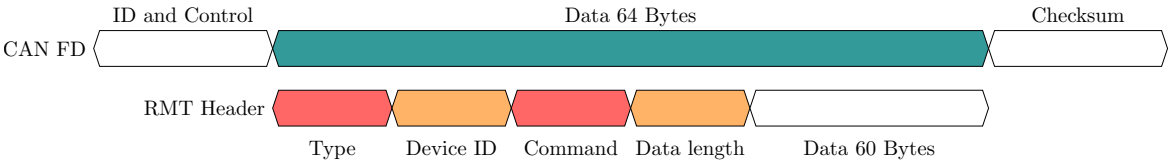

Figure 5.3: The RadMap Telescope uses four bytes to indicate message type, device address on the node, command and data length of following data.

These data bytes are one byte each and contain the following information:

- Message type: This field can have four values for four different purposes.
  - **valueGet** The CCU wants to get a value of one of the attached devices of the node or telemetry data of the microcontroller.
  - **valueGetAck** The CCU has requested a value and the information is sent back by the microcontroller. The data is attached after byte 4.
  - **valueSet** The CCU wants to set a configuration in the microcontroller or one of the attached devices. The value to set the device to is attached after byte 4.
  - **valueSetAck** The CCU has sent a configuration value and the microcontroller has configured the device accordingly.
- Device identification: It stores one of the predefined addresses for each device (microcontroller or sensor) to indicate for which device the message is for.

- Command: Here a set of predefined commands specific to the device is saved to indicate to the device that a measurement value has to be collected or a function has to be executed.
- Data length: This field indicates the length of the following data bytes up to a value of 60.

All CAN bus nodes and all devices of these (including the microcontroller) have a unique ID (Device ID) to address them. All commands that can be used with a device are predefined.

The ID field of the regular CAN FD header indicates the node the message has to be sent to. To illustrate the functionality of this header a data request and a configuration example are given here.

Configuration Example The CCU wants to alter the operating mode of the D2 power domain 3.3 V power monitor present on the I2C bus of the ROE node. The command sequence is shown in Figure 5.4.

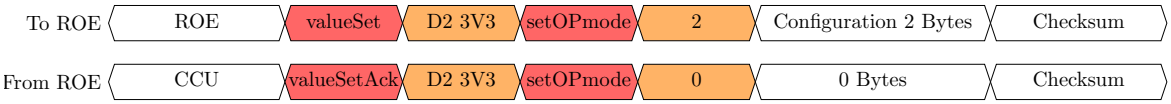

Figure 5.4: Example for a CCU commanding sequence for one of the power monitors of the ROE.

First the CCU sends a message to the ROE stating that it wants to configure the D2 3V3 device and the command to change the operating mode to the configuration given in the attached data bytes. The ROE responds after the configuration has been executed with an acknowledge message with the information of the command used.

Data Request Example If the CCU wants to request data from the D2 3V3 power monitor, it can use the commanding sequence shown in Figure 5.5.

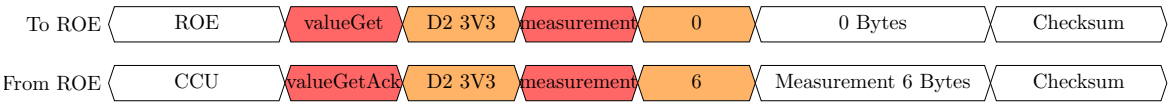

Figure 5.5: Example for a CCU data request sequence for one of the power monitors of the ROE.

The CCU requests information about the measurement of the D2 3V3 device from the ROE. The ROE sends back the requested information after the measurement data has been fetched using the I2C bus. It attaches the data after byte 4.

5.1.2 Commands

Some commands a shared by all nodes and can give telemetry information about the node. The commands as seen in Table 5.1 can be issued by the CCU to every node.

Since all of the nodes use the ATMega128 microcontroller nearly all commands shown return specific register values of the controller, which indicate the current status of the device. Additional information about the status of the CAN controller can be requested. These include the amount of used internal memory of the controller as well as its current settings. The node can also report the amount of devices it has detected for each of its interfaces. Internal timers of the node are started when power is applied to act as a counter. These indicate the time the node has been active. This clock can be

Table 5.1: Common commands that can be issued via CAN bus to get telemetry information of the node.

Name	ID [Hex]	Description	Returned data bytes
powerManagment	1	Returns the power managment register. This contains power state information of the ATMega.	1
resetFlags	2	Returns the reset flag register. It contains information about the reset type that has occurred on the system.	1
intFlags	3	Returns the interrupt flag register. This indicates the interrupt state of each hardware interrupt pin.	1
ADC	4	Returns the ADC config and status register.	1
CAN	5	Returns the status of the CAN controller. Bus diagnostics and error counts are provided.	11
SPI	6	Returns the SPI status register.	1
UART0	7	Returns the registers for UART 0 status and configuration.	3
UART1	8	Returns the registers for UART 1 status and configuration.	3
TWI	9	Returns I2C status register.	1
externalDevices	10	Returns information about the detected connected external devices.	8
CLK	11	Returns the internal clock provided by the synchronous timer. The clock resets upon device reset.	7
CANTEST	99	It returns a full 64 byte long test CAN FD message.	64

returned to the CCU. For testing purposes the CCU can also request a 64 byte CAN FD frame by the node.

All of these commands are mainly used to check the overall health of the node or in case debugging is required, if an error on one of the nodes or their components has occurred.

5.1.3 Protocol Adaptation

This set of commands and the protocol presented are specific for the RadMap Telescope nodes but are not depending on the CAN FD interface. If future missions require the use of a different bus interface (e.g. I2C), the protocol can be adapted.

In case of I2C the adaption can be done without large changes of the protocol. The address of each device has to be transmitted first followed by the command to be executed. As I2C works already with a master slave model the message type is not needed. One may need to fuse the device ID field and the command field to be used as one command after the node ID has been sent. The data length byte is also not needed as the I2C protocol has such a functionality already built-in.

Similar steps to adapt this protocol may be needed for the use with CAN (8 byte data frame) or SPI.

5.1.4 Program Sequence

The ATMega128 microcontroller execute only one predefined program, that cannot be altered during run time. After all interfaces needed for its operation such as I2C are configured, the main program loop presented here is executed. All nodes share the same execution loop for the main program shown

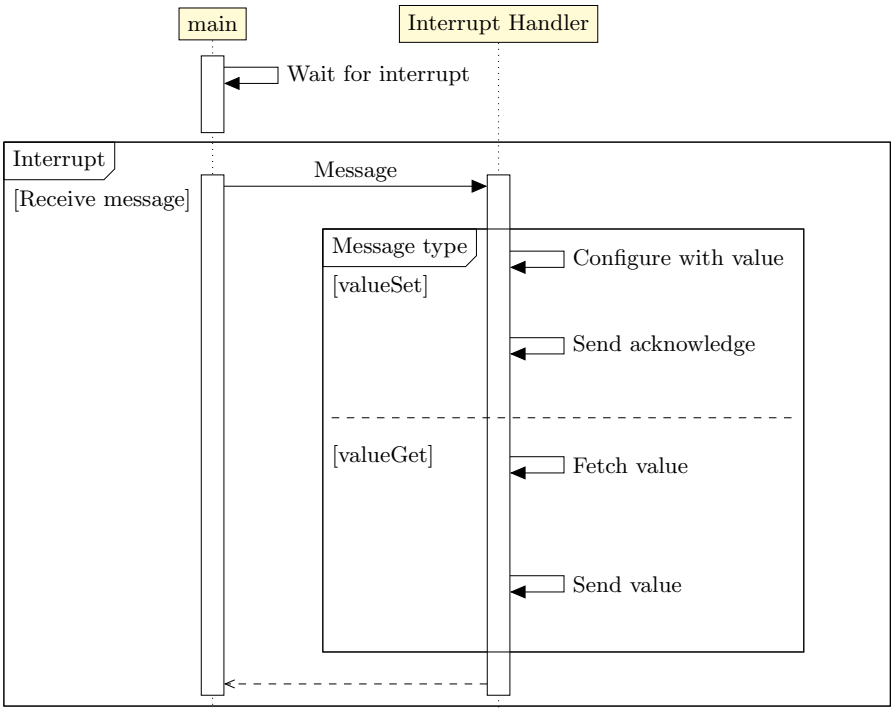

Figure 5.6: Schematic view of the main programming loop executed on all nodes.

in Figure 5.6. This part of the code of the microcontroller is running all the time in a loop and executes all other programs.

The main program loop timeline (left) and the interrupt handler subprogram (right) is shown. The interrupt handler routine has all device and interface specific functions and can process the incoming CAN messages. First the main program waits until it gets interrupted by an incoming message to the node. It passes the message to the interrupt handler which conducts the requested action. Depending on the message type as seen in the prior sections, the handler configures the device attached to the microcontroller or fetches the requested value for the CCU. In both cases a message is returned to the CCU according to the protocol stated above. After the message has been processed the program jumps back to the beginning of the main loop and waits to receive another interrupt by receiving a CAN message.

5.2 CCU

One of the main programming language used in the Ubuntu operating system of the CCU is C++. Also a lot of already existing code for sensors and interfaces is written in C++ and C, which can be integrated into C++. As a result all software used on the CCU is written in C++.

C++ is a general-purpose programming language created by Bjarne Stroustrup. The International Organization for Standardization (ISO) standard version ISO/IEC 14882:2011 is used [124]. The main purpose of C++ programming is to add object orientation to the C programming language in form of classes. A class is used to specify the form of an object and it combines data representation and methods for manipulating that data into one package. The data and functions within a class are called members of the class.

The system has to be able to gather dose rate information without a human interaction of the system after prior installation to the designated location. For this, the system boots automatically, if power is applied, and on startup the Ubuntu operating system uses the *systemd* [125] services to run and

configure itself. *systemd* is a software suite that provides an array of system components for Linux operating systems including program startup, interface and file management as well as event logging and network connection management.

The RadMap Telescope software is started as a service within *systemd*. The starting sequence of the CCU is shown in Figure 5.7.

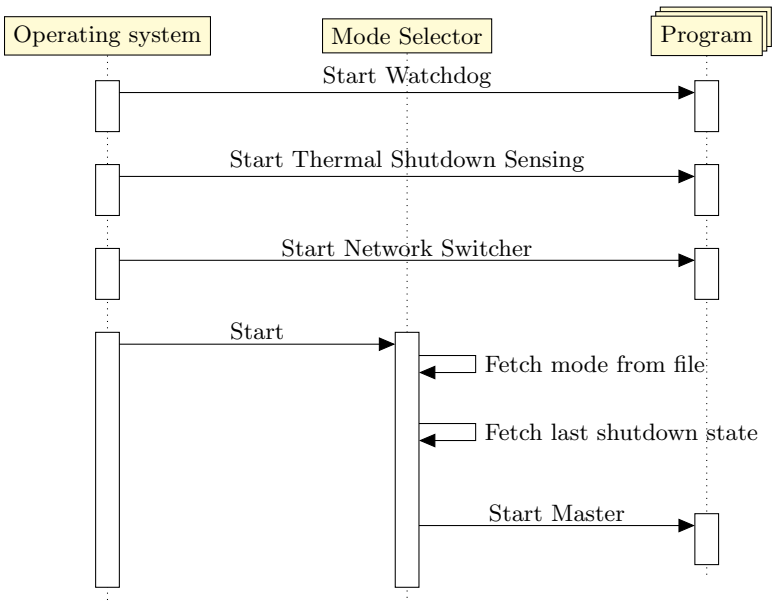

Figure 5.7: Schematic view of the CCU boot sequence.

At the top the operating system, Mode Selector program and one additional timeline, that acts as a dummy to indicate the individual started program, are shown. During boot the CCU will start the Watchdog program. It checks if a watchdog reset of the operating system or any hardware on the Jetson compute module has caused a system reset and saves this information in the Telemetry database. The Thermal Shutdown Sensing program is started and checks if the CCU has restarted after a thermally caused shutdown and stores this information in the Telemetry database.

The Mode Selector program is started and uses the information provided by a configuration file and the prior saved information of the occurred shutdowns to start the Telemetry Dose Master and Science Master programs accordingly. The configuration file can be altered by the user and has to be set during the initial commissioning phase.

5.2.1 PostgreSQL Databases and Interfaces

All hardware interfaces can be controlled via dedicated software libraries either provided by the operating system or newly written. SPI, I2C and the GPIOs are implemented as separate classes and are using the standard Linux libraries. The CAN interface uses SocketCAN, which is a set of open source CAN drivers and enables the user to configure the CAN bus with *ifconfig*. A system administration utility program for network interface configuration.

To store all configuration and measurement data a database[1] in combination with the database management system PostgreSQL [119] was chosen as it makes organising and accessing data entries easy. The stored data is organised within tables automatically and access management and table configuration is handled by PostgreSQL.

[1] A simple version of a database is a combination of several tables with multiple entries each. More complex versions can have interconnected table entries and other more complex data structures.

Three databases with multiple tables each are used for the RadMap Telescope:

- **Science**: This database has tables for calculated dose rates, particle energy and impact angle as well as other information provided by the neural networks to analyse the ADU data. Dosimetry data by the two reference dosimeter and crystal dosimeters is also stored here.
- **Telemetry**: Temperature, power rail, pressure and attitude measurement data is stored in the database as well as basic system statistics of the operating system such as used RAM and processor utilisation.
- **Configuration**: Configuration data for all nodes and attached sensors and devices of the RadMap Telescope is saved here. The entries can only be altered manually by the user or by incoming configuration messages from an operations team on ground, that have been sent to the ISS.

To establish an interconnection and easy access to the database and its entries throughout the C++ code, ODB object relational mapping (ORM) is used [120]. It allows to save C++ objects such as class members to database entries without having to deal with tables, columns or mapping code. ODB uses classes to relate the database entries to a C++ object. Members of these classes can automatically be written and read to and from database entries. Classes and functions to interact with the databases are collected in a separate library.

5.2.2 Database Rotator and ADU Data

The data stored in the Science and Telemetry databases can be deleted automatically to keep the database organized. The Database Rotator program deletes data entries that have been sent to ground and are older than a user configurable time interval. It is started via *cron* (time-based program scheduler in Linux) every two hours. For the demonstrator mission this program is not mandatory as 32 GB of persistent storage of the TX2i is big enough to hold all incoming data for at least one week and regular maintenance and operating activities are planned. For later deep-space missions such a program is important as the built-in storage might not be big enough to store data long and a full storage would lead to data loss and a slower working CCU.

Raw ADU data, which is saved to the internal persistent storage in case the artificial neural networks can not analyse the incoming data properly and in the commissioning phase, has to be deleted manually. The data can also be stored to the NAS on the space station.

5.2.3 Watchdog and Thermal Shutdown Sensing

The Thermal Shutdown Sensing program uses GPIO pins of the Jetson TX2i to sense, if the instrument has been shut down due to too high temperature that could harm the astronaut. The following events can occur:

- If one side of the cooling channels in the upper compartment for the ROE of the ADU is getting over 45 °C, the corresponding ADU site will be turned off.
- If two or more ADU cooling channels overheat, power to all power domains apart from D0 will be cut.
- If the main cooling channel in the lower compartment for CCU and ROE base is overheating with 45 °C or more, the instrument turns of all power domains but D0.

This functionality is implemented with an analog circuit as this can easily be tested for reliability in the laboratory and does not need extensive software testing. When a shutdown event for all subsystems of the RadMap Telescope has occurred the system will wait turned off for 10 min to cool down with

the airflow provided by the internal air distribution system of the spacecraft. The circuit will store the information that such a shutdown has happened and the Thermal Shutdown Sensing program will read the information via GPIO pins of the Jetson TX2i after the system has restarted. The program will store the information in the Telemetry database.

The program also checks every minute, if any of the ADU side has shut down. This information can be used by the Science Master program to adjust or stop the measurement accordingly.

The Watchdog program checks the system start-up event log to detect a watchdog reset of the Jetson TX2i module, as the information of this event is stored automatically by the operating system [126]. This will also cause the system to enable ccuOnly operating mode to find the error without damaging other system components. The program is only started once at system start.

5.2.4 Mode Selector and Operating Modes

The RadMap Telescope uses four different operating modes which can be used for debugging and power saving. They are also used in case of a thermal or watchdog induced shutdown.

The following modes are available:

- **ccuOnly**: The CCU is on, but all other nodes and detectors are disabled. This mode will be activated, if a thermal or watchdog event has shut down the system. In this mode only values by sensors on the main CCU PCB and telemetry data of the TX2i module are stored in the database and linked down to earth. Network interfaces are all active and remote access to the system is possible.
- **telemetry**: This mode provides only telemetry of the RadMap Telescope. All detectors are off. Additionally to the ccuOnly mode functions also temperature and power rail information are fetched from the ROE node and PDU.
- **dose**: In addition to telemetry mode, dose rates are collected from CRY 1, 2 and REF 1 & 2. The ADU is off.
- **science**: On top of the functions of dose mode, the ADU data is fetched and analysed by the artificial neural networks or stored.

As seen in Table 2.1 also the power domains will the switched on or off according to the selected operating mode to save power of the unused devices. Each mode uses also a different user defined power mode configuration of the Jetson TX2i to save power of the overall system as shown in Table 5.2.

Table 5.2: CPU and GPU frequencies of the CCU in different operating modes of the RadMap Telescope.

Power Mode	ARM cores active	Maximum ARM core frequency [GHz]	Maximum GPU frequency [GHz]
ccuOnly	1	0.35	0.11
telemetry	1	0.80	0.11
dose	2	0.80	0.11
science	4	2.0	1.3

In all modes the Denver cores are turned off. The CPU and GPU maximum clock speeds and the active ARM cores vary depending on the operating mode. These settings may be subject of change during the mission to optimize the CPU and GPU performance as well as the power consumption in each mode.

If used in sequence the modes provide a controlled system start. They can be used to slowly commission the system during initial setup or if power has to be saved. They may additionally be useful for future

missions as the dose mode can be used to detect a rise in the activity of the radiation field and trigger the activation of science mode to analyse the cause. This would save power during long missions as the ADU, which is the main power consumer apart from the CCU, is not powered all the time.

The modes are selected on system startup by the Mode Selector program. It is only started at system starts and executed once. Figure 5.8 shows a schematic overview of the decision sequence of the program.

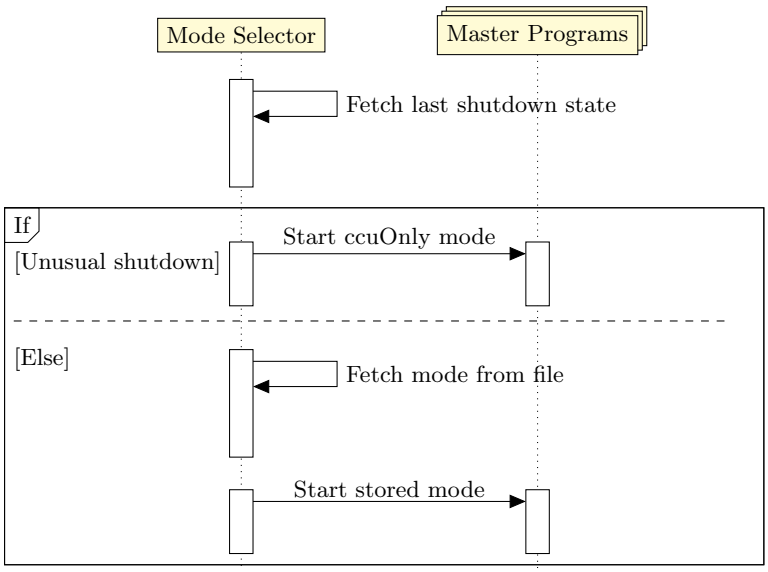

Figure 5.8: Schematic view of the RadMap Telescope mode selection sequence.

The Mode Selector timeline in combination with the dummy master program timeline is shown. At program start the cause of the last system shutdown is fetched from the Telemetry database. If a thermal or watchdog event has shut down the instrument, the system is started in the ccuOnly mode.

If no unusual shutdown has occurred, a file is read, where the user can store the operating mode. A file-based approach has been chosen as it does not require the prior start of PostgreSQL or ODB, as these may not work or get started properly after an unexpected shutdown. The configuration file can be altered by the user and has to be set during the initial commissioning phase. The stored mode is then started accordingly.

5.2.5 Network Switcher

The CCU can use two different network interfaces. The wireless network interface provided by the ACM-DB-2 mPCIe network card (up to $860\,\mathrm{Mbit\,s^{-1}}$) and the wired connection (ETH) (up to $100\,\mathrm{Mbit\,s^{-1}}$) to the ISS MRDL network. It is only allowed to use one interface at a given time to prevent accidental network overloads by internal messaging loops. Verifying software solutions for security relevant functions is more complex than to verify hardware solutions. Therefore, the hardware disable function of the mPCIe module in combination with the following program is used. The Wi-Fi module has to be actively enabled by the Jetson TX2i in order to work.

As the Wi-Fi connection has a higher bandwidth and it can be used throughout all locations on the ISS, it is the preferred network interface. To manage the network interface settings the Network Switcher program is used. A schematic overview of the program timeline sequence is given in Figure 5.9. It is started at system start and loops until a shutdown of the system.

At startup, the program fetches the configuration stored in a configuration file. The file can be adjusted by the user to select the preferred network interface for the operation of the RadMap Telescope. A

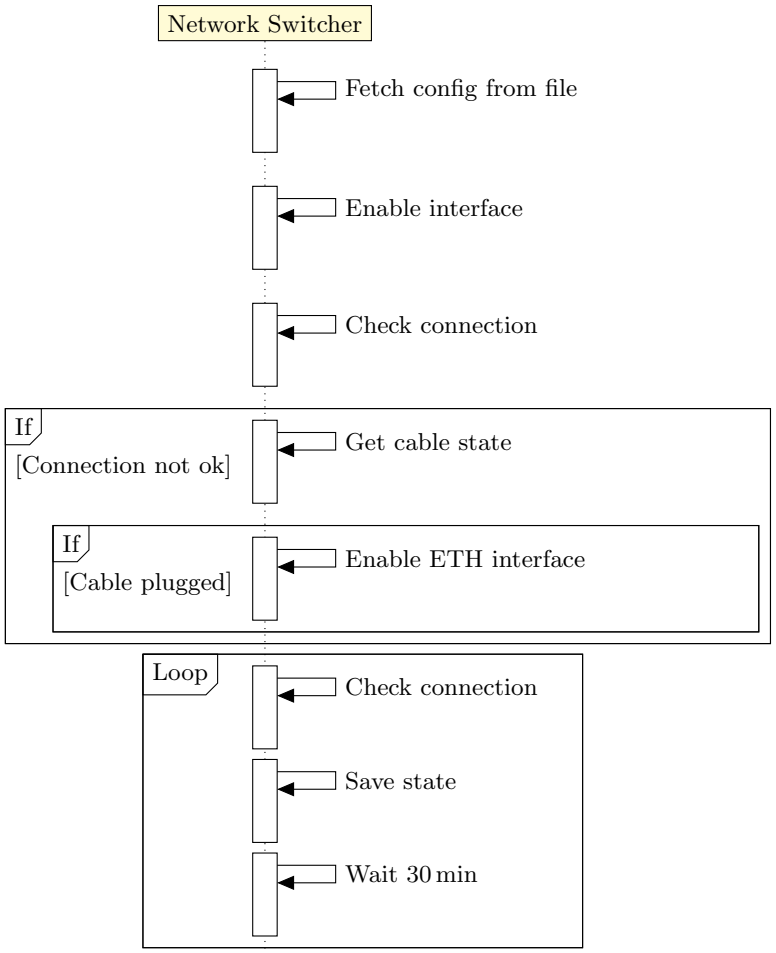

Figure 5.9: Schematic view of the Network Switcher program sequence.

file is used as source as other system like the databases may not be started correctly and the proper interface would not be configured resulting in a not accessible system after the wrong or no network interface has been enabled. The network interface stored will be configured and enabled and its connection to a network node on the ISS is checked.

This check uses the *ping* computer network administration software utility to test the reachability to the ISS gateway network node. *ping* sends echo request network packages to the node and waits for the node to answer with the echo message. If no network connection has been established the echo will not be received.

If the connection could not be checked successfully the program detects, if a cable for wired Ethernet has been plugged into the instrument. This can be done via checking a status information of the operating system and does not require the network interface to be active. If a cable is detected, the wired interface is configured and enabled.

In the case the Wi-Fi interface has to be enabled, a GPIO pin of the Jetson module is used to enable the wireless transceiver. The program will then go into an execution loop. It will check the network connection via *ping* every 30 min and saves the status of the connection in to the Telemetry database.

This procedure ensures that at a given time no more than one interface is active. If the wireless network interface is not working, the interface is not automatically switched to the wired connection as this may only be a temporary outage of one of the ISS systems.

5.2.6 MRDL Packaging

To pack and send the telemetry and dose as well as science information packages to the network the MRDL Packaging program is used. It fetches data from the databases and packs it into UDP messages using the TReK libraries provided by NASA. This enables the use of the TReK software in the laboratory to receive the transmitted messages.

Science packages include information about ADU data and a dose rate calculated from ADU data. This information is sent in real time as soon as new data is available. Telemetry and dose packages provide basic system status information and the calculated dose rates of the reference and crystal dosimeters. They are sent every 5 s.

The program can also receive commanding packages from ground. These can contain configuration values for all sensors or nodes. The information will be stored in the Configuration database.

5.2.7 Master Programs

The Science Master and the Telemetry Dose Master can be started via the Mode Selector program in different modes depending on the chosen operation mode of the RadMap Telescope. Both programs follow the same program sequence seen in Figure 5.10.

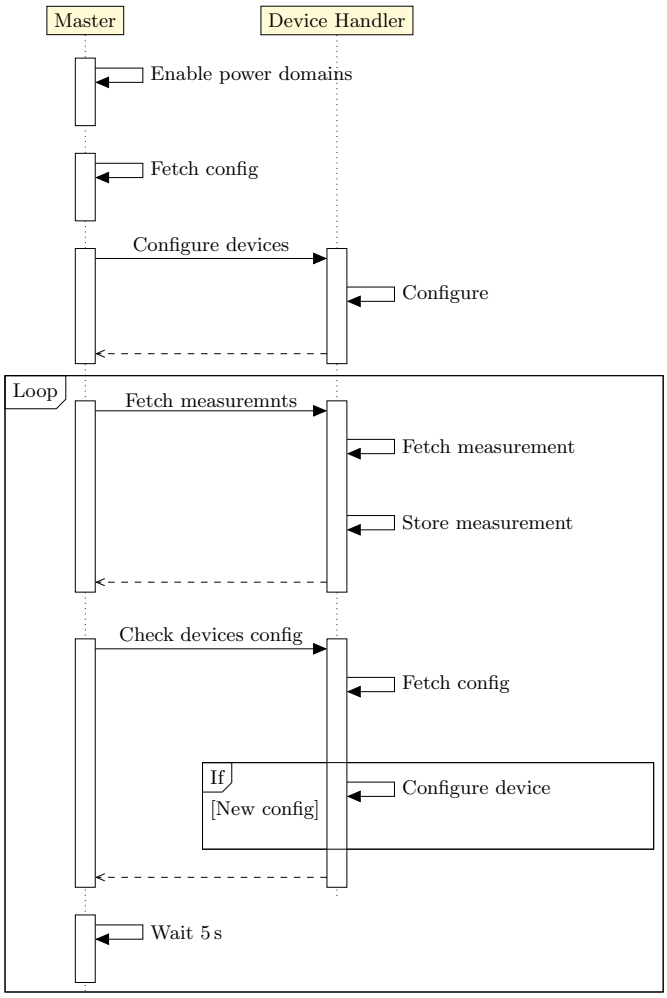

Figure 5.10: Schematic view of the CCU master program sequence.

The timeline of a master program (left) and a dummy device handler program (right) are shown. Each device handler uses code specific to the device that it controls. It provides functions to get and set values to the device such as measurements and configurations. First the power domains are switched on according to the selected operating mode. All configurations for the devices used in the specific operating mode are fetched from the Configuration database. The devices are configured accordingly by the device handler.

Afterwards, the main measurement loop is started by getting all measurement values of the configured devices. The measured values may be processed by the CCU, e.g. to calculate an accumulated dose rate. The values are stored to the databases depending on the device and data.

The current device configuration is checked with the database. If a new configuration is available, the device handler configures the device accordingly. Only devices where a change in the configuration has been detected, will be reconfigured. This enables the instrument to alter its configuration during its operation. The new configuration originates from Configuration database entries, which can be manually changed or by telemetry packages received from ground.

The program waits for 5 s and the loop starts again with gathering measurement data. To prevent artificial data loss caused by this waiting time the Science Master program reacts on interrupts to fetch the ADU data. The interrupts are caused by the FPGA of the ROE, if an ADU event has fulfilled one of the trigger condition.

The Telemetry Dose Master program collects all telemetry data from the CCU and PDU as well as the CAN bus nodes and saves the data to the Telemetry database. Furthermore, it collects the measured does rates of REF 1 & 2 and CRY 1 and 2. The dose data is saved to the Science database.

In addition to configuring the ASICs of the ROE via SPI and gathering data from the FPGA via PCIe, the Science Master program also executes the artificial neural networks with the measured data as an input. If a new configuration is detected, the measurement will stop and the device settings will be adjusted. Otherwise the program will process the ADU data with the program sequence shown in Figure 5.11.

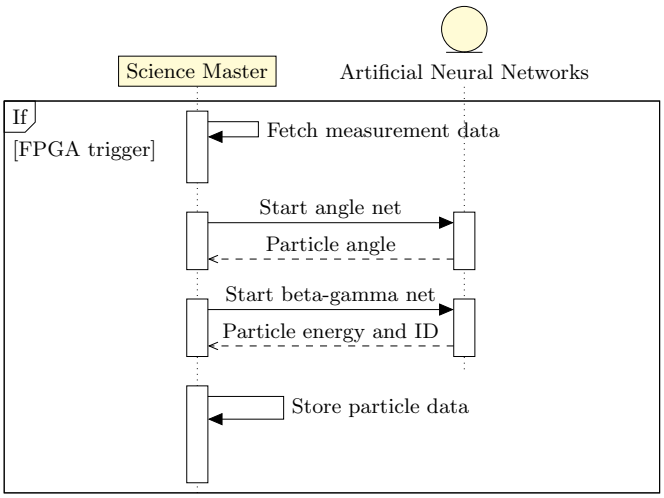

Figure 5.11: Schematic view of the Science Master program measurement sequence.

The timeline of the Science Master program (left) and the artificial neural networks (right) are shown. The program sequence shows only a schematic view of the ADU data processing part of the Science Master program.

The measurement data from the ADU is collected from the FPGA, if the ROE indicated that a trigger condition has been reached. After storing the data on the persistent storage of the CCU it will be

passed to the artificial neural networks. Detailed information about the functionality of the networks can be found in the master thesis of M. Höschler [70].

First the impact angle of the impinging particle will be determined by the so called angle artificial neural network. The resulting impact angle may have an 180° ambiguity at high energies as the timing resolution of the detector is not high enough in that range, if the particle does not stop in the detector [70], to obtain their origin. If the angle network is able to give a result, the data is passed on to the beta-gamma artificial neural network. This determines the energy and charge of the particle. Both data values are then stored in the Science database.

The Science Master offers a mode where the raw data is stored to the ISS NAS and is passed to the artificial neural networks. The NAS data will automatically be transmitted to ground and can be accessed from the E18 laboratories. This mode is used during the commissioning phase of the instrument to compare the instrument raw data analysed on ground to the on-orbit artificial neural networks calculations.

Chapter 6

Implementation

To test the selected hard- and software components in combination with each other so-called engineering models (EMs) have been built. They are PCBs that do not resemble all functions of the final flight hardware, which is also called flight model (FM).

EM boards help to simulate the behavior of the components with each other while giving access to certain aspects of the final system that otherwise cannot be tested, as they are highly integrated and most often cannot be reached by humans in the assembled FM hardware. During the design process of the RadMap Telescope CCU two EM boards and one FM board have been built.

Both EM PCBs use the standard for the Versa Module Eurocard (VME) bus system [127] and are built on a compatible PCB in terms of size and power connections. This offers easy access to all components as the PCB size is a lot bigger than the final hardware. Additionally, already existing VME compatible devices can be used throughout the design and testing process.

6.1 Engineering Model 1

To test all selected components in combination with each other a first EM (EM1) has been built. Special attention to interfaces and voltages required for the operation of the Nvidia Jetson TX2i module has been applied as it is the main component of the CCU.

6.1.1 Overview

In Figure 6.1 the board layout can be seen with some components indicated. With this board the following functions are implemented:

- Jetson TX2i power
- UART interface to debug the TX2i module and use its operating system
- ADC and thermistors
- SPI multiplexing
- mPCIe for Wi-Fi card
- Power monitors via I2C
- Pressure and attitude sensors
- CAN FD

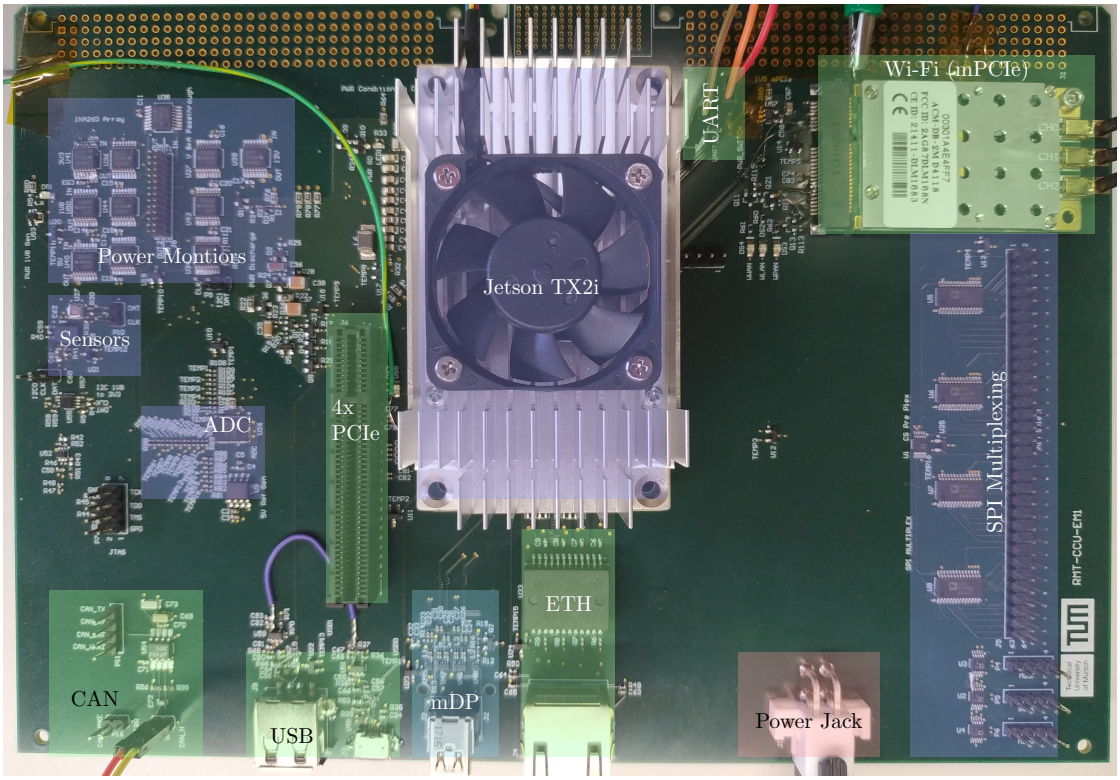

Figure 6.1: CCU EM1 PCB overview: Inputs and outputs are marked green. Display output is drawn in cyan. Power is in red. Onboard devices are blue.

- PCIe
- Gigabit Ethernet (ETH) with a standard RJ-45 jack
- Mini Display Port (mDP) for display output
- Mini USB for module configuration
- USB A jack

In order to work properly with this custom board the Jetson Module needs to have its Device Tree altered. On ARM devices (as built into the Jetson modules) this contains all information about the carrier board as well as basic configurations of the system. It is comparable to the BIOS on a x86 architecture. The pre-installed tree does not enable certain functions needed for the RadMap Telescope. The configuration file has to be compiled and flashed onto the module in order to allow for the following functions to work [128]:

- USB configuration[1]
- SPI[2]
- PCIe configuration
- Display output via the mini Display Port

[1] https://elinux.org/Jetson/TX2_USB
[2] https://elinux.org/Jetson/TX2_SPI

Altering the device tree is complex and not well documented by Nvidia. Due to this and errors made during the design and manufacturing process, the EM1 PCB has the following issues:

- Not all attached I2C devices can be accessed, since internal system devices share the same address and thereby interfere with each other.
- The BNO055 attitude sensor is not responding to normal I2C commands, as it has the pin configuration for I2C HID instead of normal I2C.
- After fixing the reset line for the PCIe x4 connector, a test with a x1 card was performed successfully.
- The mini Display Port does not show an output. This error is not fully understood, but there is a possible cause for this behaviour: The default device tree configuration asserts display interface 0 with HDMI. The mini Display Port connector is attached to interface 1 pins on the TX2i module connector. Attempts to change the device tree to accommodate this issue were unsuccessful.
- A differential pair used for the reference clock of the mPCIe interface was connected incorrectly. Additionally the LEDs used to indicate functions of the mPCIe module, do cause the attached module to power off. The issues were fixed by re-soldering of the differential pair and removing the LEDs.
- The Ethernet connection was responding very slowly to connected networks (only $100\,\mathrm{Mbit\,s^{-1}}$ could be achieved) and does need higher voltages than normal. This is caused by an incorrect connected RJ-45 jack. The problem has been solved and a gigabit connection has been tested.
- On both USB connectors the data line differential pairs are connected incorrectly. The 5 V rail is not attached correctly on the USB A jack. Both problems have been fixed.
- The enable pin of all ICs used for SPI multiplexing is connected to 3.3 V. If the SPI interface is switched to a different device on the bus, unwanted signals produced by the switching ICs are disturbing the signal.
- The temperature ADC needs additionally to the operating voltage a reference voltage. This voltage is 3.3 V instead of 2.5 V since a wrong chip has been used to produce the reference voltage.
- The JTAG debug connector cannot be used with standard debuggers as it does not use the JTAG standard connector.
- For development the Jetson TX2 module can be used. The TX2 module needs a power button signal in order to power up. This is not required for the TX2i as it powers up automatically, if supplied with the correct voltages. A cable had to be added to enable automatic power-on also for the TX2 module.
- The 1.8 V converter is not working due to a missing $10\,\mathrm{k\Omega}$ resistor between in and output. This problem has been fixed.
- Wrongly placed resistors created a short on the reset line of the TX2 module. This prevented the module to power up, but has been fixed.

6.1.2 Tests

Despite theses problems the network capabilities could be verified with the wired connection as well as with the Wi-Fi extension card. The SPI multiplexer switching and the SPI interface could be tested successfully. Power monitors and the pressure sensor that were accessible could be tested and delivered measurement results.

CAN (FD)

Extensive CAN bus testing with the new protocol could be performed in combination with an ATMega128 on a development board. This test measured the performance of the new protocol using 8-byte CAN messages and 64-byte long CAN FD message. The ATMega node used an LTC2875 and MCP2517FD as described earlier. It was configured to use the commanding scheme as shown in section 5.1.1.

CAN is capable of sending the header at a slower data rate than the actual data. Two different settings have been tested:

- Header: 500 kHz, Data: 2 MHz
- Header: 1000 kHz, Data: 8 MHz

100 messages of the CANTEST type were requested by the Nvidia module from the ATMega128 with different request intervals. For the standard CAN the CANTEST message data content was adjusted to fit in the 8-byte CAN message. All received frames were checked for their integrity. Only frames with full integrity are treated as received.

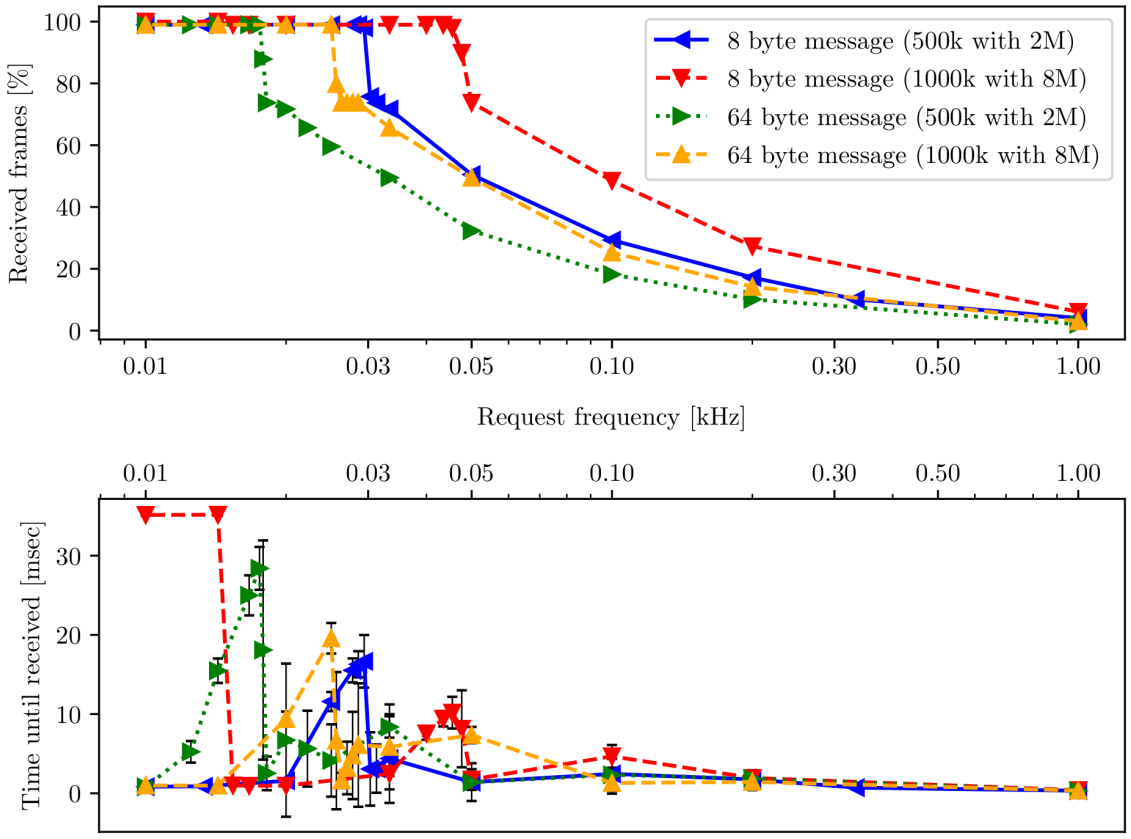

Figure 6.2: Tests with CAN and CAN FD message and different CAN bus settings with the new protocol: Time until the message was received (bottom) and the amount of successful received frames (top) at a given request frequency.

In Figure 6.2 the amount of successful received frames and the time until the requested data arrived at the Nvidia module for different request frequency are shown. At the slower rate setting all messages can be received until 30 Hz for CAN and 15 Hz request frequency for CAN FD. The higher rate setting all messages are received until 48 Hz and 28 Hz respectively. At frequencies slightly lower as these

the time until a request by the TX2 is resulting in a received frame increases, because the internal memory buffer of the CAN controller getting full and the ATMega is not fast enough the clear the buffer before the next frame arrives. After the received frame amount drops, the time until a frame is received drops to about 0 ms, as only the time of correct received frames is shown.

For CAN the maximum data rate that can be achieved with this hardware and the new protocol is 3.1 kbit s^{-1}. A maximum data rate of 14.4 kbit s^{-1} could be measured when using CAN FD.

PCIe Integrity

The design of the instrument introduces several connectors and imposes longer signal lines than 13.97 cm (recommended by the Jetson TX2 design guide [129]) that a PCIe signal has to pass from the Jetson module to the ROE. These introduce impedance characteristic changes as well as resistance to the data connection, which lead to a degraded signal and in the worst case to signal loss [130].

To test the impact of long signal lines and multiple connectors in the case of the RadMap Telescope, a test with PCIe extension cables (riser) was conducted. One cable extends the signal path by 20 cm and up to two were connected together. The PCIe connector of the EM1 board was used. As a PCIe device a mPCIe Wi-Fi module was used in combination with a mPCIe to PCIe adapter. The Wi-Fi card uses one lane of the PCIe interface which can achieve up to 2 Gbit s^{-1}.

To test the signal integrity, UDP network packages were sent via the Wi-Fi card to a server. 20 simultaneous data streams with up to 40 Mbit s^{-1} per stream were used to potentially utilize the maximum data rate of the card (860 Mbit s^{-1}). The total data rate, that the system could achieve over a test duration of 10 s, is shown in Figure 6.3.

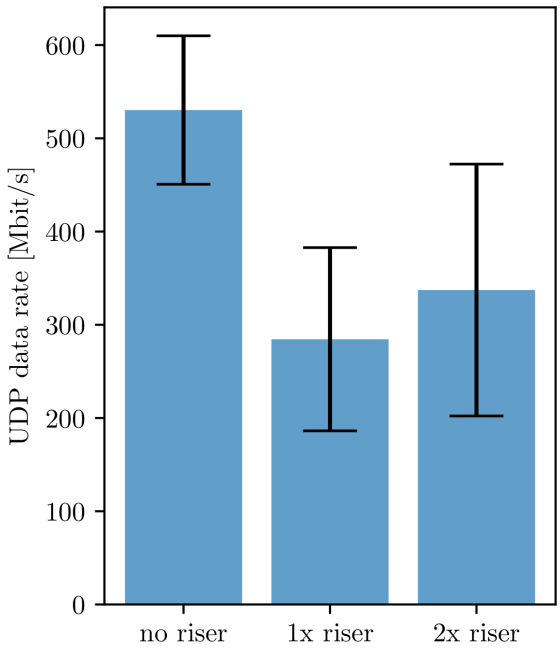

Figure 6.3: PCIe benchmark test with up to two 20 cm extension cables (riser).

With no extension cable used a data rate of (530 ± 80) Mbit s^{-1} could be achieved. (285 ± 98) Mbit s^{-1} and (375 ± 146) Mbit s^{-1} could be achieved for one and two attached extension cables. It is unclear why adding a second cable did improve the data rate. Extending the PCIe signal path to the Wi-Fi module influences the signal integrity up to 46 %.

To achieve the highest possible data rates between the CCU and ROE, a PCIe signal booster could be used, but is not required as the needed bandwidth of 12.3 Mbit s^{-1} even with multiple connectors and long signal traces can be achieved.

6.2 Engineering Model 2

A second EM (EM2) was built to fix the issues of EM1 and to be used with in a VME server rack in combination with engineering models of other subsystems such as the PDU to test all subsystems of the RadMap Telescope together.

6.2.1 Overview

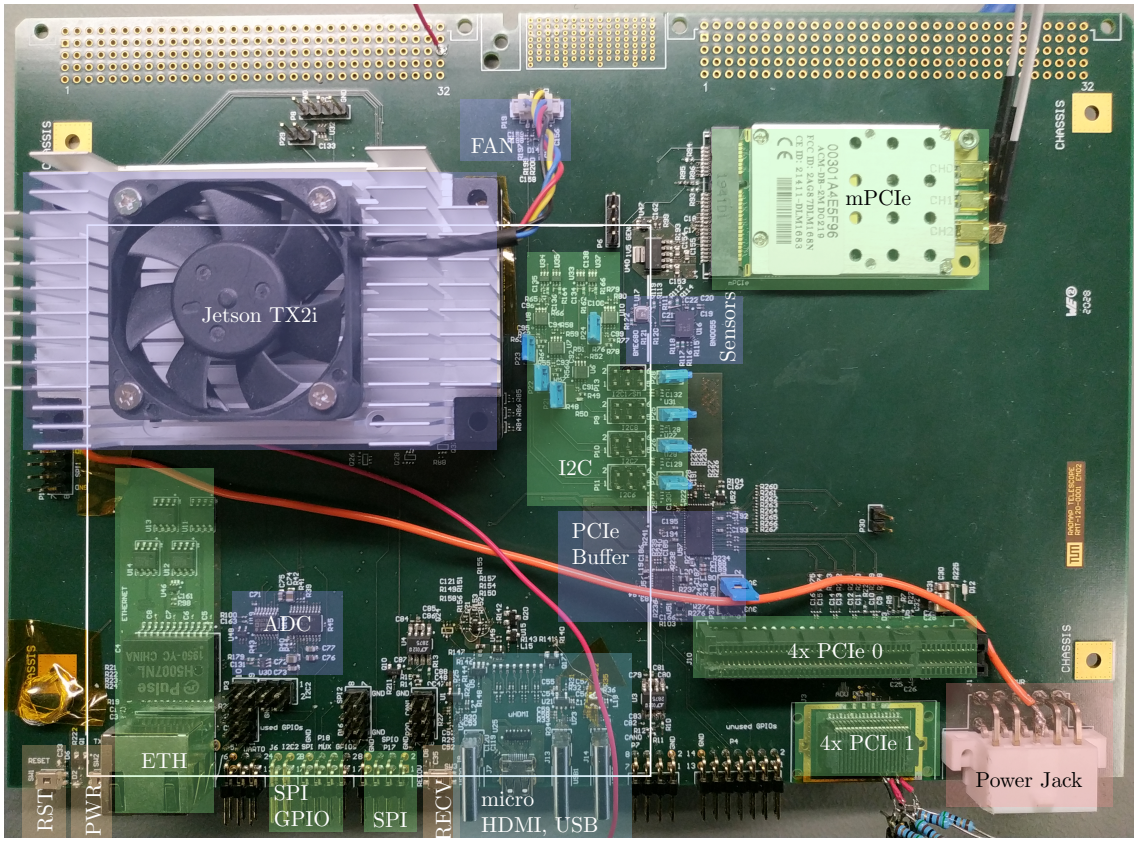

Figure 6.4: CCU EM2 PCB overview: Inputs and outputs are marked green. Display output is drawn in cyan. Power is in red. Onboard devices are blue. White rectangle indicates area of FM hardware.

Figure 6.4 shows an overview of the EM2 PCB. The following key features are implemented in addition of the EM1 functions:

- Reset, power and recovery mode buttons
- PCIe buffer for clock (9DBL02x2 [131]) and a four lane interface (DS80PCI402 [132])
- Additional compact PCIe [133] (PCIe 1) compatible connector for use with other EMs
- Three USB C jacks for flashing and other USB devices
- Micro HDMI connector for display output
- A connector for the fan of the heat sink shipped with the Jetson modules
- All I2C lines use the LTC4311 [134] to improve the signal integrity

- More debug headers for GPIO, I2C, SPI and CAN

All important components were roughly placed on the same area of the FM as indicated by the white rectangle. As all connectors had to be reachable while the card is placed inside the server rack, some interfaces had to be moved along the edge of the card.

In order to work properly with the EM2 board, the Device Tree of the Jetson Module has to be altered in the same way apart from the display output as for the EM1 PCB. The debug USB was used to flash the TX2 and TX2i modules.

The board has the following issues:

- Since the 2.0 specification uses 500 mA, a USB 3.0 device which is allowed to use up to 900 mA may not work properly.
- Unfortunately the same errors were made with the signal routing to the Ethernet RJ-45 connector. It has been fixed and a gigabit connection is available.
- The GPIO voltage level shifting from 1.8 V used by the Jetson module to more commonly used 3.3 V had to be fixed with a separate PCB. Not all GPIOs can be used with the un-altered device tree.
- The I2C voltage shifting for the micro HDMI port had to be fixed. After also fixing a short to ground on the connector the HDMI connection shows a display output.
- A proper PCIe connection could not be established even though signals did pass the PCIe lane buffer. The reference clock buffer is working fine and improving the signal. Since the connection to the Jetson module is fine, the problem seems to be with the PCIe lane buffer.

6.2.2 Tests

All power monitors and ADCs of the CCU and PDU measurements could be received via the common I2C interface. The pressure and acceleration measurements were successfully received by the Jetson compute module. In addition the mPCIe interface has been tested to see if the repair compared to the EM1 has improved the connection and a power consumption measurement for the new operating modes has been conducted.

mPCIe Improvement

The error in differential lane routing of the mPCIe connector that is present on the EM1, was not made on the EM2. To validate the signal integrity improvement of the mPCIe connection over the EM1 board the same test procedure as described in section 6.1.2 was used. A mPCIe Wi-Fi card was used on the EM1 and EM2 via the mPCIe interface connector.

As seen in Figure 6.5 the data rate could be improved by 25 % from $(412 \pm 163)\,\mathrm{Mbit\,s^{-1}}$ to $(542 \pm 114)\,\mathrm{Mbit\,s^{-1}}$.

Power Consumption

For each operating mode also a custom power mode for the Jetson TX2i has been created. To measure the CCU power consumption in idle and under load of each mode the same test as described in section 4.1.1 has been conducted with the custom power modes described in section 5.2.4. The values were measured with a laboratory power supply and did not involve other power converters in-between. The power consumption under load (CPU and GPU) and in idle state of the EM2 are shown in Figure 6.6.

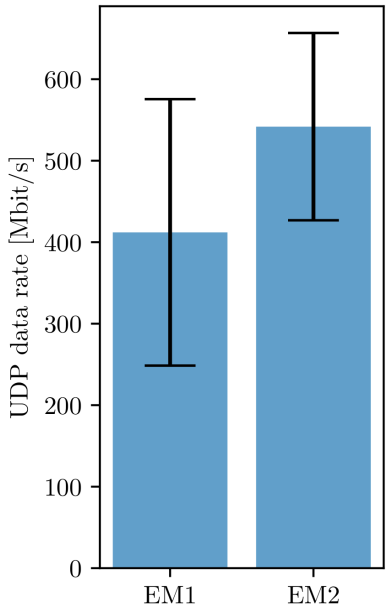

Figure 6.5: mPCIe benchmark test with a mPCIe Wi-Fi card on EM1 and EM2.

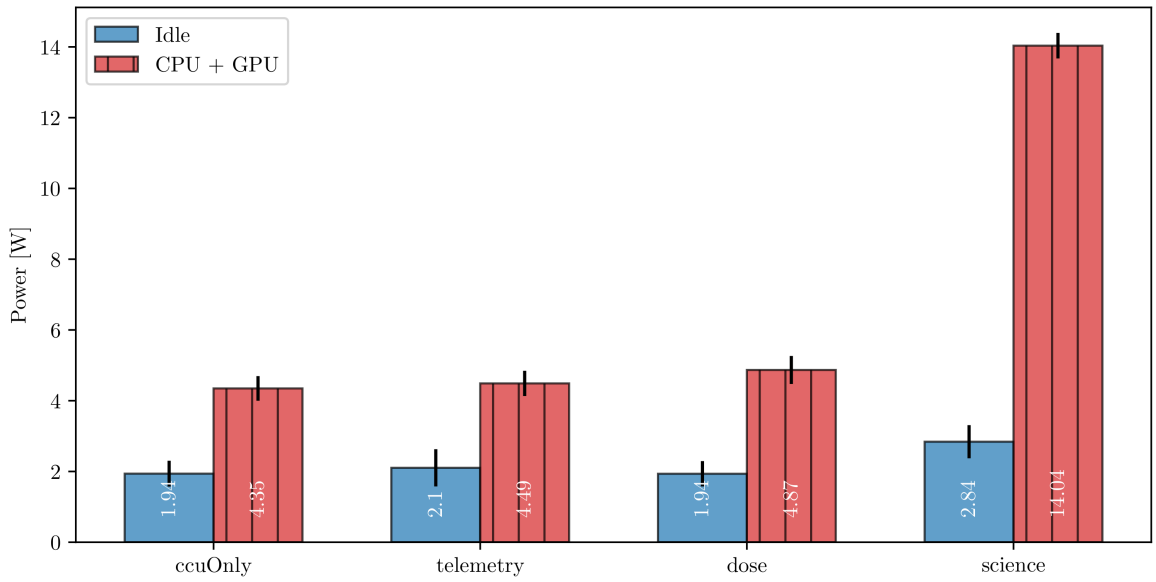

Figure 6.6: Combined GPU and CPU CCU power consumption: Colour shows idle (blue) and load (red) power consumption in different operating modes. Standard deviation from mean values are indicated with black error bars.

The PCIe buffers were turned off[3]. The Wi-Fi card was powered during the test but not used. The power consumption is mainly dominated by the TX2i and the power consumption of other devices was 0.5 W and has been added to the Jetson compute module power consumption as a constant in each mode as the different operating modes do not change the hardware active on the CCU.

Results for separate CPU and GPU measurements can be found in section A.3. The CCU takes about 2.0 W in idle in all modes but the science mode (2.84 W) and can need up to (14.04 ± 0.40) W in science mode, if the CPU and GPU are fully utilized. All modes do not need more than 15 W and fit the requirements.

6.3 Flight Model

The layout of EM2 showed that all needed devices should fit on the final board and all interfaces could be verified. The flight hardware (FM) is placed in the lower compartment of the RadMap Telescope (Figure 2.3).

As the PCIe buffers did not work as expected and the PCIe benchmark test showed that they are not mandatory in order to achieve the data rates required for the operation of the instrument, the FM does not implement them.

As seen in Figure 6.7 the Jetson TX2i compute module is placed in the middle and is attached to the main cooling channel of the RadMap Telescope. Ethernet and power connections are routed to the connectors on the outside of the case via the connector on one side. The PDU PCB is attached to the cooling channel and is connected through a port next to the connector for the Jetson compute module. On the opposite side of the cooling channel the mPCIe Wi-Fi module with a separate PCB is placed. A connector on the PCB routes the mPCIe signals to the CCU.

In the lower left corner, where the aluminium case has the service hatch, a micro HDMI and USB connectors as well as a Enhanced Small Form Factor Pluggable Module (SFP+) [135] are placed. The SFP+ is used for a direct connection to the FPGA of the ROE during development. Buttons for flashing mode and reset of the Jetson module are also accessible through the hatch. These buttons require a minimum force of 450 g to be activated to prevent accidental resets by vibrations or shocks. The connector on the bottom routes the following connections to the upper compartment:

- Power for domains D0, D2, D3, D4 and D5
- PCIe with four lanes
- CAN FD for all nodes
- SPI for the ASICs of the ROE
- SFP+ for the FPGA
- USB for a JTAG debugger used for in flight access of the CCU to the FPGA configuration

[3] If turned on, they need about 1 W during operation.

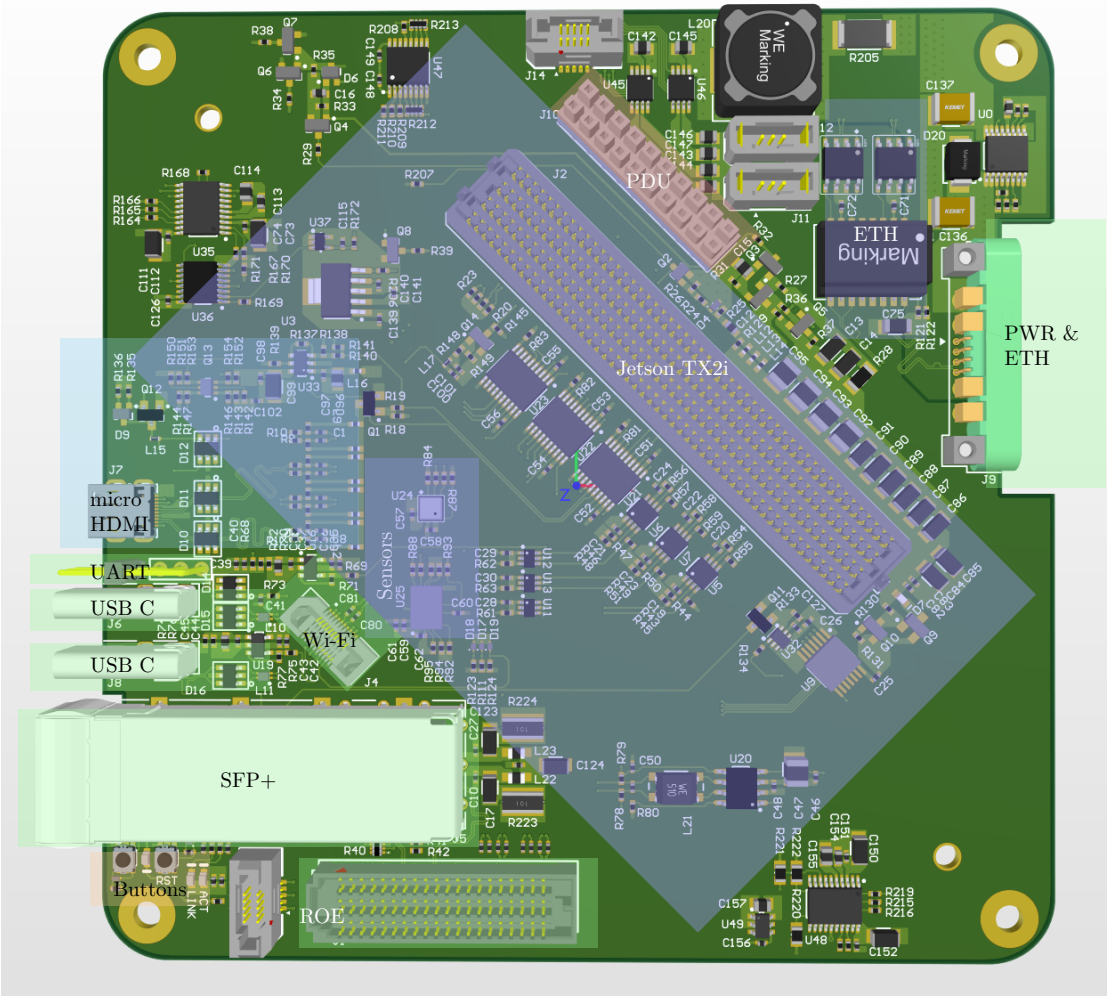

Figure 6.7: CCU FM PCB overview: The board is roughly 10 cm by 10 cm. Inputs and outputs are marked green. Display output is drawn in cyan. Power is in red. Onboard devices are blue.

Chapter 7

Mission Status and Outlook

The RadMap Telescope will have its final integration test campaign with replicas of the ISS systems in NASA laboratories in 2021. All astronaut safety related aspects will be tested as well as the integration into ISS facilities. Until this test the presented hardware will be used to test several EMs of different system with each other and also a full integration test will be conducted. Several different EMs still have to be built and tested. This includes PCBs for all CAN nodes as well as the FPGA and ROE boards.

The ADU calibration tests to measure the response functions of the fibers did already take place in September 2020 and are validated at the moment. A test with the Jetson TX2 development board and very early version of the flight software was conducted in NASA laboratories in March 2020. During this test also network messages were recorded. These can be retransmitted using the ISS test facilities to simulate the TReK data transmission services between the ISS to the facilities of E18. At the moment the ground station server for this purpose is being built and this test has yet to be done.

Future deep space missions on satellites or human rated spacecrafts may use the onboard computing solution provided by the spacecraft instead of the CCU solution presented here. As development and understanding of the used artificial neural networks evolve, also other options as a GPU based solution may be possible. The networks developed during the RadMap Telescope deployment on the ISS may be used in a FPGA based system where not only triggering is done on the FPGA hardware, but also the event processing [136].

Chapter 8

Summary

The goal of the presented work was to develop a flight computer and the system architecture of the RadMap Telescope. The experiment wants to validate a compact radiation monitoring device for deep space missions. It uses a combination of flight-proven and new dosimeters as well as spectrometer to deliver near-real time particle characterisation and dose rates.

As a flight computer a Nvidia Jetson TX2i compute module is used. It connects to a scintillating fiber-based active detection unit (ADU) and a CAN bus with four additional dosimeters. The flight proven DLR M-42 dosimeter and a not jet fixed commercial solution are used as a reference to calibrate the ADU and two additional new crystal dosimeters. The flight computer is used to gather data from the CAN nodes as well as the ADU. The ADU data will be analysed by artificial neural networks running on the built-in GPU of the computer.

The instrument automatically collects ADU and dosimeter dose data and stores it in PostgreSQL managed databases. The Medium Rate Data Link of the ISS can be used to broadcast the gathered information to the ground or to receive commanding packages which alter the configuration of the instrument. Two network interfaces can be used for this purpose. A wired Fast Ethernet connection with up to $100\,\mathrm{Mbit\,s^{-1}}$ and a Doodle Labs ACM-DB-2 wireless transceiver with up to $860\,\mathrm{Mbit\,s^{-1}}$. A software routine in combination with a hardware disable ensures that only one interface is used by the instrument at a given time.

A new protocol to request and configure the CAN FD bus nodes has been developed. Data rates up to $14.4\,\mathrm{kbit\,s^{-1}}$ can be achieved using this protocol between the flight computer and a CAN node.

Four different operating modes have been defined for the operation of the RadMap Telescope. Each mode has a different power setting to save power, if devices are not needed. In science mode all sensors and detectors are active and the measured dose rates and particle information are transmitted to Earth. The CCU needs up to 14.4 W in this mode.

Two engineering and one flight model have been built during the development and can be used for further testing and development. The flight hardware has the following main features:

- PCIe link to the ADU
- mPCIe link to the wireless transceiver
- Fast Ethernet
- CAN FD
- Micro HDMI display output
- Two USB 2.0 compatible USB C connectors
- Temperature, pressure and attitude sensors

Bibliography

[1] Francis A. Cucinotta et al. 'How Safe Is Safe Enough? Radiation Risk for a Human Mission to Mars'. In: *PLoS ONE* 8.10 (2013). DOI: 10.1371/journal.pone.0074988.

[2] National Research Council. 'Radiation Hazards to Crews of Interplanetary Missions'. In: *Radiation Hazards to Crews of Interplanetary Missions*. National Academies Press, Feb. 1996. DOI: 10.17226/5540.

[3] Donald V. Reames. 'Particle Acceleration at The Sun and in the Heliosphere'. In: *Space Science Reviews* 90 (1999), pp. 413–491.

[4] A. Aab et al. 'Observation of a large-scale anisotropy in the arrival directions of cosmic rays above 8 × 1018 eV'. In: *Science* 357.6357 (2017), pp. 1266–1270. DOI: 10.1126/science.aan4338.

[5] E R. Benton and E V Benton. 'Space radiation dosimetry in low-Earth orbit and beyond'. In: *Nuclear Instruments and Methods in Physics Research, Section B: Beam Interactions with Materials and Atoms* 184.1-2 (2001), pp. 255–294. DOI: 10.1016/S0168-583X(01)00748-0.

[6] James A. Van Allen. 'Radiation Belts around the Earth'. In: *Scientific American* 200.3 (1959), pp. 39–46. DOI: 10.1038/scientificamerican0359-39.

[7] J. A. Simpson et al. 'The protons and electrons trapped in the Jovian dipole magnetic field region and their interaction with Io'. In: *Journal of Geophysical Research* 79.25 (1974), pp. 3522–3544. DOI: 10.1029/ja079i025p03522.

[8] Rudolf A Hoffman and John W Wilson. 'WORKSHOP ON THE RADIATION ENVIRONMENT OF THE SATELLITE POWER SYSTEM'. In: (1978).

[9] D. J. McComas et al. 'Interplanetary magnetic field draping about fast coronal mass ejecta in the outer heliosphere'. In: *Journal of Geophysical Research* 93.A4 (1988), p. 2519. DOI: 10.1029/ja093ia04p02519.

[10] J G Roederer et al. *Physics and Chemistry in Space Volume 1*. Vol. 1. 1972.

[11] Richard C Willson and Hugh S Hudsont. 'Complete Solar Cycle'. In: 351.May (1991), pp. 42–44.

[12] Robert B. Leighton. 'A Magneto-Kinematic Model of the Solar Cycle'. In: *The Astrophysical Journal* 156 (1969), p. 1. DOI: 10.1086/149943.

[13] David H. Hathaway. 'The solar cycle'. In: *Living Reviews in Solar Physics* 12.1 (Sept. 2015), pp. 1–87. DOI: 10.1007/lrsp-2015-4. URL: https://link.springer.com/article/10.1007/lrsp-2015-4.

[14] H. S. Hudson, L. W. Acton and S. L. Freeland. 'A Long-Duration Solar Flare with Mass Ejection and Global Consequences'. In: *The Astrophysical Journal* 470 (1996), p. 629. DOI: 10.1086/177894.

[15] G M Lindsay et al. 'Relationships between coronal mass ejection speeds from coronagraph images and interplanetary characteristics of associated interplanetary coronal mass ejections'. In: *Journal of Geophysical Research: Space Physics* 104.A6 (1999), pp. 12515–12523. DOI: 10.1029/1999ja900051.

[16] Max Gleber. *The Difference Between Flares and CMEs | NASA*. Aug. 2017. URL: https://www.nasa.gov/content/goddard/the-difference-between-flares-and-cmes (visited on 02/11/2020).

[17] Piers T.A. Jiggens et al. 'ESA SEPEM project: Peak flux and fluence model'. In: *IEEE Transactions on Nuclear Science* 59.4 PART 1 (2012), pp. 1066–1077. DOI: 10.1109/TNS.2012.2198242.

[18] C. M.S. Cohen et al. 'New observations of heavy-ion-rich solar particle events from ACE'. In: *Geophysical Research Letters* 26.17 (1999), pp. 2697–2700. DOI: 10.1029/1999GL900560.

[19] R A Mewaldt et al. 'Proton, helium, and electron spectra during the large solar particle events of October-November 2003'. In: *Journal of Geophysical Research: Space Physics* 110.A9 (2005), pp. 9–18. DOI: 10.1029/2005JA011038. URL: http://www.ssg.sr..

[20] Marc-André Chavy-Macdonald. 'Strategies and Geant4 Simulations for Radiation Protection on an EML-2 Mission January'. In: June (2014), pp. 97–168. DOI: 10.13140/RG.2.1.2646.2881.

[21] D. F. Smart and M. A. Shea. 'Solar proton events during the past three solar cycles'. In: *Journal of Spacecraft and Rockets* 26.6 (1989), pp. 403–415. DOI: 10.2514/3.26086.

[22] M. Ackermann et al. 'Detection of the characteristic pion-decay signature in supernova remnants'. In: *Science* 339.6121 (2013), pp. 807–811. DOI: 10.1126/science.1231160. arXiv: 1302.3307.

[23] A. R. Bell. 'Cosmic ray acceleration'. In: *Astroparticle Physics* 43 (Mar. 2013), pp. 56–70. DOI: 10.1016/j.astropartphys.2012.05.022.

[24] Andrew W Strong, Igor V Moskalenko and S Vladimir. 'Cosmic-ray propagation and interactions in the Galaxy'. In: (2008), pp. 1–39. arXiv: 0701517v1 [arXiv:astro-ph].

[25] J A Simpson. 'Elemental and Isotopic Composition of the Galactic Cosmic Rays'. In: *Annual Review of Nuclear and Particle Science* 33.1 (Dec. 1983), pp. 323–382. DOI: 10.1146/annurev.ns.33.120183.001543.

[26] T Slaba, S Blattnig and J Norbury. *Space Radiation Environment Comparison and Validation of GCR Models*. Tech. rep. April. 2015.

[27] T. W. Armstrong and K. C. Chandler. 'Stopping powers and ranges for muons, charged pions, protons, and heavy ions'. In: *Nuclear Instruments and Methods* 113.2 (1973), pp. 313–314. DOI: 10.1016/0029-554X(73)90852-5.

[28] S. M. Seltzer et al. 'Fundamental quantities and units for ionizing radiation'. In: *Journal of the ICRU* 11.1 (2011), pp. 1–41. DOI: 10.1093/jicru/ndr011.

[29] Stanley B. Curtis. 'Calculated let distributions of heavy ion beams'. In: *International Journal of Radiation Oncology, Biology, Physics* 3.C (1977), pp. 87–91. DOI: 10.1016/0360-3016(77)90232-2.

[30] Richard S Johnston, Lawrence F Dietlein and Charles A Berry. *Biomedical Results of Apollo*. Tech. rep. NASA, Jan. 1975. URL: https://ntrs.nasa.gov/search.jsp?R=19760005580.

[31] M. H. Acuña et al. 'Magnetic field and plasma observations at Mars: Initial results of the Mars global surveyor mission'. In: *Science* 279.5357 (1998), pp. 1676–1680. DOI: 10.1126/science.279.5357.1676.

[32] Michael E Purucker. 'A global model of the internal magnetic field of the Moon based on Lunar Prospector magnetometer observations'. In: *Icarus* 197.1 (2008), pp. 19–23. DOI: 10.1016/j.icarus.2008.03.016.

[33] C. T. Russell. 'The solar wind interaction with the earth's magnetosphere: A tutorial'. In: *IEEE Transactions on Plasma Science* 28.6 (2000), pp. 1818–1830. DOI: 10.1109/27.902211.

[34] N. Sato and Z. Yoshida. 'Charged particle diffusion in a magnetic dipole trap'. In: *AIP Conference Proceedings* 1928.January (2018). DOI: 10.1063/1.5021579. arXiv: 1709.00783.

[35] *ESA - Space Environment - Radiation environment*. 2013. URL: https://web.archive.org/web/20130224063817/http:/www.esa.int/TEC/Space%7B%5C_%7DEnvironment/SEMEF3T4LZE%7B%5C_%7D0.html (visited on 02/11/2020).

[36] D. N. Baker et al. 'A long-lived relativistic electron storage ring embedded in earth's outer van allen belt'. In: *Science* 340.6129 (Apr. 2013), pp. 186–190. DOI: 10.1126/science.1233518.

[37] J. E. Naugle and D A Kniffen. 'Flux and energy spectra of the protons in the inner Van Allen belt'. In: *Physical Review Letters* 7.1 (1961), pp. 3–6. DOI: 10.1103/PhysRevLett.7.3.

[38] Paul Sommers. 'Extensive air showers and measurement techniques'. In: *Comptes Rendus Physique* 5.4 (2004), pp. 463–472. DOI: 10.1016/j.crhy.2004.03.009.

[39] Glenn F. Knoll. *Radiation Detection and Measurement, 4th Edition*. 2010. DOI: 10.1109/PROC.1981.12016.

[40] M. Tanabashi et al. 'Review of Particle Physics'. In: *Physical Review D* 98.3 (2018), p. 30001. DOI: 10.1103/PhysRevD.98.030001. URL: https://doi.org/10.1103/PhysRevD.98.030001.

[41] Thomas Pöschl. 'Modeling and Prototyping of a Novel Active-Target Particle Detector for Balloon and Space Applications'. In: (2015).

[42] C R Gruhn et al. 'Bragg curve spectroscopy'. In: *Nuclear Instruments and Methods* 196.1 (1982), pp. 33–40. DOI: 10.1016/0029-554x(82)90612-7.

[43] Marco Durante and Francis A. Cucinotta. 'Physical basis of radiation protection in space travel'. In: *Reviews of Modern Physics* 83.4 (2011). DOI: 10.1103/RevModPhys.83.1245.

[44] E J Wyrwas and Analysis Group. 'Proton Testing of nVidia Jetson TX'. In: October (2016), p. 15.

[45] Francis A. Cucinotta and Marco Durante. 'Cancer risk from exposure to galactic cosmic rays: implications for space exploration by human beings'. In: *Lancet Oncology* 7.5 (2006), pp. 431–435. DOI: 10.1016/S1470-2045(06)70695-7.

[46] Janapriya Saha et al. 'Biological Characterization of Low-Energy Ions with High-Energy Deposition on Human Cells'. In: *Radiation Research* 182.3 (2014), p. 282. DOI: 10.1667/rr13747.1.

[47] Oleg V. Belov et al. 'Neurochemical insights into the radiation protection of astronauts: Distinction between low- and moderate-LET radiation components'. In: *Physica Medica* 57 (2019), pp. 7–16. DOI: 10.1016/j.ejmp.2018.12.003.

[48] Francis A. Cucinotta. 'Biophysics of NASA radiation quality factors'. In: *Radiation Protection Dosimetry* 166.1-4 (2015), pp. 282–289. DOI: 10.1093/rpd/ncv144.

[49] Kotaro Ozasa et al. 'Erratum: Studies of the mortality of atomic bomb survivors, report 14, 1950-2003: An overview of cancer and noncancer diseases (Radiation Research (2012) 177:3)'. In: *Radiation Research* 179.4 (2013). DOI: 10.1667/RROL05.1.

[50] Oliver Jäkel. 'Radiation hazard during a manned mission to Mars'. In: *Zeitschrift fur Medizinische Physik* 14.4 (2004), pp. 267–272. DOI: 10.1078/0939-3889-00229.

[51] Jeffery C. Chancellor, Graham B.I. Scott and Jeffrey P. Sutton. 'Space radiation: The number one risk to astronaut health beyond low earth orbit'. In: *Life* 4.3 (2014), pp. 491–510. DOI: 10.3390/life4030491.

[52] G. Dietze et al. 'ICRP publication 123: Assessment of radiation exposure of astronauts in space'. In: *Annals of the ICRP* 42.4 (2013), pp. 1–339. DOI: 10.1016/j.icrp.2013.05.004.

[53] L. Lindborg et al. 'The use of TEPC for reference dosimetry'. In: *Radiation Protection Dosimetry* 86.4 (1999), pp. 285–288. DOI: 10.1093/oxfordjournals.rpd.a032959.

[54] Guenther Reitz et al. 'Space radiation measurements on-board ISS - The DOSMAP experiment'. In: *Radiation Protection Dosimetry* 116.1-4 (Dec. 2005), pp. 374–379. DOI: 10.1093/rpd/nci262. URL: http://academic.oup.com/rpd/article/116/1-4/374/1601131/Space-radiation-measurements-onboard-ISSthe-DOSMAP.

[55] D. Zhou et al. 'Radiation measured for ISS-Expedition 12 with different dosimeters'. In: *Nuclear Instruments and Methods in Physics Research, Section A: Accelerators, Spectrometers, Detectors and Associated Equipment* 580.3 (Oct. 2007), pp. 1283–1289. DOI: 10.1016/j.nima.2007.06.091. URL: https://www.sciencedirect.com/science/article/pii/S0168900207013782.

[56] M.D. Richard S. Williams. 'Nasa Space Flight Human-System Standard Volume 1, Revision A: CREW HEALTH'. In: 1 (2015), p. 83. URL: https://standards.nasa.gov/standard/nasa/nasa-std-3001-vol-1%7B%5C%%7D0A.

[57] Thomas Berger et al. 'DOSIS {\&} DOSIS 3D: Radiation measurements with the DOSTEL instruments onboard the Columbus Laboratory of the ISS in the years 2009-2016'. In: *Journal of Space Weather and Space Climate* 7.March (2017). DOI: 10.1051/swsc/2017005.

[58] Jarvis A. Caffrey and D. M. Hamby. 'A review of instruments and methods for dosimetry in space'. In: *Advances in Space Research* 47.4 (2011), pp. 563–574. DOI: 10.1016/j.asr.2010.10.005. URL: http://dx.doi.org/10.1016/j.asr.2010.10.005.

[59] Martin J. Losekamm et al. 'Real-time omnidirectional radiation monitoring on spacecraft'. In: *AIAA Space and Astronautics Forum and Exposition, SPACE 2016* (2016), pp. 1–9. DOI: 10.2514/6.2016-5532.

[60] Edward C. Posner and Robertson Stevens. 'Deep Space Communication-Past, Present, and Future'. In: *IEEE Communications Magazine* 22.5 (1984), pp. 8–21. DOI: 10.1109/MCOM.1984.1091955.

[61] SensL. 'An Introduction to the Silicon Photomultiplier Introduction to SiPM'. In: *Technical note* (2011), pp. 1–16.

[62] OnSemiconductor. 'Introduction to the Silicon Photomultiplier (SiPM)'. In: *Technical note* (2018), pp. 1–12. URL: www.onsemi.com.

[63] OnSemiconductor. 'Biasing and Readout of ON Semiconductor SiPM Sensors'. In: *Technical note* (2019), pp. 1–10.

[64] Jacob Job Wijker. *Spacecraft structures*. Springer Berlin Heidelberg, 2008, pp. 1–504. DOI: 10.1007/978-3-540-75553-1.

[65] D Renker and E Lorenz. 'Advances in solid state photon detectors'. In: *Journal of Instrumentation* 4.4 (2009). DOI: 10.1088/1748-0221/4/04/P04004.

[66] KETEK GmbH. *Product Data Sheet SiPM – Silicon Photomultiplier PM3325-WB-D0*. 2020.

[67] Ideas. 'IDE3380 ASIC Datasheet'. In: (2017), pp. 1–46.

[68] Martin J. Losekamm et al. 'The AFIS detector: Measuring antimatter fluxes on nanosatellites'. In: *Proceedings of the International Astronautical Congress, IAC* 5.September (2014), pp. 3468–3476. DOI: 10.13140/RG.2.1.4996.0405.

[69] Thomas Pöschl et al. 'A novel cubesat-sized antiproton detector for space applications'. In: *Proceedings of Science* 30-July-20 (2015), pp. 1–8. DOI: 10.22323/1.236.0590.

[70] Maximilian Hoechler. 'Particle Identification for a Radiation Monitor based on Neural Networks'. PhD thesis. 2020.

[71] T. Berger et al. 'The German Aerospace Center M-42 radiation detector-A new development for applications in mixed radiation fields'. In: *Review of Scientific Instruments* 90.12 (2019). DOI: 10.1063/1.5122301.

[72] Marvin J. Weber. 'Inorganic scintillators: Today and tomorrow'. In: *Journal of Luminescence* 100.1-4 (2002), pp. 35–45. DOI: 10.1016/S0022-2313(02)00423-4.

[73] Peter Bishop. *AIRPLANE SEAT TRACK*. 2011.

[74] NASA. 'EXTERNAL PAYLOADS PROPOSER ' S GUIDE to the International Space Station External Payloads Proposer ' s Guide to the International Space Station'. In: (2017).

[75] Doodle Labs. *ACM-DB-2 Industrial Wi-Fi Transceiver*. 2020.

[76] PCI-SIG. *PCI Express ® Mini Card Electromechanical Specification Revision 1.2*. 2007. URL: www.pcisig.com.

[77] Carlos Cilla Hernandez. 'Communication systems in the international space station (ISS)'. In: *International Astronautical Federation - 55th International Astronautical Congress 2004* 11 (2004), pp. 7489–7498. DOI: 10.2514/6.iac-04-t.2.09.

[78] David M. Hornyak. *A Researcher's Guide to: International Space Station Technology Demonstration*. 2013.

[79] *How does the ISS communicate to Earth?* URL: https://www.quora.com/How-does-the-ISS-communicate-to-Earth (visited on 04/11/2020).

[80] J. (USC/Information Sciences Institute) Postel. *User Datagram Protocol*. 1980.

[81] Michelle Schneider and Nasa Msfc Fd. 'Payload Operations Integration Center Remote Operations Capabilities Payload Operations Options Telescience Resource Kit (TReK) Telemetry Services'. In: October (2001).

[82] SpaceX. 'DragonLab: Fast track to flight'. In: (2016), pp. 3–4.

[83] SpaceX. 'Falcon 9 Launch Vehicle Payload User's Guide'. In: *SpaceX* (2008), p. 65.

[84] PCI-SIG. *PCI Express Base Specification, Revision 3.0*. 2010.

[85] Motorola Inc. *SPI Block Guide*. 2003.

[86] Bosch. *CAN Specification Version 2.0*. 1991. URL: http://esd.cs.ucr.edu/webres/can20.pdf.

[87] NXP Semiconductors. *I2C-bus specification and user manual*. 2014.

[88] Donald F. Specht. 'A General Regression Neural Network'. In: *IEEE Transactions on Neural Networks* 2.6 (1991), pp. 568–576.

[89] Yoshiyasu Takefuji. *Neural Network Parallel Computing*. September. 1992. DOI: 10.1007/978-1-4615-3642-0.

[90] Akio Ohba and Masayuki Chatani. *Information processing apparatus, graphic processing unit, graphic processing method, storage medium, and computer program*. 2005.

[91] Jan Henrik Müller. 'Particle-Antiparticle Discrimination using Neural Networks'. Bachelor Thesis. Technical University of Munich, 2018.

[92] Bosch. *CAN with Flexible Data-Rate Specification Version 1.0*. 2012.

[93] M Schreiner et al. 'Introduction of CAN FD into the next generation of vehicle EE architectures.pdf'. In: (2017), pp. 1–6.

[94] Microchip Technology Incorporated. *MCP2515 Stand-Alone CAN Controller with SPI Interface*. 2019. URL: http://ww1.microchip.com/downloads/en/DeviceDoc/MCP2515-Stand-Alone-CAN-Controller-with-SPI-20001801J.pdf.

[95] Pedro Bernardo. 'Development of technology and procedures for health monitoring of UAV subsystems Examination Committee'. In: November (2015).

[96] Microchip Technology Incorporated. *MCP2518FD External CAN FD Controller with SPI Interface*. 2019.

[97] Microchip Technology Incorporated. *ATA6560/1 High-Speed CAN Transceiver with Standby Mode CAN FD Ready Data Sheet*. 2018.

[98] COBHAM. *UT64CAN333x CAN FD Transceivers Released Datasheet*. 2019.

[99] Analog Devices. *LTC2875 High Speed CAN FD Transceiver Datasheet*. 2019.

[100] Microchip Technology Incorporated. *ATmega16M1/32M1/64M1*. 2016.

[101] Microchip Technology Incorporated. *8-bit Atmel Microcontroller Programmable ATmega128L*. 2011. URL: http://www.atmel.com/images/doc2467.pdf.

[102] Microchip Technology Incorporated. *ATmegaS128*. 2017.

[103] Analog Devices. *ADG704*. 1999.

[104] Maxim integrated. *MAX4734 Analog Multiplexer*. 2016.

[105] Analog Devices. *ADG804*. 2005.

[106] Analog Devices. *ADG1606/ADG1607*. 2012.

[107] Analog Devices. *ADG706/ADG707*. 2016.

[108] ElectronS. *measurement - Making Sense of Current Sensing - Electrical Engineering Stack Exchange*. 2016. URL: https://electronics.stackexchange.com/questions/251826/making-sense-of-current-sensing/251831 (visited on 06/11/2020).

[109] Texas Instruments. *INA233 High-Side or Low-Side Measurement, Bidirectional Current and Power Monitor*. 2017. URL: http://www.ti.com/lit/ds/symlink/ina226.pdf.

[110] Texas Instruments. *INA226-Q1 AEC-Q100, 36-V, 16-Bit, Ultra-Precise, I2C Output Current, Voltage, and Power Monitor With Alert*. 2020.

[111] Texas Instruments. *INA260 Precision Digital Current and Power Monitor With Low-Drift , Precision Integrated Shunt*. 2016.

[112] Bosch. *BMX055 Small , versatile 9-axis sensor module*. 2014.

[113] Bosch. *BNO055 Intelligent 9-axis absolute orientation sensor*. 2016. URL: https://ae-bst.resource.bosch.com/media/%7B%5C_%7Dtech/media/datasheets/BST%7B%5C_%7DBNO055%7B%5C_%7DDS000%7B%5C_%7D14.pdf.

[114] Analog Devices. 'Low Noise, Low Drift, Low Power, 3-Axis MEMS Accelerometers ADXL356 / ADXL357'. In: (2016), pp. 1–42.

[115] Bosch. *BMP280 digital pressure sensor*. 2014. URL: https://www.sparkfun.com/datasheets/Components/General/BST-BMP085-DS000-05.pdf.

[116] Bosch. *BME680 Low power gas, pressure, temperature & humidity sensor*. 2019.

[117] Microchip Technology Incorporated. *Low-Power Linear Active Thermistor ICs - MCP9700 / 9700A MCP9701 / 9701A Datasheet*. 2007.

[118] Analog Devices. '4-Channel, I2 C, Ultra Low Power, 12-Bit ADC in 20-Lead LFCSP / TSSOP AD7091R-5'. In: (2018).

[119] The PostgreSQL Global Development Group. *PostgreSQL: The world's most advanced open source database*. 2013. URL: https://www.postgresql.org/%20http://www.postgresql.org/ (visited on 26/06/2020).

[120] Code Synthesis. *ODB - C++ Object-Relational Mapping (ORM)*. 2019. URL: https://www.codesynthesis.com/products/odb/ (visited on 26/06/2020).

[121] Microchip Technology Incorporated. *AVR- and Arm- Toolchains (C Compilers) | Microchip Technology*. URL: https://www.microchip.com/mplab/avr-support/avr-and-arm-toolchains-c-compilers (visited on 29/06/2020).

[122] Dreamiurg. *GitHub - dreamiurg/avr-liberty: Library of routines for AVR microcontollers*. URL: https://github.com/dreamiurg/avr-liberty (visited on 29/06/2020).

[123] ExploreEmbedded. *GitHub - ATmega32_ExploreUltraAvrDevKit*. URL: https://github.com/ExploreEmbedded/ATmega32%7B%5C_%7DExploreUltraAvrDevKit (visited on 29/06/2020).

[124] International Organization for Standardization (ISO). *ISO/IEC 14882:2011 - Information technology — Programming languages — C++*. 2011. URL: https://www.iso.org/standard/50372.html.

[125] Martin Pitt. *systemd - Ubuntu Wiki*. URL: https://wiki.ubuntu.com/systemd (visited on 26/06/2020).

[126] NVIDIA Corporation. *NVIDIA Parker Series SoC Technical Reference Manual*. 2017.

[127] American National Standards Institute. *IEEE Standard for A Versatile Backplane Bus: VMEbus*. Vol. 1987. 1987, pp. 1014–1987.

[128] NVIDIA Corporation. *JETSON TX2 PLATFORM ADAPTATION AND BRING-UP GUIDE*. 2019.

[129] NVIDIA Corporation. *OEM PRODUCT DESIGN GUIDE NVIDIA Jetson TX2*. 2018.

[130] Rui Ji et al. 'The Effect of Electrical Connector Degradation on High-Frequency Signal Transmission'. In: *IEEE Transactions on Components, Packaging and Manufacturing Technology* 7.7 (2017), pp. 1163–1172. DOI: 10.1109/TCPMT.2017.2688023.

[131] Renesas. *9DBL02x2 - PCIe Zero-Delay/Fanout Buffers*. Tech. rep. 2020, p. 36.

[132] Texas Instruments. *DS80PCI402 2.5-Gbps / 5.0-Gbps / 8.0-Gbps 4-Lane PCI-Express™ Repeater With Equalization and De-Emphasis*. 2015. URL: www.ti.com.

[133] Samtec. *EYE Speed HIGH-SPEED I/O SYSTEM*. 2017.

[134] Analog Devices. *LTC4311 - I2C/SMBus Accelerator*. 2008. URL: http://www.linear.com/leadfree/.

[135] I Dal Allan. 'SFF Committee SFF-8431 Specifications for Enhanced Small Form Factor Pluggable Module SFP +'. In: *ReVision* 408 (2009).

[136] Gerhard Goos, Juris Hartmanis and Jan van Leeuwen. *Field-Programmable Logic and Applications*. 2003.

[137] PCI-SIG. *PCI-SIG - FAQ - PCI Express 3.0*. URL: https://web.archive.org/web/20140201172536/http://www.pcisig.com/news%7B%5C_%7Droom/faqs/pcie3.0%7B%5C_%7Dfaq/%7B%5C#%7DEQ2 (visited on 07/09/2020).

List of Figures

List of Tables

Appendix A

Additional Material

A.1 PCIe Generation Comparison

Table A.1: PCIe transfer rates in comparison with its version history [137].

Version	Line code	overhead [%]	Transfer rate [GT s^{-1}]	Throughput [GB s^{-1}]				
				x1	x2	x4	x8	x16
1.x	8b/10b	20	2.5	0.2500	0.5000	1.000	2.000	4.000
2.x	8b/10b	20	5.0	0.5000	1.000	2.000	4.000	8.000
3.0	128b/130b	1.54	8.0	0.9846	1.9692	3.9385	7.877	15.754

The overhead in Table A.1 is calculated from the line encoding scheme as 2/10 and 2/130. One can calculate the throughput with following formula:

$$\text{PCIe transfer rate} \times (1 - \text{encoding overhead}) \times \text{lane width}/8\,\text{bit} = \text{PCIe throughput} \tag{A.1}$$

The throughput is calculated for one direction only as PCIe is full duplex capable.

A.2 Single Board Computer Test Results

The consumed power values for full GPU and CPU utilisation and also individual CPU and GPU tests can be found in Table A.2. Figure A.1 and A.2 show power consumption measurements for GPU and CPU individual tests.

Figure A.3 and A.4 show the run time per event on GPU and CPU for a batch size of 1000 events. Detailed event rate test values can be found in Table A.3.

For a detailed description of the measurement setup and the used TensorFlow loads see section 4.1.1 and 4.1.2.

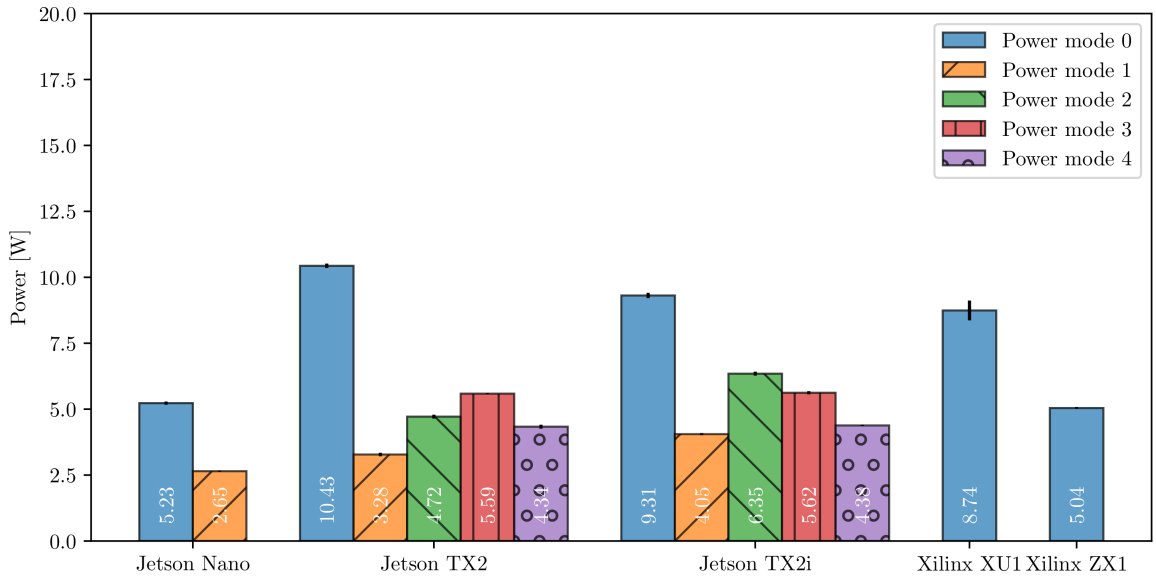

Figure A.1: CPU power consumption of tested single board computers: Colours show power modes where available. A 5 min long CPU test was conducted and the power consumption was averaged. Standard deviation from mean values are indicated with black error bars.

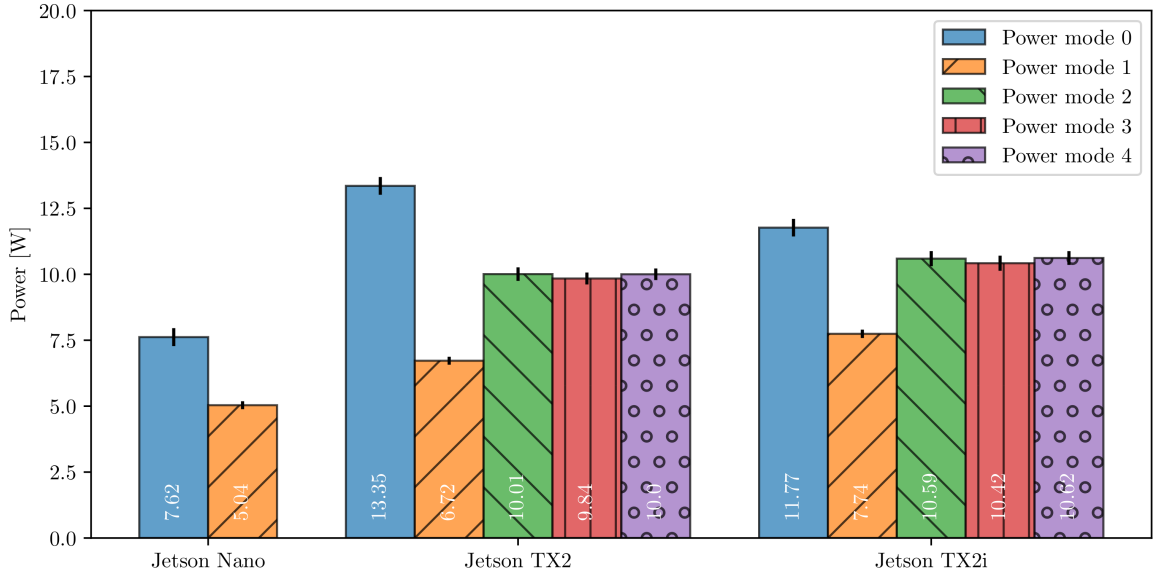

Figure A.2: GPU power consumption of tested single board computers: Colours show power modes where available. A 5 min long GPU test was conducted and the power consumption was averaged. Standard deviation from mean values are indicated with black error bars.

Table A.2: Power consumption of tested single board computers in different power modes (where available).

Processor	Power consumption in [W]
Enclustra Zynq Mercury+ XU1	8.6 ± 0.5
Enclustra Zynq Mercury ZX1	5.2 ± 0.2
Nvidia Jetson Nano	
Power mode 0 CPU	5.2 ± 0.2
Power mode 0 GPU	7.5 ± 0.5
Power mode 0 CPU & GPU	9.8 ± 0.4
Power mode 1 CPU	2.6 ± 0.2
Power mode 1 GPU	5.1 ± 0.4
Power mode 1 CPU & GPU	5.0 ± 0.3
Nvidia Jetson TX2	
Power mode 0 CPU	10.2 ± 0.2
Power mode 0 GPU	13 ± 5
Power mode 0 CPU & GPU	19 ± 1
Power mode 1 CPU	3.3 ± 0.2
Power mode 1 GPU	6.8 ± 0.3
Power mode 1 CPU & GPU	7.8 ± 0.3
Power mode 2 CPU	4.8 ± 0.2
Power mode 2 GPU	9.8 ± 0.3
Power mode 2 CPU & GPU	12.2 ± 0.5
Power mode 3 CPU	5.5 ± 0.2
Power mode 3 GPU	9.8 ± 0.3
Power mode 3 CPU & GPU	12.6 ± 0.4
Power mode 4 CPU	4.4 ± 0.4
Power mode 4 GPU	9.8 ± 0.3
Power mode 4 CPU & GPU	11.5 ± 0.5
Nvidia Jetson TX2i	
Power mode 0 CPU	9.2 ± 0.3
Power mode 0 GPU	11.5 ± 0.5
Power mode 0 CPU & GPU	16.0 ± 0.6
Power mode 1 CPU	4.1 ± 0.2
Power mode 1 GPU	7.9 ± 0.3
Power mode 1 CPU & GPU	9.0 ± 0.3
Power mode 2 CPU	6.3 ± 0.2
Power mode 2 GPU	10.6 ± 0.4
Power mode 2 CPU & GPU	13.0 ± 0.4
Power mode 3 CPU	5.6 ± 0.2
Power mode 3 GPU	10.6 ± 0.4
Power mode 3 CPU & GPU	12.7 ± 0.4
Power mode 4 CPU	4.3 ± 0.2
Power mode 4 GPU	10.6 ± 0.4
Power mode 4 CPU & GPU	12.0 ± 0.4

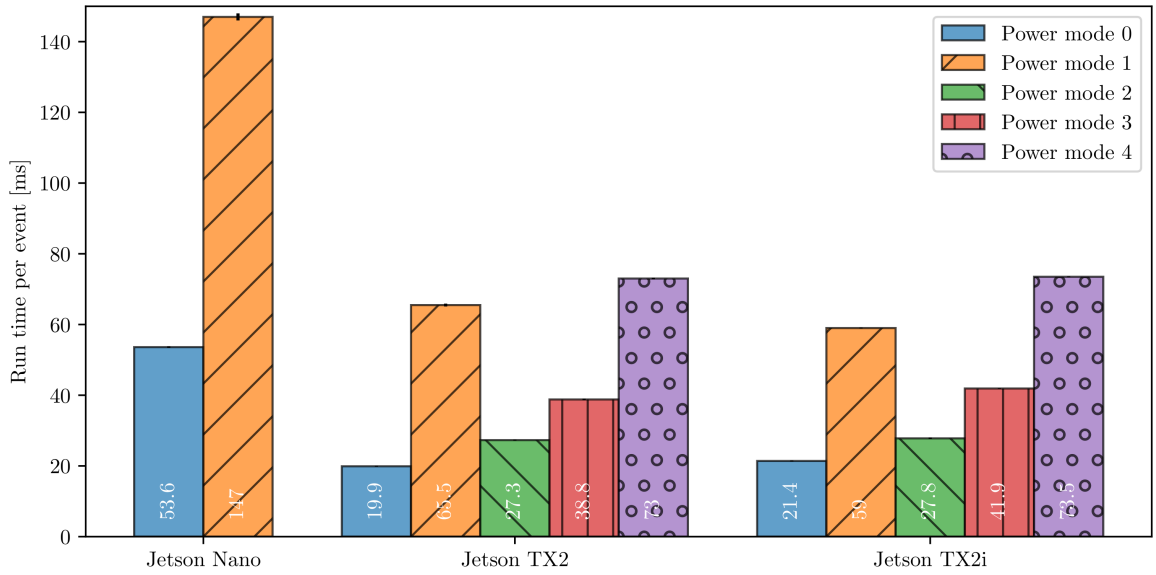

Figure A.3: Test results for run time per event for 1000 events per batch on CPU of Jetson Nvidia modules. Standard deviation from mean values are indicated with black error bars.

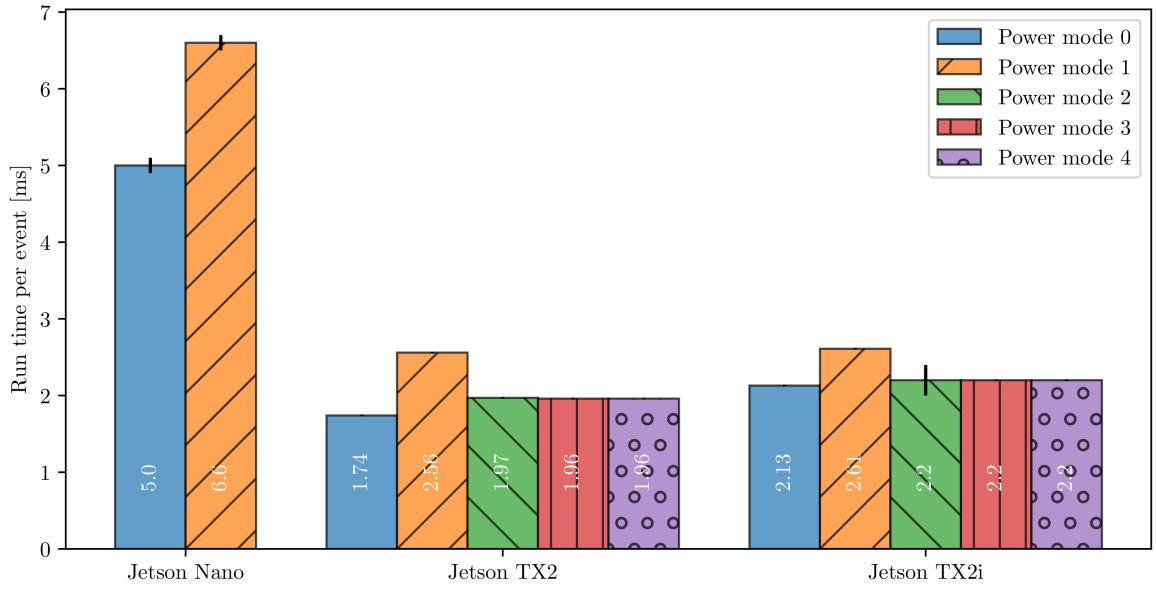

Figure A.4: Test results for run time per event for 1000 events per batch on GPU of Jetson Nvidia modules. Standard deviation from mean values are indicated with black error bars.

Table A.3: Run time per event for different batch sizes on different single board computers.

Processor	Run time per event with batch size [ms]			
	1	10	100	1000
Enclustra Zynq Mercury+ XU1	81 ± 1	74.74 ± 0.08	81.0 ± 0.3	
Enclustra Zynq Mercury ZX1	1890 ± 50	1860 ± 14	1870 ± 20	
Nvidia Jetson Nano				
Power mode 0 CPU	54.6 ± 0.9	50.5 ± 0.3	51.6 ± 0.1	53.6 ± 0.2
Power mode 0 GPU	11.2 ± 0.7	5.9 ± 0.1	5.08 ± 0.05	5.0 ± 0.1
Power mode 1 CPU	145 ± 2	138.5 ± 0.7	141.3 ± 0.1	147 ± 1
Power mode 1 GPU	20 ± 4	7.5 ± 0.5	6.8 ± 0.1	6.6 ± 0.1
Nvidia Jetson TX2				
Power mode 0 CPU	26 ± 3	22 ± 1	20.2 ± 0.2	19.9 ± 0.1
Power mode 0 GPU	13 ± 2	2.2 ± 0.2	1.77 ± 0.02	1.74 ± 0.01
Power mode 1 CPU	69 ± 2	64 ± 1	65.6 ± 0.2	65.5 ± 0.4
Power mode 1 GPU	10.9 ± 0.6	3.3 ± 0.1	2.57 ± 0.01	2.56 ± 0.01
Power mode 2 CPU	34 ± 2	28 ± 1	28 ± 6	27.3 ± 0.1
Power mode 2 GPU	20 ± 2	2.8 ± 0.2	2.01 ± 0.08	1.97 ± 0.01
Power mode 3 CPU	42 ± 1	38.4 ± 0.4	39.1 ± 0.1	38.8 ± 0.2
Power mode 3 GPU	7.3 ± 0.6	2.6 ± 0.1	2.00 ± 0.01	1.96 ± 0.01
Power mode 4 CPU	85 ± 6	75 ± 3	73 ± 1	73.0 ± 0.2
Power mode 4 GPU	24 ± 5	2.8 ± 0.2	2.02 ± 0.02	1.96 ± 0.01
Nvidia Jetson TX2i				
Power mode 0 CPU	28 ± 3	24 ± 1	21.9 ± 0.1	21.4 ± 0.1
Power mode 0 GPU	15 ± 2	2.7 ± 0.4	2.15 ± 0.02	2.13 ± 0.01
Power mode 1 CPU	62 ± 1	58.2 ± 0.3	59.4 ± 0.1	59.0 ± 0.1
Power mode 1 GPU	10.5 ± 0.4	3.3 ± 0.1	2.63 ± 0.08	2.61 ± 0.01
Power mode 2 CPU	33 ± 2	28.2 ± 0.6	28.4 ± 0.4	27.8 ± 0.2
Power mode 2 GPU	19 ± 2	3.0 ± 0.2	2.24 ± 0.02	2.2 ± 0.2
Power mode 3 CPU	45 ± 1	41.4 ± 0.2	42.2 ± 0.1	41.9 ± 0.1
Power mode 3 GPU	7.6 ± 0.3	2.78 ± 0.06	2.21 ± 0.01	2.20 ± 0.01
Power mode 4 CPU	85 ± 5	76 ± 2	74.8 ± 0.4	73.5 ± 0.1
Power mode 4 GPU	23 ± 4	2.9 ± 0.2	2.26 ± 0.02	2.20 ± 0.01

A.3 Operating Mode Power Consumption

Figure A.5 shows power consumption measurements for all operating modes defined in section 5.2.4. Individual CPU and GPU test results can also be found in Table A.4. For a detailed description of the measurement setup and the used TensorFlow loads see section 4.1.1 and 6.2.2.

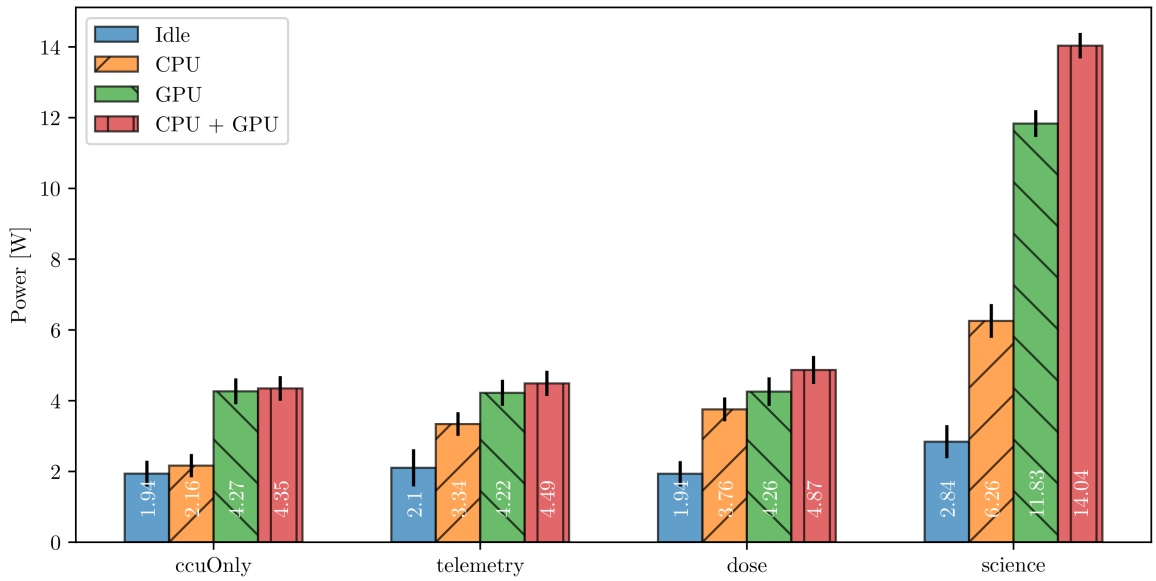

Figure A.5: CCU power consumption in different operating modes. Standard deviation from mean values are indicated with black error bars.

Table A.4: Power consumption of the CCU in different operating modes.

Power Mode	Idle [W]	CPU [W]	GPU [W]	GPU + CPU [W]
ccuOnly	1.94(0.37)	2.17(0.33)	4.27(0.37)	4.37(0.35)
telemetry	2.10(0.53)	3.34(0.33)	4.22(0.37)	4.49(0.36)
dose	1.94(0.36)	3.76(0.34)	4.26(0.40)	4.87(0.40)
science	2.84(0.47)	6.26(0.48)	11.83(0.38)	14.04(0.36)